A full-Stokes finite-element model for the vicinity of Dome Fuji with flow-induced ice anisotropy and fabric evolution

Hakime Seddik

Doctoral Thesis

Division of Environmental Science Development
Graduate School of Environmental Science
Hokkaido University

March 2008

Acknowledgments

I would like to express my sincere thanks to all people that contributed to this thesis.

Thanks to my supervisor Ralf Greve for his help and wise guidance during my research. His contribution has made possible the good achievements in this thesis.

Thanks to all of the evaluation committee members, Takeo Hondoh, Motoyoshi Ikeda, Takayuki Shiraiwa and Ayako Abe-Ouchi for their interest in my work and for their valuable comments.

Thanks to Luca Placidi for his invaluable contribution and help. Not only his previous work has been the building block for this thesis but also his contribution was a rich source of information for me.

Thanks to Thomas Zwinger for his patience and his help in using Elmer. His work was a great value for this thesis. With him, thanks to all members at CSC for their help and kindness during my visit there. A special thought to Juha Ruokolainen, Peter Råback and Mikko Lyly for their technical support. Thanks to Olivier Gagliardini for his contribution, useful discussion and invaluable comments that he gave to improve the content of my work. Also I should not forget all people at the LGGE in Grenoble for their kindness during my visit and the interesting discussions that we had there.

Thanks to Ilka Hamann for kindly sharing her data and thanks to all people who have expressed their interest in my work, Sérgio Faria and all members of the Glacier and Ice Sheet Research group.

I would also like to thank all my family in France for their support, patience and encouraging. Thanks to all friends in Sapporo and the nice relaxing moments around a coffee. Lastly, thanks to Emiko for her kind support and encouraging during those years passed as a doctor student.

Contents

List of Figures

Abstract

A three-dimensional, thermo-mechanically coupled flow model with induced anisotropy has been developed and applied to the vicinity of Dome Fuji, Antarctica, the site of a recent Japanese deep ice drilling project. The model implements the full-Stokes equations for the ice dynamics, and the system is solved with the finite-element method (FEM) using the open source multi-physics package Elmer.

A Continuum-mechanical, Anisotropic Flow model, based on an anisotropic Flow Enhancement factor (CAFFE model) is used for taking into account flow-induced anisotropy in ice. The flow law is implemented in Elmer/Ice by means of second and fourth order orientation tensors that describe the c-axis orientation of the fabric. Similarly, the fabric evolution equation is written in terms of the evolution of the second order tensor, and it is solved inside Elmer/Ice with a Discontinuous Galerkin method using Picard type iterations for the non-linearity. Since the fabric evolution equation also depends on the fourth order orientation tensor, the IBOF (Invariant-Based Optimal Fitting) closure function is used for the computation of its components from the solution of the second orientation.

The main questions addressed by the simulations carried out in this thesis are (i) what is the local flow field in the vicinity of Dome Fuji, (ii) how is the flow field affected by the anisotropic fabric, and (iii) what are the consequences for the interpretation of the climatological proxy data of the Dome Fuji ice core. The results are therefore relevant for the reconstruction of the paleo-climatic variability in East Antarctica, which is an important clue for understanding possible future climate changes on Earth. Further, the improved modeling of ice dynamics by solving the full-Stokes equations and including anisotropy is an important step towards simulating rapid dynamical changes which may destabilize the terrestrial ice sheets and lead to a potentially dangerous rate of sea level rise in a warming environment.

Notations

Tensors, vectors and scalars:

A, a, α	scalars,
$\mathbf{a}$, $\mathbf{c}$	vectors,
A	tensor A_{ij} or A_{ijkl},
$\mathbf{a} \otimes \mathbf{b} = \mathsf{C}$	tensorial product $a_i b_i = C_{ij}$,
$\mathsf{A} \cdot \mathsf{B} = \mathsf{C}$	simple contraction (dot product) $A_{ik}B_{kj} = C_{ij}$,
$\mathsf{A} : \mathsf{B} = C$	double contracted product $A_{ij}B_{ji} = C$,
$\mathsf{A} : \mathsf{B} = \mathsf{C}$	double contracted product $A_{ijkl}B_{lk} = C_{ij}$,
A^{T}	transpose of A, $A^T_{ij} = A_{ji}$.

Acronyms:

ODF	Orientation Distribution Function,
OMD	Orientation Mass Density,
IBOF	Invariant Based Optimal Fitting closure approximation function,
GRIP	Greenland Ice Core Project,
EDML	Epica ice core at Kohnen station in Dronning Maud Land,
UC	Uniaxial Compression,
SS	Simple Shear,
SM	Single Maximum.

Quantities used in the manuscript:

A	Ice age,
$A(T^{'})$	Rate factor,
A_0	Pre-exponential constant in the Arrhenius law,
$\mathcal{A}^*$	Deformability of a single crystal,
$\mathcal{A}$	Deformability of the polycrystal,
$\mathsf{a}^{(2)}$ and $a_{ij}^{(2)}$	Second-order orientation tensor,
$\mathsf{a}^{(4)}$ and $a_{ijkl}^{(4)}$	Fourth-order orientation tensor,
a_b	Basal melting,
c	Specific heat,
D and D_{ij}	Rate of strain tensor,
D_t^2	Scalar invariant describing the deformation on the crystal basal plane,
d	Effective strain,
$\hat{E}$	Enhancement factor function,
$E_{\max}$	Maximum softening,
$E_{\min}$	Minimum hardening,
f^*	Orientation distribution function,
g	Gravity acceleration.
H	Ice thickness,
$\mathcal{H}^*$	Function for the hardness,
II, III	Second and third invariants of $\mathsf{a}^{(2)}$,
k	Heat Conductivity,
L	Velocity gradient tensor,
n	Stress exponent,
$\mathbf{n}$	Normal unit vector,
p	Pressure,
Q	Activation energy,
$\mathbf{q}$	Heat flux,
$\mathbf{q}^*$	Orientation flux,
q_{geo}	Geothermal heat flux,
R	Universal gas constant,
$R(\theta)$	Radius of the equipotential ellipse,
S and S_{ij}	Deviatoric stress tensor,
S_t^2	Scalar invariant describing the stress on the crystal basal plane,
S^2	Unit sphere,
T and T_{ij}	Cauchy stress tensor,
T	Temperature,

T'	Temperature relative to pressure melting,
$\mathbf{t}$	Tangential unit vector,
t	Time,
$\mathbf{u}^*$	Orientation transition rate,
$\mathbf{v}$ and v_i	Velocity,
W	Spin tensor,
β_i	Coefficients for the calculation of the IBOF function,
$\mathbf{\Gamma}^*$	Orientation production rate,
Γ	Positive constant used in the orientation production rate equation,
δ_{ij}	Kronecker symbol,
γ	Horizontal bed parallel shear rate,
ϵ	Negative vertical strain rate,
η	Viscosity,
θ	Co-latitude of the general lattice-orientation,
ι	Positive constant used in the orientation transition rate equation,
λ	Orientation diffusivity,
ρ	Mass density of ice,
ρ^*	Orientation mass density,
σ	Effective stress,
Φ, $\mathbf{\Phi}$	Test functions,
ϕ	Potential (work rate),
φ	Longitude of the general lattice-orientation,
Ψ_i, Ψ_j	Interpolation functions.

Chapter 1

Introduction

In the perspective of climate change, ice sheets (Greenland and Antarctica) constitute an important component of the climate system. Their geographical location has allowed a unique accumulation of frozen water on the Earth (Antarctica accounts for 70% of the fresh water available on our planet) and in the context of warming environment, their detailed study is crucial to assess climate change. Ice sheets essentially provide a mean

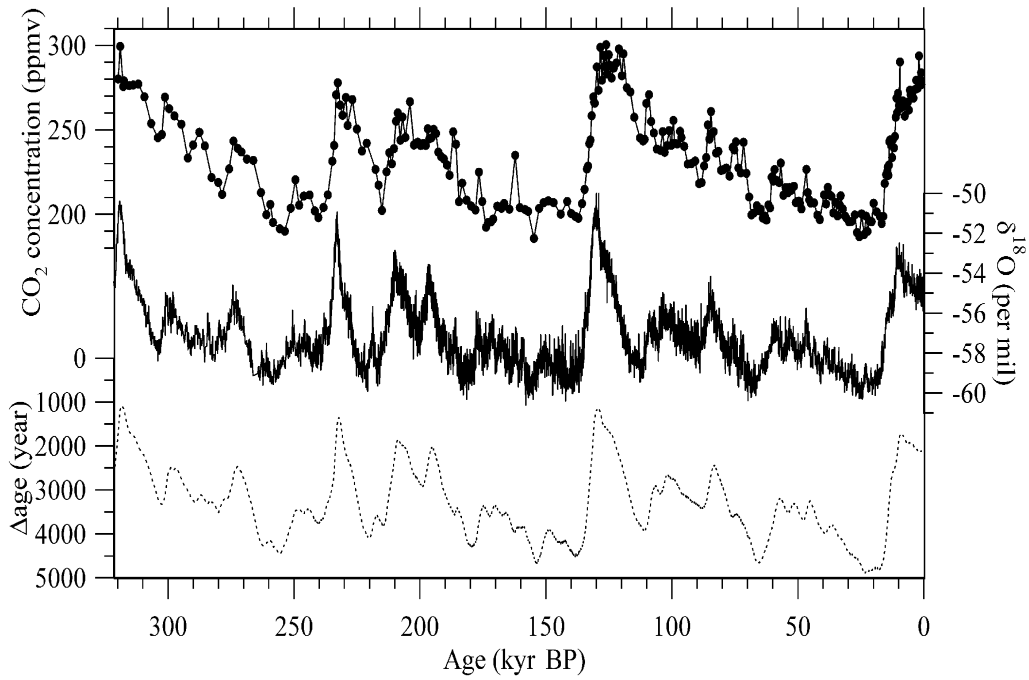

Figure 1.1: Variations of the CO_2 concentration, $\delta^{18}O$ values and age differences between air and its surrounding ice for the past 320 kyr obtained with the Dome Fuji ice core (Kawamura and others, 2003).

for better understanding of past climatic changes associated with the evolution of Earth as ice contains long record of informations that can be used for this purpose. With the paleo-climatic reconstructions provided by ice sheets, understanding of past climatic changes necessarily provides knowledges for the understanding of future climate change. Paleo-climatic reconstruction can be performed by the use of climatic proxy contained in the ice (oxygen and deuterium isotopes, CO_2, etc) which can be used to reconstruct climatic variations. Those proxy are measured in ice cores which are drilled in particular locations of ice sheets where the ice is thick enough to provide informations which go far in time in the climate history. An example of such measurements is given by Fig. 1.1, for the Dome Fuji ice core. The interpretation of δ^{18}O variations over time allows assessing the temperature variations and recognizing the different climatic periods. Here, the last three glacial-interglacial climatic cycles can be recognized. It becomes therefore essential to be able to better interpret those proxy in relation with ice sheets dynamics (flow, temperature variation, fabric). But it is also important to being able to better exploit ice cores, and it has became urgent to define future ice core drilling sites in order to locate older ice and therefore to provide, further in the past, paleo-climatic reconstructions.

Another aspect of the better understanding of future climate change is associated with the sea level change. Future sea level change has became an important issue (Fig. 1.2) so that understanding its factors of occurrence is essential. Because of the large amount of water that they contain, ice sheets are crucial actors in seal level change as sudden melting of ice sheets will have a dramatic effect on sea level rise. In a warming environment, ice sheets can encounter rapid dynamical change which can trigger their rapid destabilization. The rapid change of ice sheets dynamics needs to be better understood by improved modeling and by taking into account anisotropy in ice and its relation with ice sheets flow. Therefore, better modeling of ice sheet flow associated with ice fabrics is required for this purpose.

Ice sheets or glaciers, consists of zillions of individual hexagonal crystals ("ice Ih") with a typical diameter of millimeters to centimeters. This length scale stands in contrast with the size of the ice masses, which ranges from 100's of meters to 1000's of kilometers. It has long been known that, while the distribution of the crystallographic axes (also known as optical axes or c-axes) at the surface of an ice sheet is essentially at random, deeper down into the ice, different types of anisotropic fabrics (crystals orientations) with preferred orientations of the c-axes tend to develop.

Many models have been proposed to describe the anisotropy of polar ice. On the one end of the range in complexity, there are descriptions by a simple flow enhancement factor, introduced in an *ad-hoc* fashion as a multiplier of the isotropic ice fluidity. On the other end, viscoplastic self-consistent (VPSC) models have been formulated, in which the macroscopic behavior of the polycrystalline aggregate is calculated by a homogenization

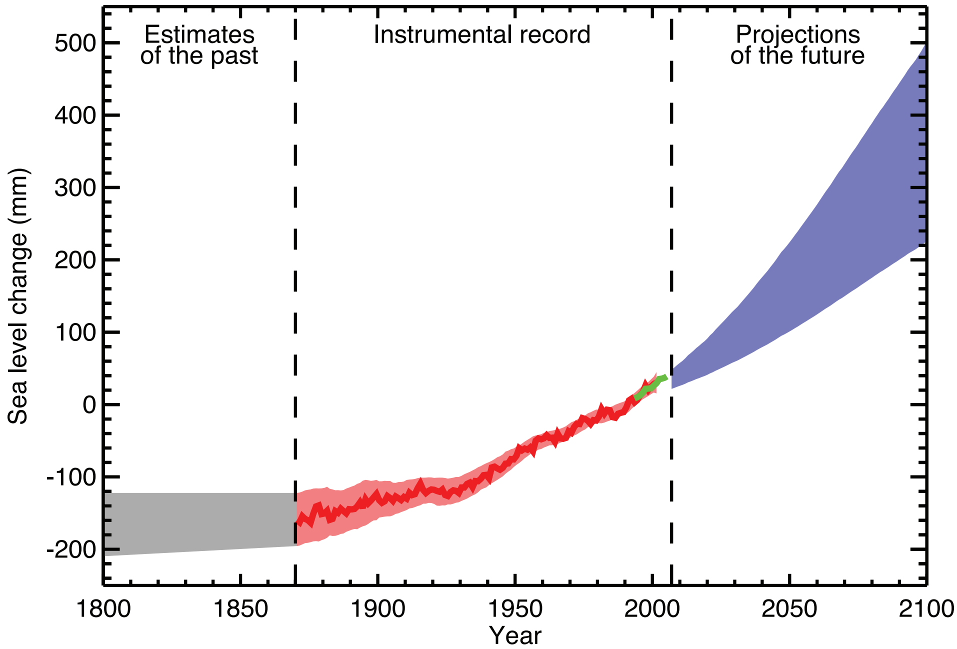

Figure 1.2: Time series of global mean sea level (deviation from the 1980-1999 mean) in the past and as projected for the future (IPCC fourth assessment report: climate change 2007)

procedure of the microscopic behavior, and on the microscopic scale the influence of the neighborhood of each ice crystal is accounted for by considering this grain as an inclusion embedded in a homogeneous matrix [see Gillet-Chaulet and others (2005), Placidi and others (2006), and references therein]. However, the more sophisticated models are usually too complex and computationally time-consuming to be included readily in a model of macroscopic ice flow, and therefore, the flow law used in ice-flow models is usually that of an isotropic fluid.

Here, the Continuum-mechanical, Anisotropic Flow model, based on an anisotropic Flow Enhancement factor, is used ("CAFFE model"). It is laid down in detail in the study by Placidi and others (2008) [based on previous works by Placidi (2004, 2005); Placidi and Hutter (2006a); Faria (2006a,b); Faria and others (2006)], and takes the flow enhancement factor as a function of a newly introduced scalar quantity called *deformability*, which is essentially a non-dimensional invariant related to the shear stress acting on the basal plane of a single crystal, weighted by the orientation-distribution function which describes the anisotropic fabric of the polycrystal. Fabric evolution is modeled by an orientation mass balance which accounts for grain rotation and recrystallization processes. The CAFFE model fulfills all the fundamental principles of classical continuum mechanics (see also Placidi and Hutter, 2006b), is sufficiently simple to allow numerical implementations in ice-flow models and contains only a limited number of free parameters.

The CAFFE model is applied to the vicinity of Dome Fuji (Fig 1.3; 77°19'01"S, 36°42'11"E; elevation 3810 m.a.s.l.) We model the dynamics by means of a full-Stokes finite-element model that takes into account ice anisotropy. The general objective of this simulation is to better understand the variation and evolution of ice sheets in a warning environment. This study therefore aims for better reconstruction of the paleo-climatic variability in East Antarctica by being able to better exploit ice cores and by improving interpretation of climatological proxy of the Dome Fuji ice core. Better understanding of rapid dynamical change of ice sheets constitutes the second objective of this work. The full-Stokes anisotropic flow model will allow for better modeling of flow dynamics variations which is important to assess sea level change.

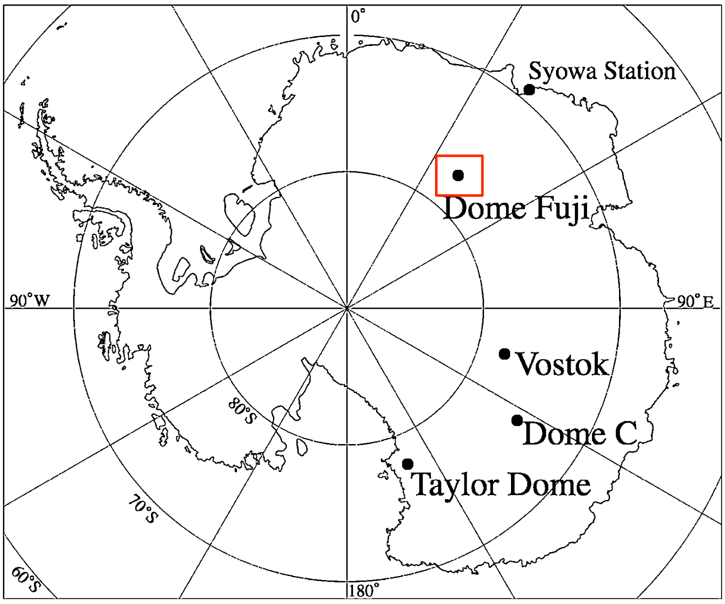

Figure 1.3: Antarctica ice sheet and location of Dome Fuji. Vostok, Dome C, Taylor Dome and Japanese Antarctic station, Syowa are also shown (Kawamura and others, 2003). The red square represents the 200 x 200 km domain used for the finite-element model developed in this work (Chapter 6).

The chapters of this manuscript describes the model equations and its application. We start in the first chapter by reviewing quickly the physical processes of deformation for the mono and polycrystal ice. There, we review the work which has been done to model ice deformation associated with anisotropy. Work which has been done to model ice sheets with flow induced anisotropy is also presented.

In Chapter 3, we introduce and discuss the general theory of modeling ice anisotropy by using the CAFFE model. The anisotropic flow law and the fabric evolution equation are presented. For the fabric evolution equation, different re-crystallization processes that the theory is able to model are also discussed.

In Chapter 4, equations for modeling anisotropy are applied to the EDML ice core, Antarctica, with an one-dimensional model. This application is necessary to demonstrate the performance of the CAFFE model and to validate the equations. It also allows validating the model stability before the application to large scale modeling.

In Chapter 5, the challenges of applying the CAFFE model to large scale finite-element modeling are discussed and overcome. The formulation of the anisotropic flow law and the fabric evolution equation in terms of second and fourth-order orientation tensors are presented. Solution method for the fourth-order tensor based on an Invariant Based Optimal Fitting approximation function (IBOF) is discussed.

Finally, in Chapter 6, the full-Stokes anisotropic flow model is applied to the vicinity of Dome Fuji. We present the model boundary conditions, geometry and finite-element mesh. The simulation of the flow is proposed and the results for the age across the domain are depicted for isotropic steady-state conditions. The results for the fabric evolution are then presented and we study the influence of anisotropy on ice flow. Interpretations of textures obtained with the Dome Fuji ice core are then proposed and the age obtained with anisotropic velocities is compared to the isotropic age.

Chapter 2

Deformation mechanism in polar ice and large scale modeling of ice sheets

2.1 Introduction

In this section, we start to discuss general notions of ice deformation, induced anisotropy and fabric development in polar ice caps. We focus on the description of ice anisotropy, the behavior of the monocrystal of ice and the generalization of anisotropy to polycrystal.

With this description, we give a short review of present flow model with induced ice anisotropy as well as the work which has been done to model the ice sheet flow at large scales.

2.2 Deformation mechanism in polar ice

2.2.1 Deformation of the monocrystal of ice

In normal terrestrial conditions of temperature and pressure, the monocrystal of ice has a hexagonal structure (ice Ih). The largest density of oxygen occurs on the basal plan and the hexagonal axis of symmetry (axis c) is perpendicular to this plan (Fig. 2.1). The optical axis corresponds to the c-axis so that the c-axis orientation can be understood by polarization.

The viscoplastic deformation primarily results from the glide of dislocations on the basal plan and for this reason, the ice monocrystal is a strong natural anisotropic material. For the same regime of stress, the resolved shear deformation parallel to the basal plan is three to four times higher than the deformation in compression perpendicular to the basal plane. Duval and others (1983) have showed that the secondary creep of the ice monocrystal with basal deformation corresponds to a power law with an exponent for the

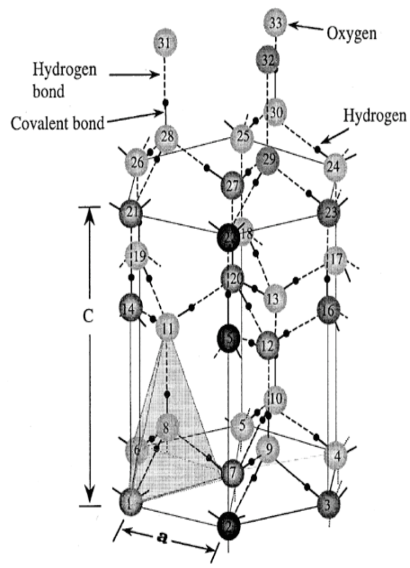

Figure 2.1: Representation of the hexagonal crystallographic structure of terrestrial ice (Schulson, 1999).

stress $n = 2$ and an activation energy of 63 $\mathrm{kJ\,mol^{-1}}$ (Fig. 2.2). However, experiments conducted by Kamb (1961) have showed that for $n = 1$ or $n = 3$, there is no privileged direction of deformation on the basal plane and therefore for $1 \leq n \leq 3$, the basal plane is isotropic.

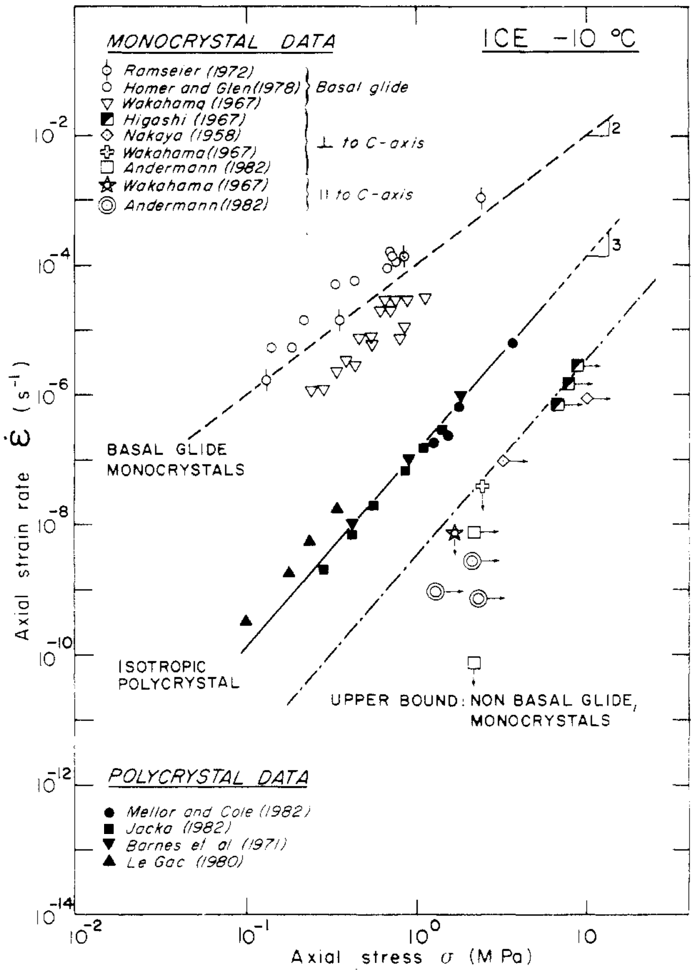

Figure 2.2: Relation between deformation rates and stresses obtained by laboratory experiments for isotropic ice and the monocrystal deformed by basal and non-basal glide (Duval and others, 1983)

2.2.2 Development of textures in polar ice

Due to the strong anisotropy of the monocrystal of ice, during deformation, the c-axis rotates towards and parallel to the axis of compression and away and perpendicular to the axis of traction (Fig. 2.3). The resulting distribution of c-axes is called ice fabric (polycrystal) and it represents the historical trajectory of an ice particle from the surface due to strain rates into an ice sheet. It is then natural to understand that the distribution of c-axes depends on the ice flow conditions. In a dome, the ice deforms mainly by uni-axial compression and the resulting measured fabric exhibits strong single maximum orientations with c-axes oriented towards the vertical. Such fabrics are well observed for the GRIP ice core in Greenland (Thorsteinsson and others, 1997), for Dome Fuji (Azuma and others, 1999) and Dome C (Wang and others, 2003) in Antarctica. Some examples of Schmidt diagrams measured for the GRIP ice core are shown in Figure 2.4.

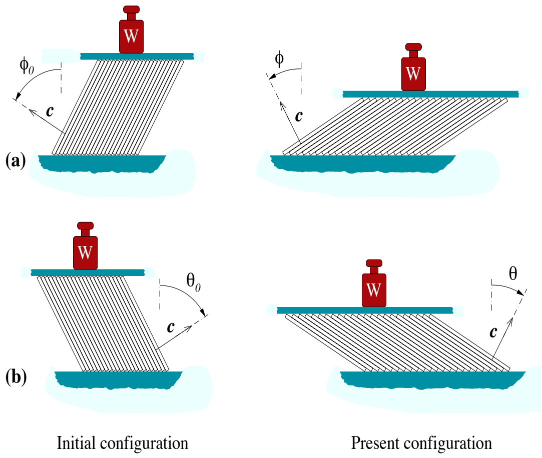

Figure 2.3: Ice crystal subjected to vertical compression due to the load W. The crystal deforms by basal slip, forcing the c-axis to rotated towards the axis of compression. The polycrystal of ice is expected to deform in a somewhat similar manner building a concentration of c-axes about the vertical (Placidi, 2004).

Several recrystallization process which affect the development of the fabric can be recognized in polar ice:

- the upper part (between 100 and 1000 m depth) of ice sheets is an area of normal growth of ice crystals. Under the influence of the decrease of the energy between grain boundaries, the averaged area of each grain tends to increase with time. There is no creation of new gains and the evolution of fabric is primarily driven by the rotation of grains by ice deformation. The normal growth of grains can slow down by impurities or particles contained into the ice.

- The intermediate part of ice sheets corresponds to a zone of normal grain growth and rotation recrystallization (polygonization). Polygonization is generally associated with the formation of sub-grain boundaries due to heterogeneous loading inside the polycrystal. This fragmentation process mainly affects grains that are not well oriented for dislocation glide, so-called hard grains. The resulting disorientation between grains can slow down the concentration under compression and eventually stop the normal grain growth of grains. This phenomenon has been for example observed for the GRIP ice core (Thorsteinsson and others, 1997) from 650 m depth. However this effect does not affect the normal grain growth for the case of Dome C as observed by (Durand and others, 2006a).

- At the lower part of ice-sheets, near the bedrock where the temperature and deformation are high, the recrystallization is the nucleation and growth of new grains called dynamic recrystallization. New grains well oriented for deformation appears and it is common to observe fabrics with the formation of several maximum of orientations or sudden de-concentration in those areas (Thorsteinsson and others, 1997). The fabric is then essentially controlled by the state of stress.

Due to the strong anisotropy of the monocrystal and the development of pronounced fabrics in the area of normal grain growth and polygonization, the ice polycrystal presents a strong anisotropic mechanical behavior, function of the fabric. In the area of dynamic recrystallization, as the fabric adapts almost instantaneously to the state of stress, the ice is sometimes considered as isotropic but with higher fluidity (Lliboutry and Duval, 1985) .

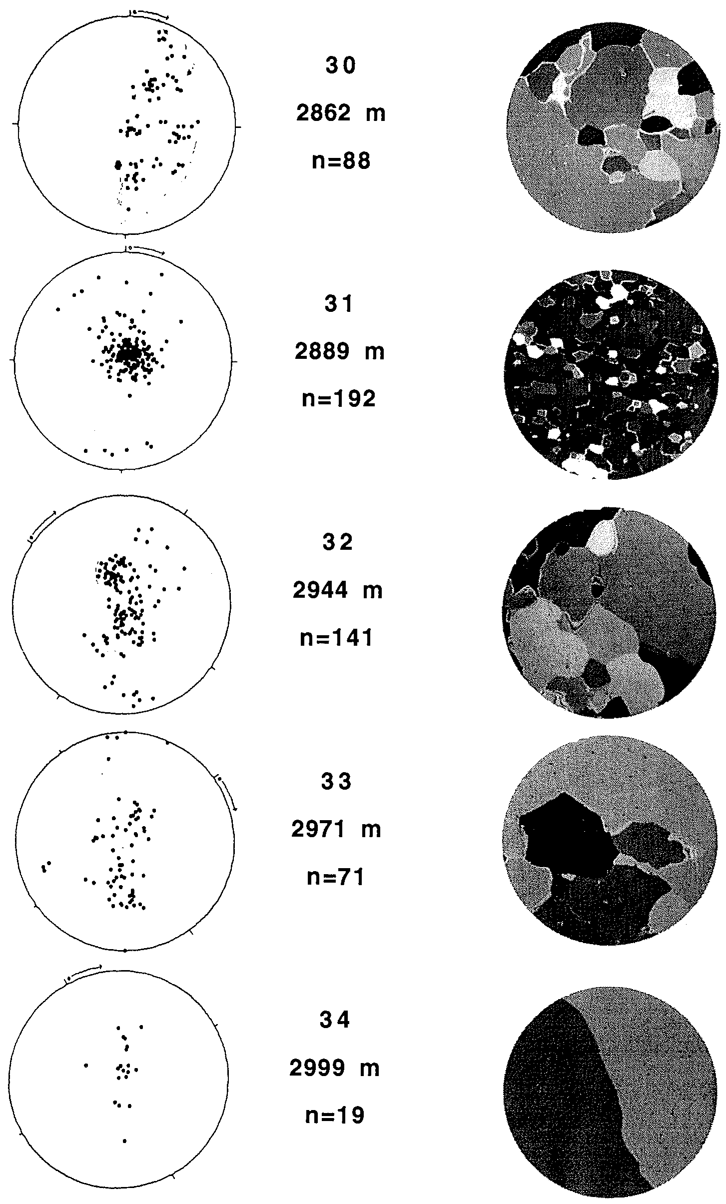

Figure 2.4: Fabric diagrams from c-axis orientation measurements obtained at the bottom of the GRIP ice core (Greenland). With each diagram, the thin section is presented and the diagrams are obtained from measurements on vertical sections (Thorsteinsson, 1996).

2.2.3 Ice polycrystal deformation

2.2.3.1 Isotropic polycrystal

The ice polycrystal deforms essentially by glide of dislocations. In the case of ice, the creep by diffusion is marginal because of the large size of crystals in natural ice and the low value of diffusion coefficients (Duval and others, 1983). Similarly, deformation by glide on grain boundaries is not an important process in the deformation of ice-sheets because it does not explain the formation of observed fabrics (Meyssonier and others, 2001). The creep of isotropic ice can be decomposed into three stages (Fig. 2.5),

- During the beginning of a creep test, the deformation rate presents a decreasing curve, this is the primary creep. The loading on the material results from the strong anisotropy of the monocrystal of ice. The development of dislocations near the grain boundaries due to the heterogeneity of the polycrystal results in the hardening of the material (Duval and others, 1983).

- The secondary creep (or stationary creep) corresponds to the phase where the material deforms at constant velocity. For the ice, this phase is short and the secondary creep is defined to be the minimum of the strain rate. The relation between the deformation rate D and the stress S is well described by power law of Norton-Hoff type, also known as Glen's law in glaciology. Let us briefly review the isotropic case, for which polycrystalline ice is treated as an incompressible, viscous fluid. The Cauchy stress tensor T is split up according to

$$\mathsf{T} = -p\mathsf{1} + \mathsf{S}, \qquad p = -\frac{1}{3}\mathrm{tr}\,\mathsf{T}, \tag{2.1}$$

where p denotes the pressure, and S is the traceless stress deviator ($\mathrm{tr}\,\mathsf{S} = 0$). The flow law only determines the stress deviator S and reads

$$\mathsf{S} = 2\eta\mathsf{D}, \tag{2.2}$$

where $\mathsf{D} = \mathrm{sym}\,\mathrm{grad}\,\mathbf{v}$ is the strain-rate tensor (symmetric part of the gradient of the velocity $\mathbf{v}$), and the coefficient η is the *shear viscosity* (or simply the *viscosity*). Its inverse, the *fluidity*, can be factorized as

$$\frac{1}{\eta} = 2EA(T')f(\sigma), \tag{2.3}$$

where

$$\sigma = \sqrt{\tfrac{1}{2}\,\mathrm{tr}\,(\mathsf{S}^2)} \tag{2.4}$$

is the *effective stress* (square root of the second invariant of the stress deviator), and the *creep function* $f(\sigma)$ is given by the power law

$$f(\sigma) = \sigma^{n-1} \tag{2.5}$$

(the parameter n is called "stress exponent"). Further, the *rate factor* $A(T')$ depends on the temperature relative to pressure melting $T' = T - T_\mathrm{m} + T_0$ (T: absolute temperature, T_m: pressure melting point, $T_0 = 273.15\,\mathrm{K}$) via the Arrhenius law

$$A(T') = A_0\, e^{-Q/RT'}, \tag{2.6}$$

where A_0 is the pre-exponential constant, Q the activation energy and $R = 8.314\,\mathrm{J\,mol^{-1}\,K^{-1}}$ the universal gas constant. The *flow enhancement factor* E is equal to unity for pure ice, and can be set to values deviating from unity in order to account roughly for effects of impurities and/or anisotropy (Paterson, 1991).

The isotropic flow law for ice is now obtained by inserting Eq. (2.3) [with the specifications of Eqs. (2.5) and (2.6)] in the viscous flow law (2.2). This yields

$$\mathsf{D} = EA(T')f(\sigma)\,\mathsf{S}, \tag{2.7}$$

which is called *Nye's generalization of Glen's flow law*, or *Glen's flow law* for short (e.g., Greve and Blatter (2008); Hooke (2005); Paterson (1994); Van der Veen (1999)). Suitable values for the several parameters are listed in Table 2.1.

Quantity	**Value**	
Stress exponent, n	3	
Pre-exponential constant, A_0	$3.985 \times 10^{-13}\,\mathrm{s^{-1}\,Pa^{-3}}$	(for $T' \le 263.15\,\mathrm{K}$)
	$1.916 \times 10^{3}\,\mathrm{s^{-1}\,Pa^{-3}}$	(for $T' > 263.15\,\mathrm{K}$)
Activation energy, Q	$60\,\mathrm{kJ\,mol^{-1}}$	(for $T' \le 263.15\,\mathrm{K}$)
	$139\,\mathrm{kJ\,mol^{-1}}$	(for $T' > 263.15\,\mathrm{K}$)

Table 2.1: Physical parameters for Glen's flow law.

In the usual conditions prevailing in ice sheets, the value of n is however uncertain and varies with the conditions of stress and temperature, and therefore with the depth. From ice layers inclination data, a value below 2 and closer to 1 has been proposed by Doake and Wolff (1985) and Lliboutry and Duval (1985). Form the study of bubbles densification in the Vostok ice core, Lipenkov and others (1997) proposed a value $n = 1$.

An uncertainty also exists for the activation energy. Budd and Jacka (1989) and Lliboutry and Duval (1985) have proposed a value of 60 $\mathrm{kJ\,mol^{-1}}$ for temperatures close to the melting point. However for stress and temperatures conditions ($\approx$ 263.15 K) during laboratory tests, values of 78 $\mathrm{kJ\,mol^{-1}}$ have been proposed. In this manuscript, we will used values presented in Table 2.1.

- When the minimum of deformation is reached, the deformation rate increases to reach a stead-sate. This phase, called the tertiary creep, starts with the beginning of the dynamic recrystallization (Lliboutry and Duval, 1985). Usually, the deformation in this phase can still be described by the Glen's law, but with a higher fluidity than the conditions prevailing in the secondary creep.

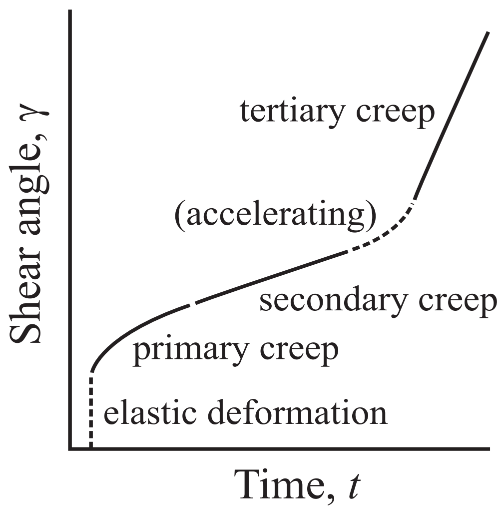

Figure 2.5: Representation of the different stages of polycrystalline ice creep (Greve, 2005)

2.2.3.2 Anisotropic polycrystal

Several tests have been performed on textured ice extracted from ice cores [Duval and Le Gac (1982); Pimienta (1987)]. The curve for the creep on textured ice presents the same three phases than the isotropic ice. Pimienta (1987) has however shown that for a texture with a single-maximum, the polycrystal is ten times easier to deform by shearing on the basal planes than in other directions. Those tests have therefore clearly shown the influence of the fabric on the mechanical behavior of the polycrystal.

2.3 Modeling polar ice

2.3.1 The monocrystal of ice

2.3.1.1 Models of grains with gliding planes

In those models, the deformation results from the glide of crystallographic planes in different directions. The rate of deformation in case of shearing parallel to those planes depends on the scission resolved on the planes and on the hardness of each plane. In case of the monocrystal of ice, most of authors assumed that the glide occurs only on the basal plane [Lliboutry (1993); Azuma and Goto-Azuma (1996); Svendsen and Hutter (1996); Gödert and Hutter (1998); Thorsteinsson (2001)]. The inconvenient of this assumption is that the grain can not deform in all directions. Castelnau and others (1996b) have considered the glide on basal, prismatic and pyramidal planes to overcome this problem and have noticed that the prismatic and pyramidal planes are 70 times harder to deform than the basal planes.

2.3.1.2 Models with continuous grains

Such models have been proposed for example by Meyssonier and Philip (1996) by assuming transverse isotropy for the monocrystal of ice. The deformation law that connects rate deformations D and stresses S is assumed to be linear and is build based on representation theorems of Boehler (1978) objective tensorial function. The anisotropy is then function of two scalar parameters and the reorientation of grains is obtained by assuming that grains deforms essentially by basal glides. An extension taking into account non-linearity has been proposed by Gagliardini (1999).

2.3.2 The fabric

Two types of the fabric description are generally used in glaciology. The discrete description consists on defining a given number of grains N_g, each grain having its own orientation and volumic fraction. With this description, deformations and stresses are computed for each grain, which may result in large required computing time and number of variables.

An alternative method is based on a continuous description of the fabric, where orientation distribution function or an orientation tensors are used for the description of crystal orientations. The advantage of those methods is that they allow for reducing the number of variables to describe the fabric and in some case analytical solutions can be derived. Those description will be further studied in details in the following chapters.

2.3.3 The ice polycrystal

Three types of models for the simulation of the ice polycrystal have been proposed in order to overcome the unsuited isotropic Glen's flow law when ice sheets flow is modeled. Polar ice being strongly textured, the assumption of isotropy for polar ice has became inadequate for the proper modeling of the mechanical deformation of ice in ice sheets.

2.3.3.1 Phenomenological models

This approach tries to construct a macroscopic anisotropic law for the deformation of ice by either identifying the parameters of this law with mechanical laboratory tests [Le Gac (1980); Pimienta (1987)] or by comparison with anisotropic models (Gillet-Chaulet and others, 2005).

In the phenomenological model proposed by Morland and Staroszczyk (1998), the mechanical anisotropic behavior of ice is described by a tensorial objective function (Boehler, 1978) which depends on the deformation rate, the deformation and three structural tensors. The anisotropy is then described by phenomenological functions of the deformation with the shortcoming that fabrics are assumed transversely isotropic or orthotropic. Another phenomenological model has been proposed by Placidi and Hutter (2006a) where analytical solutions are derived for particular fabrics by assuming homogeneous stresses in the polycrystal and collinearity between deformation rates and stresses.

2.3.3.2 Homogenization models

Also called Micro-Macro models, this approach proposed to derive the macroscopic behavior of the polycrystal from the microscopic behavior of its constituents. Those models are based on several type of interactions between each grain and the polycrystal with the assumption that deformation rates and stresses are homogeneous inside the grain (they can be interpreted as being average of the real deformation rates and stresses inside the grain). These models can be divided into three types

- The Taylor models where deformation rates are assumed homogeneous in each grain and equal to the macroscopic deformation rates.

- The Static model where stresses are assumed homogeneous in each grain and equal to the macroscopic stresses.

- The Auto-Coherent models which introduces an interaction equation between the grain and the equivalent homogeneous medium. They result in an intermediate behavior between Taylor and Static models.

Different version of those models have been proposed to compute the anisotropic behavior of ice and the evolution of fabrics. The Static model is certainly the mostly used [Lliboutry (1993); Castelnau and Duval (1994); Svendsen and Hutter (1996); Gödert and Hutter (1998); Gagliardini (1999); Thorsteinsson (2001)] sometime by also taking into account the recrystallization (Van der Veen and Whillans, 1994) or the interaction between grains (Thorsteinsson, 2002). “1-site” Auto-Coherent models have been developed and applied to ice by Castelnau (1996), Meyssonier and Philip (1996) and Montagnat Rentier (2001). Auto-Coherent models are also classically used in metallurgy (Lebensohn and Tomé, 1993) and to calculate the texture of rocks in the terrestrial mantle (Tommasi and others, 2000).

More recently, Faria (2006a) ; Faria and others (2006); Faria (2006b); Placidi (2004) and Placidi and Hutter (2006a) have adapted the theory of mixture with continuous diversity to polycrystalline ice with a continuous approach of the diversity of constituents. The continuous approach does not consider a given finite number of discrete constituents, but a continuous representation of the density of the diversity on all possible diversities.

The anisotropic flow law presented in this manuscript is derived from the formulation proposed by Placidi (2004).

2.3.3.3 Complete models

Those models entirely solve the equations governing the deformation in a polycrystal: the balance equation in each grain and the compatibility equation for deformations. The finite-element model of Mansuy (2001) or the FFT (Fast Forrier Transform) model of Montagnat Rentier (2001) are examples of such approach. The main disadvantage of those models is that they are computationally expensive to use and are generally limited for simple 2D cases. However, they allow the precise understanding of the non-homogeneous deformations and stresses inside each grain.

2.4 Ice sheet flow modeling

Modeling ice sheets flow can be motivated by two research perspectives. Modeling the entire ice-sheets (Antarctica and Greenland) allows the understanding of their past and future evolution. Due to the involved time and space scales, those models requires simplifications in order to reduce the computing time. They are based on the shallow-ice approximation. The second type of models have objectives to better understand the flow conditions at the vicinity of ice core drilling boreholes. Those models solves all equations that govern ice deformation and flow.

2.4.1 The shallow-ice approximation

The equations that govern the ice flow are developed with the consideration of ice sheets aspect ratio $\epsilon = H/L$, where H is the ice thickness and L is the horizontal extent. The parameter ϵ is generally very small so that simplified equation for the ice flow can be derived [Hutter (1983); Greve (1997)]. Models formulated with this approach use a zero order approximation in ϵ which neglects the longitudinal stresses and computes the bedrock parallel shear stresses which are dependent on the local topography. This approximation is valid on locations far away from domes and for small variations of the geometry (surface and bedrock) respective to the ice thickness.

2.4.2 Higher order models

The majority of models that solve the entire equations that govern ice motion are based on the finite-element method. Other methods have however been used, namely the finite volume method (Deponti and others, 2006) and the finite difference method (Mangeney, 1996). Another approach proposed by Pattyn (2003) is also an higher order model but with hypothesis aimed at simplifications: the vertical longitudinal stress is assumed equal to the hydrostatic pressure and the horizontal gradient of the vertical velocity is assumed small respective to the gradients of the horizontal velocity.

Higher models have generally been applied for synthetical tests in order to investigate the effect of longitudinal stresses on ice flow were the shallow ice approximation is not valid, notably near domes [Mangeney and others (1996); Hvidberg (1996); Pettit and Waddigton (2003)].

Several applications have also been carried out for the simulation of the flowline joining the drilling sites GRIP and GISP2 in Greenland [Mangeney (1996); Hvidberg and others (1996); Gagliardini and Meyssonnier (2000)]. Those simulations have showed the limits of uni-directional modeling used for dating the GRIP ice core (Dahl-Jensen and others, 1993). Martin and others (2006) have used their thermo-mechanical isotropic model for the reconstruction of Raymond arks (Raymond, 1983) where the bumps amplitude were only reproducible for high stress exponent ($n = 4$), while however Pettit (2003) has showed that anisotropy plays a role in the amplitudes of Raymond arks.

Models that use an anisotropic flow law but with a fixed fabric (the anisotropy does not evolve with deformation) have also been proposed [Mangeney (1996); Pettit (2003)]. Among models that implement the evolution of induced anisotropy, we can mention the work of Staroszczyk and Morland (2000) based on the phenomenological law of Morland and Staroszczyk (1998), or the models of Gagliardini (1999) and Gödert and Hutter (1998) which use a micro-macro approach with an ODF description of the fabric. Those models have showed that for a flat bedrock, the anisotropy is favorable to the shear deformation of the polycrystal so that the the deformation and the flow velocity are higher at the ice sheet base than in isotropic conditions. On sinusoidal bedrock, Mangeney (1996) observed with a anisotropic flow law, an acceleration of the flow at the top of bumps and a deceleration in cavities.

2.5 Conclusion

We have presented in this chapter the mechanisms of polar ice deformation. By considering different scales, the monocrystal of ice, the development of textures and the ice polycrystal, we have showed the complexity of modeling the ice deformation and ice flow in ice sheets. Combined with the need to construct large scale models of ice sheets, precise ice flow modeling with realistic computing time has become an issue. However those considerations are important for the better understanding of ice sheet dynamics and therefore they will be addressed in this study.

Combined with a large scale modeling at the vicinity of Dome Fuji, we propose an implementation of a anisotropic flow law that takes into account the flow induced anisotropy in ice and the fabric evolution with a continuum approach. This law will be implemented in a finite element thermo-mechanical flow model with the perspective to better understand the dynamics at Dome Fuji.

Chapter 3

A continuum-mechanical model for ice anisotropy and fabric evolution based on an anisotropic flow enhancement factor

3.1 Introduction

In this chapter, we present the CAFFE model and its mathematical formulation. We start by formulating the deformation of a polycrystal which we generalize for the polycrystal ice afterwards. The inversion of the flow law in then presented before to formulate the fabric evolution equation. There, we present the equations that take into account grain rotation due to deformation and the recrystallization processes that occur in ice-sheets.

3.2 Deformation of a single crystal in the polycrystalline aggregate

In order to motivate the anisotropic generalization of Glen's flow law (2.7), let us first consider the deformation of a single crystal embedded in the polycrystalline aggregate. Following Placidi and others (2008), only the dominant deformation along the basal plane is accounted for, whereas deformations along prismatic and pyramidal planes, which are up to 60 times smaller in the temperature range of $210\,\mathrm{K} < T < 273.16\,\mathrm{K}$, shall be neglected (Fig. 3.1).

Let $\mathbf{n}$ be the normal unit vector of the basal plane (direction of the c-axis), then $\mathsf{S}\mathbf{n}$ is the resolved deviatoric stress vector (Fig. 3.2). Note that the tensor S is interpreted

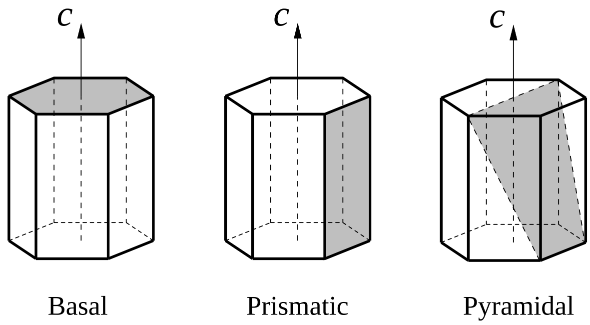

Figure 3.1: Basal, prismatic and pyramidal glide planes in the hexagonal ice-Ih crystal, sketched as a right hexagonal prism (Faria, 2003).

as the *macroscopic* stress deviator which does not depend on the orientation $\mathbf{n}$. It is reasonable to assume that only the stress component S_t tangential to the basal plane (resolved shear stress) contributes to its shear deformation, while the component normal to the basal plane has no effect.

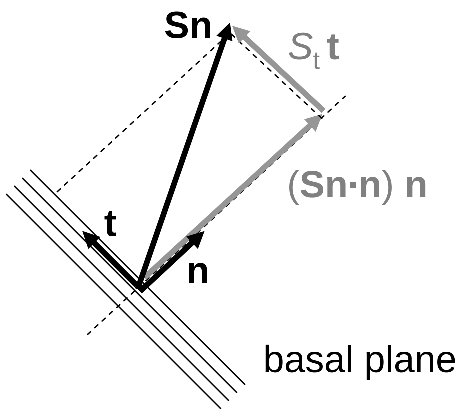

Figure 3.2: Decomposition of the deviatoric stress vector into a part normal and a part tangential to the basal plane.

According to Fig. 3.2, the decomposition of the stress vector reads

$$\mathsf{S}\mathbf{n} = (\mathsf{S}\mathbf{n} \cdot \mathbf{n})\mathbf{n} + S_\mathrm{t}\mathbf{t}, \tag{3.1}$$

where $\mathbf{t}$ denotes the tangential unit vector. As mentioned above, deformation of the single crystal in the polycrystalline aggregate is attributed to the tangential component S_t only. Since we aim at a theory which describes the effects of anisotropy by a *scalar*, anisotropic flow enhancement factor, we define the scalar invariant

$$S_\mathrm{t}^2 = \mathsf{S}\mathbf{n} \cdot \mathsf{S}\mathbf{n} - (\mathsf{S}\mathbf{n} \cdot \mathbf{n})^2. \tag{3.2}$$

This quantity has the unit of a stress squared, and so a natural way to non-dimensionalize it is by the square of the effective stress σ, which is also a scalar invariant. Thus, we introduce the *deformability* of a single crystal in the polycrystalline aggregate, which is loaded by the deviatoric stress S, as

$$\mathcal{A}^\star(\mathbf{n}) = \frac{5}{2}\,\frac{S_\mathrm{t}^2(\mathbf{n})}{\sigma^2} = 5\,\frac{\mathsf{S}\mathbf{n}\cdot\mathsf{S}\mathbf{n} - (\mathsf{S}\mathbf{n}\cdot\mathbf{n})^2}{\mathrm{tr}\,(\mathsf{S}^2)}. \tag{3.3}$$

The factor 5/2 has been introduced merely for reasons of convenience, as it will become clear below.

3.3 Flow law for polycrystalline ice

In polycrystalline ice, the crystals within a control volume (which is assumed to be large compared to the crystal dimensions, but small compared to the macroscopic scale of ice flow) show a certain fabric. Extreme cases are on the one hand the single maximum fabric, for which all c-axes are perfectly aligned, and on the other hand the isotropic fabric with a completely random distribution of the c-axes. A general fabric, which is usually in between these cases, can be described by the *orientation mass density* (OMD) $\rho^\star(\mathbf{n})$. It is defined as the mass per volume and orientation, the latter being specified by the normal unit vector (direction of the c-axis) $\mathbf{n} \in S^2$ (S^2 is the unit sphere). Evidently, when integrated over all orientations, the OMD must yield the normal mass density ρ, which leads to the normalization condition

$$\int\limits_{S^2} \rho^\star(\mathbf{n})\,\mathrm{d}^2 n = \rho. \tag{3.4}$$

Alternatively, an *orientation distribution function* (ODF) $f^\star(\mathbf{n})$ can be defined as

$$f^\star(\mathbf{n}) = \frac{\rho^\star(\mathbf{n})}{\rho}, \tag{3.5}$$

which is normalized to unity when integrated over all orientations.

We use the ODF in order to define the *deformability* of polycrystalline ice by weighting the deformability of the single crystal (3.3),

$$\mathcal{A} = \int\limits_{S^2} \mathcal{A}^\star(\mathbf{n})\,f^\star(\mathbf{n})\,\mathrm{d}^2 n = \frac{5}{2}\int\limits_{S^2} \frac{S_\mathrm{t}^2(\mathbf{n})}{\sigma^2} f^\star(\mathbf{n})\,\mathrm{d}^2 n = 5\int\limits_{S^2} \frac{\mathsf{S}\mathbf{n}\cdot\mathsf{S}\mathbf{n} - (\mathsf{S}\mathbf{n}\cdot\mathbf{n})^2}{\mathrm{tr}\,(\mathsf{S}^2)} f^\star(\mathbf{n})\,\mathrm{d}^2 n. \tag{3.6}$$

Note that, for the isotropic case, the ODF is $f^\star(\mathbf{n}) = 1/(4\pi)$, and from Eq. (3.6) we obtain a deformability of $\mathcal{A} = 1$ (Placidi and others, 2008). For that reason, the factor 5/2 has been introduced in Eq. (3.3).

The envisaged flow law for anisotropic polar ice can now be formulated. Essentially, we keep the form of the Glen's flow law (2.7), but with a scalar, anisotropic enhancement factor $\hat{E}(\mathcal{A})$ instead of the parameter E,

$$\mathsf{D} = \hat{E}(\mathcal{A})\, A(T')\, \sigma^{n-1}\, \mathsf{S}. \tag{3.7}$$

The viscosity η is therefore

$$\frac{1}{\eta} = 2\hat{E}(\mathcal{A})\, A(T')\, \sigma^{n-1}. \tag{3.8}$$

The function $\hat{E}(\mathcal{A})$ is supposed to be strictly increasing with the deformability $\mathcal{A}$, and has the fixed points

$$\begin{aligned} \hat{E}(0) &= E_{\min} && \text{(uniaxial compression on single maximum),} \\ \hat{E}(1) &= 1 && \text{(arbitrary stress on isotropic fabric),} \\ \hat{E}(\tfrac{5}{2}) &= E_{\max} && \text{(simple shear on single maximum).} \end{aligned} \tag{3.9}$$

The "hard" case $(3.9)_1$ and the "soft" case $(3.9)_3$ are illustrated in Fig. 3.3. Note also that the deformability cannot take values larger than $\mathcal{A} = 5/2$ (Placidi and others, 2008).

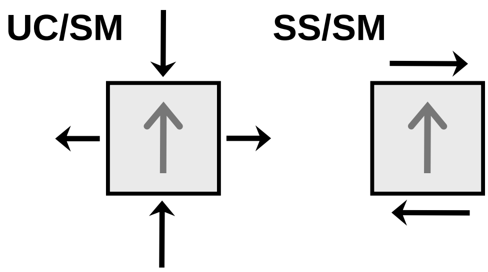

Figure 3.3: Uniaxial compression on single maximum (UC/SM) and simple shear on single maximum (SS/SM) for a small sample of polycrystalline ice. Stresses are indicated as black arrows, and the single maximum fabric is marked by the dark-grey arrows within the ice sample.

For the detailed form $\hat{E}(\mathcal{A})$ of the anisotropic enhancement factor, in addition to Eq. (3.9), we demand that the function is continuously differentiable, that is, $\hat{E} \in C^1[0, \frac{5}{2}]$. Moreover, Azuma (1995) and Miyamoto (1999) have experimentally verified that the enhancement factor depends on the Schmidt factor (resolved shear stress) to the fourth power, that is, on the square of the deformability $\mathcal{A}$. This yields

$$\hat{E}(\mathcal{A}) = \begin{cases} E_{\min} + (1 - E_{\min})\mathcal{A}^t, \quad t = \dfrac{8}{21}\,\dfrac{E_{\max} - 1}{1 - E_{\min}}, & 0 \leq \mathcal{A} \leq 1, \\[2ex] \dfrac{4\mathcal{A}^2(E_{\max} - 1) + 25 - 4E_{\max}}{21}, & 1 \leq \mathcal{A} \leq \dfrac{5}{2} \end{cases} \tag{3.10}$$

[for details see Placidi and others (2008)]. Investigations by Pimienta and others (1987) indicate that the parameter $E_{\max}$ (maximum softening) is approximately equal to ten, whereas Jacka and Budd (1989) report a value of about eight. The parameter $E_{\min}$ (maximum hardening) can be realistically chosen between zero and one tenth, a non-zero value serving mainly the purpose of avoiding numerical problems. The function (3.10) is shown in Fig. 3.4.

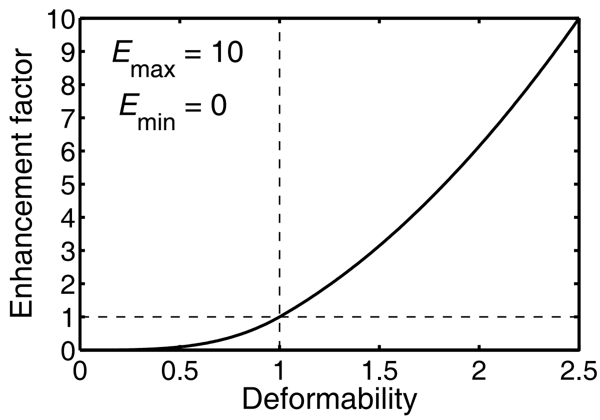

Figure 3.4: Anisotropic enhancement factor $\hat{E}(\mathcal{A})$ as a function of the deformability $\mathcal{A}$ according to Eq. (3.10), for $E_{\max} = 10$ and $E_{\min} = 0$.

3.4 Inversion of the flow law

The anisotropic flow law (3.7) can be inverted analytically. We find

$$\mathsf{S} = [\hat{E}(\mathcal{A})]^{-1/n}\,[A(T')]^{-1/n}\,d^{-(1-1/n)}\,\mathsf{D}, \tag{3.11}$$

where $d = \sqrt{\frac{1}{2}\,\mathrm{tr}\,(\mathsf{D}^2)}$ is the *effective strain rate*. The deformability $\mathcal{A}$ also needs to be expressed by strain rates instead of stresses [see Eq. (3.6)]. In analogy to Eq. (3.1), we consider the resolved strain-rate vector $\mathsf{D}\mathbf{n}$ in a single crystal in the polycrystalline aggregate, and decompose it according to

$$\mathsf{D}\mathbf{n} = (\mathsf{D}\mathbf{n} \cdot \mathbf{n})\mathbf{n} + D_\mathrm{t}\mathbf{t}, \tag{3.12}$$

where D_t is the resolved shear rate in the basal plane (see also Fig. 3.2). As in Eq. (3.2), we define the scalar invariant

$$D_\mathrm{t}^2 = \mathsf{D}\mathbf{n}\cdot\mathsf{D}\mathbf{n} - (\mathsf{D}\mathbf{n}\cdot\mathbf{n})^2. \tag{3.13}$$

Owing to the collinearity of the tensors S and D [see Eqs. (3.7) and (3.11)], the deformability of polycrystalline ice can be readily expressed by D_t and d,

$$\mathcal{A} = \frac{5}{2}\int\limits_{S^2} \frac{D_\mathrm{t}^2(\mathbf{n})}{d^2} f^\star(\mathbf{n})\,\mathrm{d}^2n = 5\int\limits_{S^2} \frac{\mathsf{D}\mathbf{n}\cdot\mathsf{D}\mathbf{n} - (\mathsf{D}\mathbf{n}\cdot\mathbf{n})^2}{\mathrm{tr}\,(\mathsf{D}^2)} f^\star(\mathbf{n})\,\mathrm{d}^2n, \tag{3.14}$$

which completes the inversion of the anisotropic flow law. With Eqs. (3.11) and (3.14), the viscosity η reads

$$\eta = \frac{1}{2}[\hat{E}(\mathcal{A})]^{-\frac{1}{n}}\,[A(T')]^{-\frac{1}{n}}\,d^{-(1-\frac{1}{n})}. \tag{3.15}$$

3.5 Evolution of anisotropy

3.5.1 Orientation mass balance

The anisotropic flow law of the CAFFE model in the form (3.7) or (3.11) needs to be complemented by an evolution equation for the anisotropic fabric. This is done by formulating the *orientation mass balance* for the OMD $\rho^\star(\mathbf{n})$,

$$\frac{\partial\rho^\star}{\partial t} + \mathrm{div}\,(\rho^\star\mathbf{v}) + \mathrm{div}_{S^2}(\rho^\star\mathbf{u}^\star + \mathbf{q}^\star) = \rho^\star\Gamma^\star \tag{3.16}$$

(Placidi and others, 2008). In this equation, div is the normal, three-dimensional divergence operator, div_{S^2} the divergence operator on the unit sphere, $\mathbf{u}^\star(\mathbf{n})$ the orientation transition rate, $\mathbf{q}^\star(\mathbf{n})$ the orientation flux and $\Gamma^\star(\mathbf{n})$ the orientation production rate. The orientation transition rate corresponds to grain rotation, the orientation flux to rotation recrystallization (polygonization), and the orientation production rate to migration recrystallization and all other processes in which the transport of mass from one grain, having a certain orientation, to another grain, having a different orientation, cannot be neglected. Mass conservation requires

$$\int\limits_{S^2} \rho^\star(\mathbf{n})\,\Gamma^\star(\mathbf{n})\,\mathrm{d}^2n = 0. \tag{3.17}$$

Note also that the velocity $\mathbf{v}$ is assumed to be independent on the orientation $\mathbf{n}$.

In order to solve the orientation mass balance (3.16), constitutive relations for the orientation transition rate $\mathbf{u}^\star(\mathbf{n})$, the orientation flux $\mathbf{q}^\star(\mathbf{n})$ and the orientation production rate $\Gamma^\star(\mathbf{n})$ need to be provided as closure conditions.

3.5.2 Constitutive relation for the orientation transition rate

As mentioned above, the orientation transition rate corresponds physically to grain rotation. Since grain rotation is induced by shear deformation in the basal plane, in the CAFFE model it is controlled by the resolved shear rate $D_\mathrm{t}\mathbf{t}$ [Eq. (3.12)], and the relation

$$\mathbf{u}^\star = -\iota\, D_\mathrm{t}\mathbf{t} + \mathsf{W}\mathbf{n} = \iota \cdot [(\mathsf{D}\mathbf{n}\cdot\mathbf{n})\mathbf{n} - \mathsf{D}\mathbf{n}] + \mathsf{W}\mathbf{n} \tag{3.18}$$

is employed (see e.g. Dafalias, 2001), where the parameter ι is a positive constant. The additional term $\mathsf{W}\mathbf{n}$ with the spin tensor $\mathsf{W} = \operatorname{skw}\operatorname{grad}\mathbf{v}$ (skew-symmetric part of the gradient of the velocity $\mathbf{v}$) describes the contribution of local rigid-body rotations.

In the special case $\iota = 1$, the basal planes are material area elements, that is, they carry out an affine rotation. However, due to geometric incompatibilities of the deformation of individual crystals in the polycrystalline aggregate, an affine rotation is not plausible, and we expect realistic values of ι to be less than unity.

3.5.3 Constitutive relation for the orientation flux

The orientation flux is supposed to describe rotation recrystallization (polygonization). Following the argumentation by Gödert (2003), it is modeled as a diffusive process,

$$\mathbf{q}^\star(\mathbf{n}) = -\lambda\,\mathrm{grad}_{S^2}[\rho^\star(\mathbf{n})\mathcal{H}^\star(\mathbf{n})], \tag{3.19}$$

where the parameter $\lambda > 0$ is the orientation diffusivity, grad_{S^2} is the gradient operator on the unit sphere, and the "hardness" $\mathcal{H}^\star(\mathbf{n})$ is a monotonically decreasing function of the single-crystal deformability $\mathcal{A}^\star(\mathbf{n})$ [see Eq. (3.3)]. A simple choice for the hardness function would therefore be

$$\mathcal{H}^\star(\mathbf{n}) = \frac{1}{\mathcal{A}^\star(\mathbf{n}) + \epsilon}, \tag{3.20}$$

the offset $\epsilon \ll 1$ being introduced in order to prevent a singularity for $\mathcal{A}^\star = 0$. However, recent results by Durand and others (2008) suggest that rotation recrystallization is an isotropic process not affected by the orientation. In this case, the choice

$$\mathcal{H}^\star(\mathbf{n}) \equiv 1 \tag{3.21}$$

is indicated, which renders Eq. (3.19) equivalent to Fick's laws of diffusion on the unit sphere.

3.5.4 Constitutive relation for the orientation production rate

The driving force for the orientation production rate, which models essentially migration recrystallization, are macroscopic deformations of the polycrystal, which can be more easily followed on the microscopic scale by grains oriented favorably for the given deformation. Therefore, it is reasonable to assume that the orientation production rate for a certain orientation $\mathbf{n}$ is related to the deformation resolved in the basal plane. Since the orientation production rate is a scalar quantity, the CAFFE model uses the scalar invariant D_t^2 [Eq. (3.13)] as a deformation measure, and the relation

$$\Gamma^\star = \Gamma \cdot (D_\mathrm{t}^2 - \langle D_\mathrm{t}^2 \rangle), \qquad \langle D_\mathrm{t}^2 \rangle = \int\limits_{S^2} \frac{\rho^\star}{\rho} D_\mathrm{t}^2 \, \mathrm{d}^2 n \tag{3.22}$$

is formulated. Subtraction of the averaged scalar invariant $\langle D_\mathrm{t}^2 \rangle$ is required in order to fulfill the mass-conservation condition (3.17). The parameter Γ is again assumed to be a positive constant. This guarantees a positive mass production for favorably oriented grains, and a negative production for unfavorably oriented grains (Fig. 3.5).

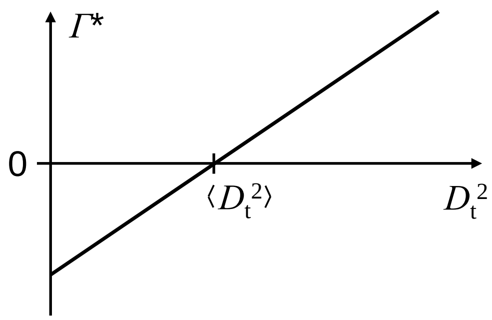

Figure 3.5: Orientation production rate according to Eq. (3.22).

3.6 Conclusion

We have presented in this chapter the theoretical background for modeling ice anisotropy and fabric evolution. A continuum-mechanical model based on a flow enhancement factor is derived that allows for modeling flow induced ice anisotropy by using a crystal orientation dependent scalar that computes the polycrystal deformability. The ice fabric evolution is modeled by means of the variation of a mass orientation density that takes into account deformation induced crystal rotation and recrystallization processes (rotation and migration recrystallization). In the next chapter, we propose the application of the CAFFE model to the EDML ice core in order to assess the performance of the theoretical formulation.

Chapter 4

Anisotropic flow and fabric evolution modeling: application to the EDML core, Antarctica, by means of a one dimensional flow model

4.1 Introduction

The application of the continuum-mechanical model formulated in the previous chapter is considered in this chapter with the development of a one-dimensional model applied the site of the EPICA (European Project for Ice Coring in Antarctica) deep ice core at Kohnen Station in Dronning Maud Land, East Antarctica ("EDML core", 75°00′06″S,00°04′04″E, 2892 meters above sea level; see http://www.awi-bremerhaven.de/Polar/Kohnen/). For this core with an overall length of 2774 m, preliminary fabric data are available from 50 m until 2570 m depth, and its location on a flank (rather than a dome like most other ice cores) allows deriving a one-dimensional flow model based on the shallow-ice approximation [Hutter (1983); Morland (1984)], with which the performance of the CAFFE model can be tested. We start in this chapter by a brief description of the fabrics data obtained at EDML. The field equations developed for the model and the numerical implementation are then discussed before presenting the results where we have considered three different solution methods, (i) computing the ice flow based on the flow law of the CAFFE model and the measured fabrics, (ii) solving the CAFFE fabric evolution equation under the simplifying assumption of transverse isotropy, and (iii) solving the unrestricted CAFFE fabric evolution equation. The independence of the results to the employed numerical method and the stability of the anisotropic flow law are then discussed.

4.2 Fabric data

Preliminary fabric data of the EDML core were measured in 2005 down to 2570 m depth in a −20°C ice laboratory at the Alfred Wegener Institute for Polar and Marine Research, Breherhaven, Germany,. Samples were drilled between 2001 and 2004 and have been stored at −30°C after the transportation at −10°C to Bremerhaven. Thin sections were prepared according to standard procedures using a microtome from horizontally ($\sim 0.5 \times 50 \times 50$ mm) and vertically cut samples ($\sim 0.5 \times 50 \times 100$ mm). C-axes orientations were derived using an automatic fabric analyzer system (Wilson and others, 2003) which enables complete measurements of these samples in 15 to 30 minutes.

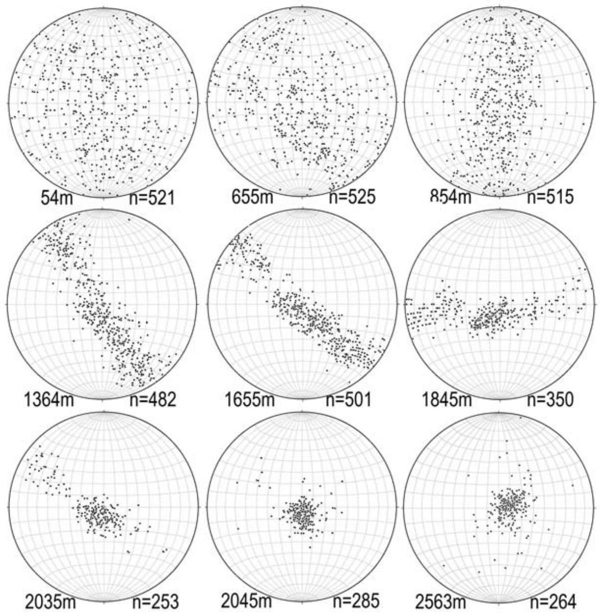

Figure 4.1: Selected Schmidt diagrams for the observed fabrics of the EDML ice core between 54 m and 2563 m depth. Centers of diagrams coincide with the core axis. All examples displayed here are from vertically cut thin sections, rotated to horizontal view. n denotes the number of grains included. Note that the orientations of the horizontal planes with respect to the ice-flow direction are unknown (courtesy Hamann, I.).

The data are still preliminary because local effects due to immatureness of the system need to be explained completely and solved. However, the impact on the statistics of local unknown effects was checked by repeated measurements with changing sample orientations and could be proved to be negligible. Among 60 to 600 grains per thin section, approx. 5 to 10 grains show these effects. The complete data set and its detailed interpretation are presented in Hamann and others (2008).

In Fig. 4.1, the preliminary fabric data of the EDML core are visualized as Schmidt diagrams for selected depths. The fabrics show a gradual transition from randomly oriented c-axes in shallower depths (down to 600 m) to a broad vertical girdle fabric (approx. 600 to 1000 m depth). A small, however systematic difference in the largest eigenvalues of the second-order orientation tensor $\mathsf{a}^{(2)}$ [defined as the second moment of the ODF, $\mathsf{a}^{(2)} = \int_{S^2}(\mathbf{n}\otimes\mathbf{n})\, f^{\star}(\mathbf{n})\,\mathrm{d}^2 n$] between horizontal and vertical cut sections in the girdle fabric region (approx. 450 to 1350 m depth) cannot be explained yet. A narrowing of the girdle fabric follows (approx. 2000 m depth). A sudden change in the flow regime is indicated by an abrupt (in between 10 m) vertical alignment of the c-axes to a single maximum (2040 m depth). Tendencies of second or multiple maxima can be observed at several depths.

4.3 One-dimensional flow model

We define a local Cartesian coordinate system such that Kohnen Station is located at the origin, the x-axis points in the 260° (WSW) direction, the y-axis in the 170° (SSE) direction, and z (depth) points vertically downward (Fig. 4.2). According to the topographical data by Wesche and others (2007), the x-axis is approximately aligned with the downhill direction, and the gradient of the free surface elevation, h, is

$$\frac{\partial h}{\partial x} = -9 \times 10^{-4} \pm 10\%, \qquad \frac{\partial h}{\partial y} = 0. \tag{4.1}$$

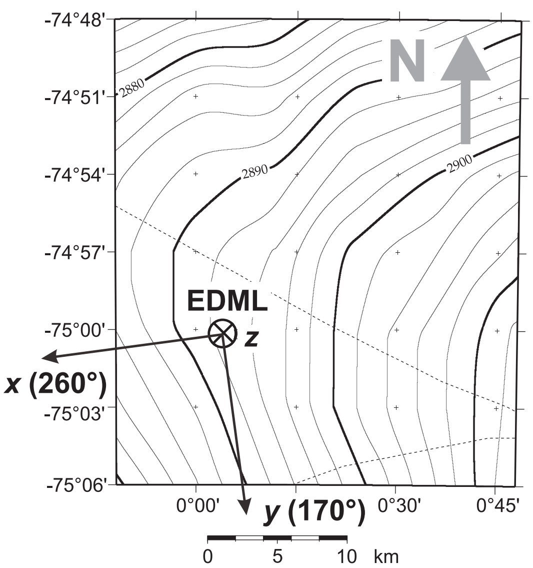

Figure 4.2: Local coordinate system for the EDML site. Underlaid topography map by Wesche and others (2007).

Thus, in the shallow-ice approximation, the only non-vanishing bed-parallel shear-stress component is S_{xz}, given by

$$S_{xz} = \rho g z \frac{\partial h}{\partial x}, \tag{4.2}$$

where g is the acceleration due to gravity. Combination with the x-z-component of the Glen's flow law (2.7) yields the isotropic horizontal velocity,

$$v_x = -2\rho g \frac{\partial h}{\partial x} \int_z^H A(T')\, \sigma^{n-1}\, \bar{z}\, \mathrm{d}\bar{z} \tag{4.3}$$

[Greve (1997); Greve and Blatter (2008)], where H is the ice thickness, the rate factor $A(T')$ and stress exponent n are chosen as listed in Sect. 2.2.3.1, and the enhancement factor E has been set to unity. Similarly, for anisotropic conditions and the corresponding flow law (3.7), the horizontal velocity is

$$v_x = -2\rho g \frac{\partial h}{\partial x} \int_z^H \hat{E}(\mathcal{A})\, A(T')\, \sigma^{n-1}\, \bar{z}\, \mathrm{d}\bar{z}, \tag{4.4}$$

with the enhancement factor function $\hat{E}(\mathcal{A})$ of Eq. (3.10). Note that no-slip conditions have been assumed at the ice base, that is, $v_x(z=H) = 0$.

The unknowns in Eq. (4.4) are the normal deviatoric stresses (S_{xx}, S_{yy}, S_{zz}) which are required together with the shallow-ice shear stress (4.2) for computing the deformability $\mathcal{A}$ by Eq. (3.6), and then the enhancement factor $\hat{E}(\mathcal{A})$ by Eq. (3.10). The normal deviatoric stresses are computed by application of the inverse anisotropic flow law (3.11) with the deformability in the form (3.14). The latter is evaluated with the calculated shallow-ice deformations and an assumed vertical strain rate D_{zz} in the form of a Dansgaard-Johnsen type distribution (Dansgaard and Johnsen, 1969), which consists of a constant value of D_{zz} from the free surface down to two thirds of the ice thickness, and a linearly decreasing value of D_{zz} below. A similar distribution is employed for the temperature profile (see Fig. 4.3). Horizontal extension is parameterized by

$$D_{xx} = -aD_{zz}, \quad D_{yy} = -(1-a)D_{zz}, \tag{4.5}$$

where the parameter a is equal to 1/2 for isotropic extension in the horizontal plane, and equal to unity for extension in the x-direction only. The vertical velocity v_z results from integrating the prescribed vertical strain rate D_{zz}, which gives a linear/quadratic profile (e.g. Greve and others, 2002).

For the ODF, we use the preliminary data of the EDML fabric described above.

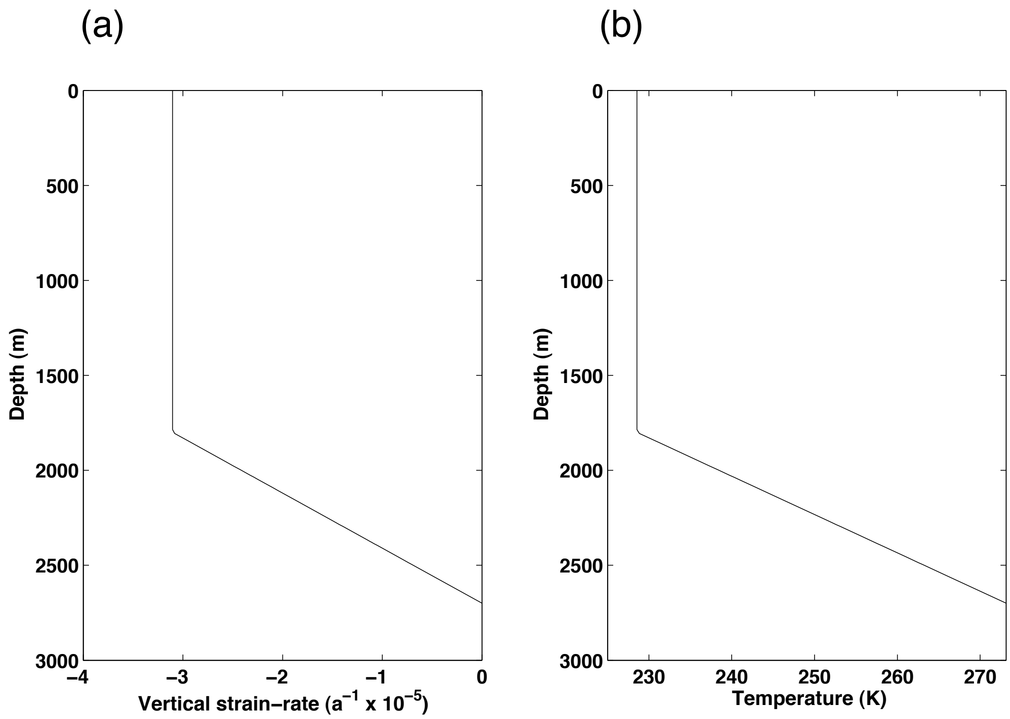

Figure 4.3: Dansgaard-Johnsen type distributions of (a) the vertical strain rate and (b) the temperature at the EDML site. The depth of the kinks is at two-thirds of the local ice thickness. The strain rate at the surface has been chosen such that the downward vertical velocity equals the accumulation rate, and the surface and basal temperatures match the ice-core data.

However, since during the drilling process the orientation of the core is not fixed, the horizontal orientation of the non-circularly symmetric girdle fabric (between approximately 600 and 2040 m depth) relative to our coordinate system, i.e., the direction of ice flow, is unknown. For this reason, we need to assign an orientation for the fabric when computing the enhancement factor. We consider two limiting cases by rotating the initial data such that the girdle fabric at all depths is aligned with the x-axis (case "R13") and with the y-axis (case "R23"), respectively. This is illustrated in Fig. 4.4. At the surface, we assume isotropic conditions, so that $\mathcal{A}_\mathrm{s} = 1$, and for the maximum softening and hardening parameters, we use the values $E_\mathrm{max} = 10$ and $E_\mathrm{min} = 0$, respectively.

In a second step, we attempt at solving the fabric evolution equation (3.16). For the lack of better knowledge, we neglect recrystallization, that is, we set $\lambda = 0$ and $\Gamma = 0$ in the constitutive relations (3.19) and (3.22), respectively. By allowing only a dependency of the orientation mass density $\rho^\star$ on the vertical coordinate z (one-dimensional steady-state problem) and on the orientation $\mathbf{n}$, the orientation mass balance (3.16) yields an

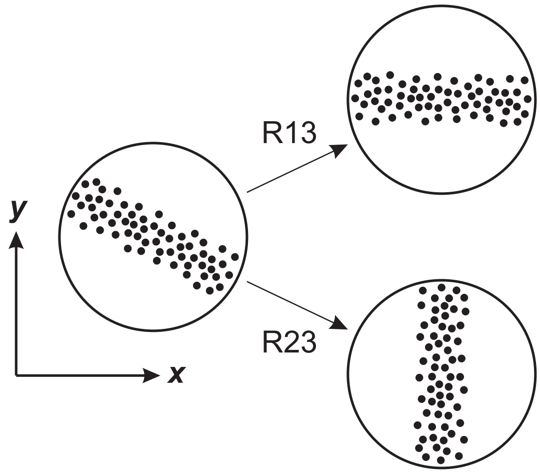

Figure 4.4: Sketch of the rotation of the girdle fabrics in order to align with the x-axis (case "R13") and with the y-axis (case "R23") in the Schmidt projection.

equation which governs the fabric evolution along the EDML ice core,

$$\frac{\partial \rho^\star}{\partial z} v_z + \partial_i(\rho^\star u_i^\star) = 0, \tag{4.6}$$

where the orientational gradient operator ∂_i and the orientation transition rate $u_i^\star$, respectively, read in index notation as

$$\partial_i = \frac{\partial}{\partial n_i} - n_i n_j \frac{\partial}{\partial n_j} \tag{4.7}$$

and, due to Eq. (3.18),

$$u_i^\star = \iota D_{hk} n_h n_k n_i - \iota D_{ij} n_j + W_{ij} n_j. \tag{4.8}$$

With Eq. (4.7), and by inserting the constitutive relation Eq. (4.8) in Eq. (4.6), it follows

$$\begin{aligned} \frac{\partial \rho^\star}{\partial z} v_z \quad &+ \quad u_i^\star \partial_i \rho^\star + \rho^\star \partial_i u_i^\star \\ &= \quad \frac{\partial \rho^\star}{\partial z} v_z + (W_{ij} - \iota D_{ij}) n_j \partial_i \rho^\star + 3\iota \rho^\star D_{hk} n_k n_h = 0. \end{aligned} \tag{4.9}$$

We assume that the local flow field consists of vertical compression with the compression rate (negative vertical strain rate) $\varepsilon = -\partial v_z/\partial z$ according to Fig. 4.3, horizontal extension according to Eq. (4.5), and the horizontal, bed-parallel shear rate

$$\gamma = \frac{\partial v_x}{\partial z} = 2\rho g \frac{\partial h}{\partial x}\, \hat{E}(\mathcal{A})\, A(T')\, \sigma^{n-1}\, z \tag{4.10}$$

that results from Eq. (4.4). The velocity gradient $\mathsf{L} = \operatorname{grad}\mathbf{v}$ then reads

$$\mathsf{L} = \begin{pmatrix} a\varepsilon & 0 & \gamma \\ 0 & (1-a)\varepsilon & 0 \\ 0 & 0 & -\varepsilon \end{pmatrix}. \tag{4.11}$$

Consequently, we obtain for the strain-rate tensor D and the spin tensor W

$$\mathsf{D} = \begin{pmatrix} a\varepsilon & 0 & \frac{1}{2}\gamma \\ 0 & (1-a)\varepsilon & 0 \\ \frac{1}{2}\gamma & 0 & -\varepsilon \end{pmatrix} \tag{4.12}$$

and

$$\mathsf{W} = \begin{pmatrix} 0 & 0 & \frac{1}{2}\gamma \\ 0 & 0 & 0 \\ -\frac{1}{2}\gamma & 0 & 0 \end{pmatrix}. \tag{4.13}$$

With these expressions and the introduction of spherical coordinates, Eq. (4.9) reduces to (cf. Appendix A)

$$\begin{aligned} 4\frac{\partial\rho^\star}{\partial z}v_z &+ 3\iota\rho^\star\big\{\varepsilon[2(2a-1)\sin^2\theta\cos 2\varphi - 1 - 3\cos 2\theta] + 2\gamma\sin 2\theta\cos\varphi\big\} \\ &+ 2\frac{\partial\rho^\star}{\partial\varphi}\Big\{\varepsilon\iota(2a-1)\sin 2\varphi + \gamma(-1+\iota)\frac{\sin\varphi}{\tan\theta}\Big\} \\ &+ 2\frac{\partial\rho^\star}{\partial\theta}\Big\{-\frac{1}{2}\iota\varepsilon\sin 2\theta\,[(2a-1)\cos 2\varphi + 3] + \gamma(1-\iota\cos 2\theta)\cos\varphi\Big\} \\ &= 0, \end{aligned} \tag{4.14}$$

where θ and φ are the polar angle (co-latitude) and azimuth angle (longitude), respectively. Note that, due to Eq. (4.10), the shear rate γ depends on the fabric via the deformability $\mathcal{A}$ with the solution of D_t^2 computed in Appendix B.

The shear flow at the EDML station leads to the transport of ice particles over significant horizontal distances. Huybrechts and others (2007) estimate, based on three-dimensional flow modeling, that particles at 89% depth of the core originate from $\approx$ 184 km upstream. This is not taken into account in our spatially one-dimensional model. However, the variation of the shear upstream of the drill site is likely small due to the small variation of the surface gradient (Fig. 4.2), so that the error resulting from the neglected horizontal inhomogeneity should be limited.

We also consider the simplified case of a transversely isotropic (circularly symmetric) fabric, so that the OMD $\rho^\star$ is only a function of the depth z and the polar angle θ. Then

Eq. (4.14) becomes, after integration over the azimuth angle φ,

$$4\frac{\partial \rho^\star}{\partial z} v_z - \frac{\partial \rho^\star}{\partial \theta} 3\iota\varepsilon \sin 2\theta - 3\iota\rho^\star\varepsilon(1 + 3\cos 2\theta) = 0. \tag{4.15}$$

Note that the dependence on the shear rate γ has disappeared, so that the evolution of the transversely isotropic fabric is only driven by the compression rate ε. The equation for the deformability, Eq. (3.14) needs also to be integrated over the azimuth angle φ, so that from Eq. (B.1), the deformability is computed when the fabric is assumed transversely isotropic by

$$\begin{aligned} \mathcal{A} &= \frac{5}{\mathrm{tr}(D^2)} \int_0^\pi \frac{1}{32}\pi(8L_{xz}^2 + 23\epsilon^2 - 20a\epsilon^2 + 20a^2\epsilon^2 \\ &+ 4(L_{xz}^2 - (1-2a)^2\epsilon^2)\cos 2\theta \\ &+ (4L_{xz}^2 + (-19 + 4a - 4a^2)\epsilon^2)\cos 4\theta)\, d\theta. \end{aligned} \tag{4.16}$$

Equations (4.14) and (4.15) are solved using a finite-volume discretization in the three-dimensional (z, θ, φ) configuration space and a finite-difference discretization in the two-dimensional (z, θ) configuration space, respectively (cf. Appendix C). In z-direction, the resolution is refined with depth via $z_{i+1} = z_i + (v_z)_i\,\Delta t$, where $z_0 = 0$ is the surface, $(v_z)_i$ is the vertical velocity at depth z_i, and $\Delta t = 1$ d for Eq. (4.14), $\Delta t = 20$ a for Eq. (4.15). The angular resolution on the unit sphere is $\Delta\theta = \Delta\varphi = 5°$ for Eq. (4.14), and $\Delta\theta = 0.2°$ for Eq. (4.15). In agreement with the considerations at the end of Sect. 3.5.2, the parameter ι is set to the value 0.6.

4.4 Results and discussion

4.4.1 Anisotropic ice flow with prescribed fabric

Figure 4.5 shows the variation of the enhancement factor, the ice fluidity and the horizontal velocity along the ice core, computed with the ODF based on the fabric data described in Sect. 4.2. The parameter in Eq. (4.5) has been set to $a = 1$ (horizontal extension in x-direction only). This choice is supported by the observed non-circularly symmetric girdle fabric, which cannot form under isotropic horizontal extension. For both limiting cases R13 and R23, the enhancement factor is close to unity in the upper 600 m, which reflects the nearly isotropic fabrics in that part of the EDML core. Further down, in the girdle fabric regime, the case R13 is characterized by a moderate increase of the enhancement factor to an average value of about two, whereas the case R23 exhibits a strong decrease of the enhancement factor to values close to zero. This demonstrates clearly that the girdle fabrics produce a significantly different mechanical response depending on the orientation relative to the ice flow. Case R23 is probably closer to reality, because in the girdle fabric regime above 2000 m depth the deformation is essentially pure shear (vertical compression, horizontal extension in x-direction). For this situation, a simple "deck-of-cards" model illustrates that the c-axes turn away from the x-axis and towards the z-axis, whereas nothing happens in y-direction, so that in the Schmidt projection a concentration perpendicular to the x-axis (flow direction) results.

Below 2000 m depth, where the fabric switches to a single maximum, the difference between the cases R13 and R23 essentially vanishes. The crystal basal planes are favorably oriented for the now prevailing simple-shear deformation, which leads to large deformabilities. Consequently, the enhancement factor shows a sharp increase to a maximum value of about eight, which is close to the theoretical maximum of $E_{\text{max}} = 10$.

The variabilities of the enhancement factor and the effective stress, as well as the increase of the temperature with depth, contribute to the fluidity profiles shown in Fig. 4.5b. Since the fluidity is very small above 2000 m depth and increases only further down, the difference between the cases R13 and R23 in absolute values is surprisingly small. At 2563 m depth, the fluidity is about 200 times higher than the fluidity at 1000 m depth for the case R23 due to the counteracting contributions from the favorably oriented c-axes, the higher temperature and the smaller effective stress. The latter is somewhat surprising; it is caused by the normal deviatoric stresses S_{xx} and S_{zz}, which decrease strongly below 2000 m depth and outweigh the influence of the increasing shear stress S_{xz} in the effective stress.

Owing to the large enhancement factors close to the bottom, the anisotropic flow law predicts significantly larger horizontal velocities compared to the isotropic flow law for the entire depth of the ice core (Fig. 4.5c). At the surface, the anisotropic horizontal velocities are by approximately a factor 3.5 larger than their isotropic counterparts, and the absolute value of $\approx 0.7\,\text{m}\,\text{a}^{-1}$ agrees very well with measurements [H. Oerter, pers. comm. 2005; Wesche and others (2007)]. The difference between the cases R13 and R23 amounts to $\approx 10\%$, the larger values being obtained for the case R23 owing to the slightly larger enhancement factors below 2000 m depth. Interestingly, these differences show that the fabrics are not perfectly transversely isotropic below 2000 m depth, even though they are very close to the single-maximum type.

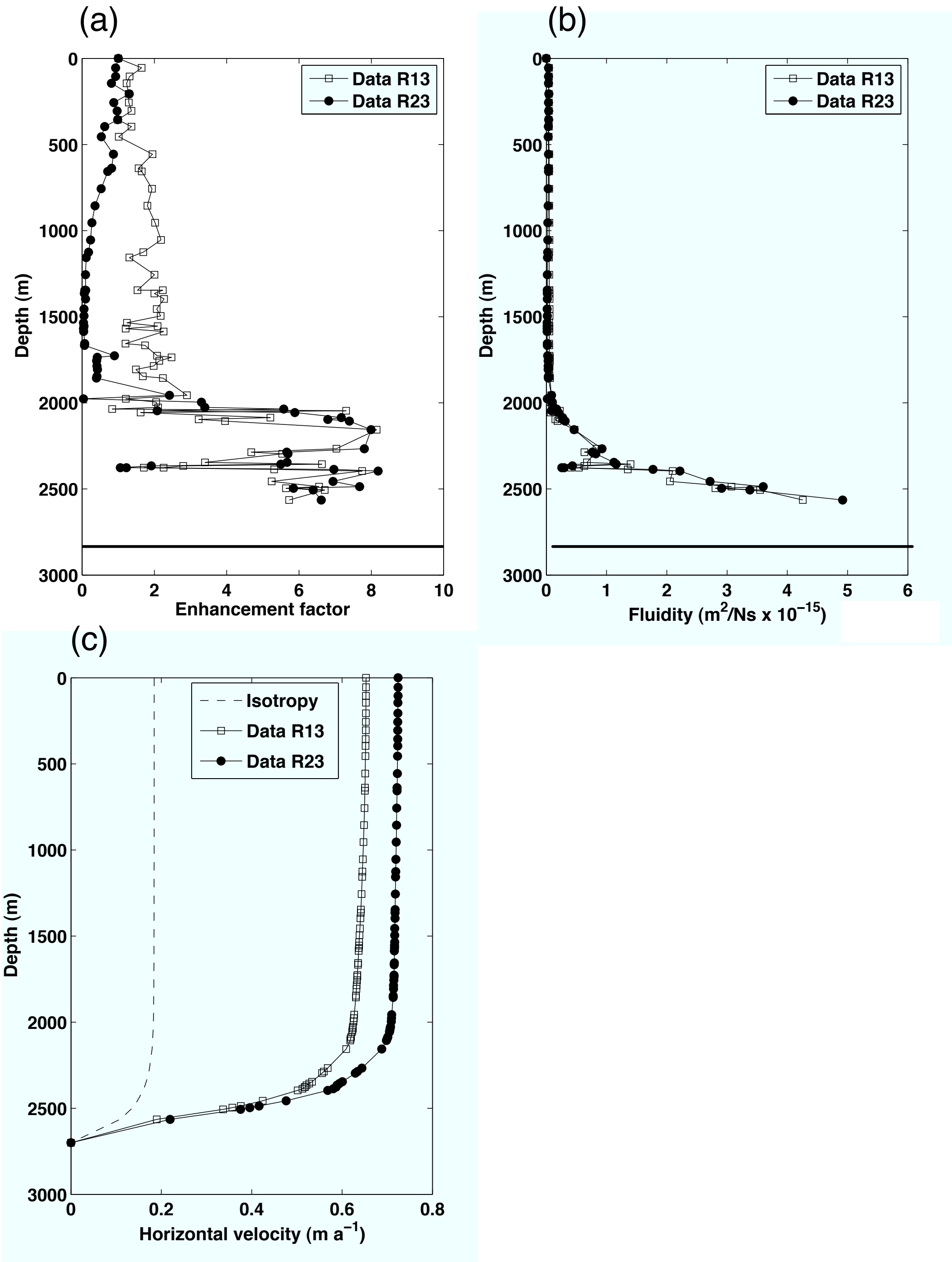

Figure 4.5: Variation along the EDML ice core of (a) the enhancement factor, (b) the ice fluidity and (c) the horizontal velocity. “Data R13” and “Data R23” represent the solutions obtained with the measured girdle fabrics rotated to align with the x- and y-direction, respectively, and “Isotropy” represents isotropic conditions.

4.4.2 Fabric evolution with transverse isotropy

Let us now turn to the simulation in which the fabric evolution is computed by solving Eq. (4.15) for a transversely isotropic fabric. Although this assumption is not consistent with the observed girdle fabric between approximately 600 and 2000 m depth and is therefore a gross simplification, it is interesting to study the mechanical response of such a simplified system and the differences to the ice flow resulting from applying the measured fabrics.

Figure 4.6a shows the comparison between the enhancement factors resulting from the computed, transversely isotropic fabric (which will be referred to as “modeled enhancement factor” in the following) and from the fabric data. Evidently, the agreement is good despite the assumption of transverse isotropy. Down to 1800 m depth, the modeled enhancement factor lies in between the cases R13 and R23, which are the limiting cases for the orientation of the measured girdle fabric with respect to the ice-flow direction. Between 1800 and 1900 m depth, the modeled enhancement factor is very close to the low values of the case R23, for which the girdle fabric is aligned perpendicular to the flow direction. Below 2000 m depth, the sharp increase is also well reproduced; however, the maximum of the modeled enhancement factor is more pronounced and lies closer to the bottom than for the cases R13 and R23.

For that reason, the modeled enhancement factor leads to larger near-basal shear rates than the enhancement factor based on the cases R13 and R23. Consequently, the horizontal velocity resulting from the modeled enhancement factor is larger by about a factor two than the velocities for the cases R13 and R23 (Fig. 4.6b). At the surface, a value of $\approx 1.5\,\mathrm{m\,a^{-1}}$ is reached, which is twice the measured surface velocity. This highlights the great sensitivity of the ice dynamics to the processes near the bottom, which are most difficult to model precisely. Beside the assumption of transverse isotropy, a weak point in that context is the disregard of recrystallization processes, which is expected to become important for the fabric evolution in the lower part of the ice core.

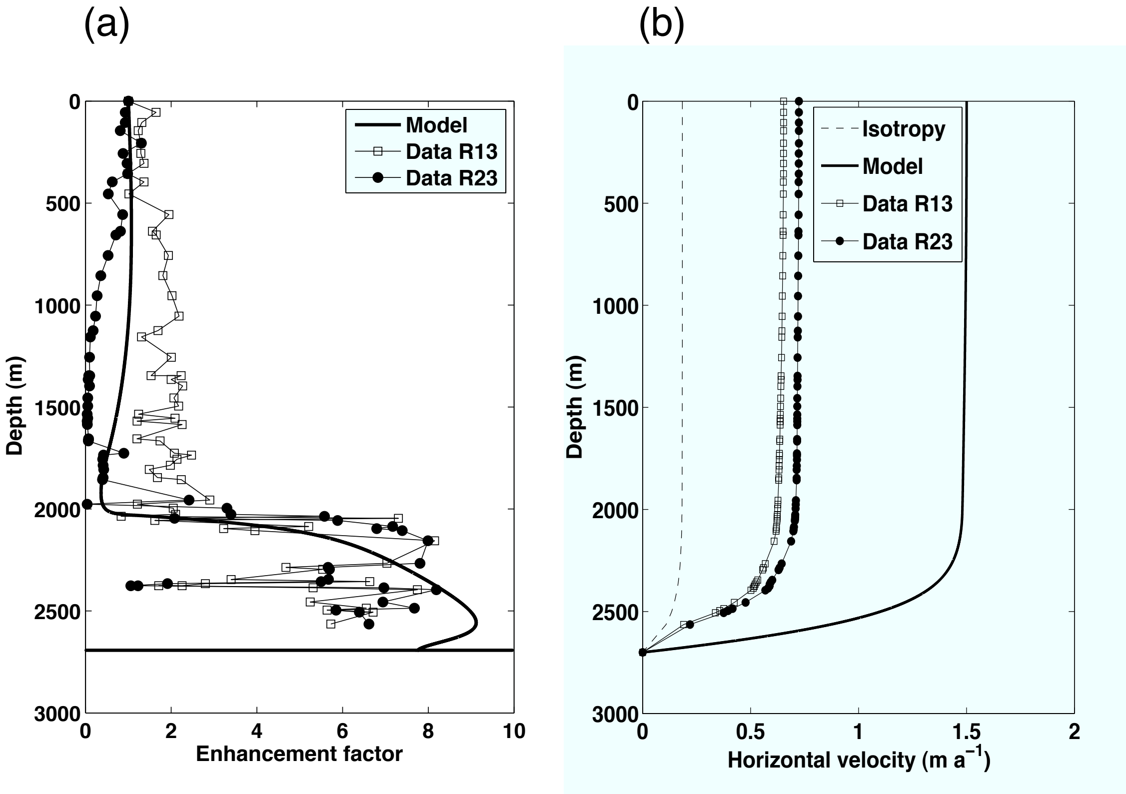

Figure 4.6: Variation along the EDML ice core of (a) the enhancement factor and (b) the horizontal velocity. “Model” represents the solutions based on the fabric evolution equation (4.15) for transverse isotropy. For “Data R13”, “Data R23” and “Isotropy” see the caption of Fig. 4.5.

4.4.3 Unrestricted fabric evolution

We now drop the assumption of transverse isotropy and compute the fabric evolution for the EDML site by solving the full equation (4.14), which describes the general one-dimensional, steady-state problem in the coordinates z, θ and φ without further approximations. The parameter in Eq. (4.5) has again been set to $a = 1$ (horizontal extension in x-direction only).

The resulting Schmidt diagrams for the ODF are presented in Fig. 4.7. For the sake of easy comparison with the fabric data, the depths are the same as in Fig. 4.1. We see a very good agreement between the data and the model results for the transition with depth from an isotropic fabric via broad and narrow girdle fabrics to a single maximum at about 2040 m. The computed girdle fabrics are aligned with the y-axis (perpendicular to the flow direction), which confirms our above justification that the case R23 for the orientation of the measured fabrics is more realistic (Sect. 4.4.1). Note also that for the alternative choice $a = 1/2$ (isotropic horizontal extension) no girdle fabric can form (results not shown). At the depths of 2035 m and 2045 m, the obtained single maximum fabrics have a noticeable deviation from the vertical (center of the Schmidt diagrams). This is also in agreement with the data, and is an effect of the transition of the deformation regime from mainly pure shear to mainly bed-parallel simple shear. However, at 2563 m depth, the modeled fabric shows a widened and somewhat decayed structure, which is reflected in the data only to a limited extent.

Down to approximately 2100 m depth, the profile of the enhancement factor obtained from the computed fabrics (Fig. 4.8a) agrees well with the results obtained from the R23 data. In the girdle fabric regime between 600 and 2000 m depth, the values are therefore distinctly lower than those based on transverse isotropy, which lie rather between the R13 and R23 data (Fig. 4.6a). The sharp increase of the enhancement factor between 2000 and 2100 m depth emerges in a very similar fashion for both the cases of transverse isotropy and general anisotropy.
However, below 2100 m depth, the enhancement factor for general anisotropy becomes radically different from that for transverse isotropy. Starting from the maximum value of about five, it drops to almost unity, and increases further down to values slightly larger than two; the latter corresponding to the Schmidt diagram for 2563 m depth in Fig. 4.7. The trends of both the R13 and R23 data show a similar behavior, but the absolute values of the enhancement factor are clearly underpredicted by the solution of the fabric evolution equation (4.14) because of the resulting decay of the single maximum. This becomes evident more clearly by inspection of the second-order orientation tensor $\mathsf{a}^{(2)}$ of the calculated fabric (Fig. 4.8b). The development of an ideal, vertical single-maximum fabric would result in values of $a^{(2)}_{33}$ converging to one and values of $a^{(2)}_{11}$ and $a^{(2)}_{22}$ to zero.

While the trend towards this state lasts until 2100 m depth, $a_{33}^{(2)}$ decreases between 2100 and 2300 m depth. Further down, $a_{33}^{(2)}$ increases again and finally stabilizes at around 0.7 close to the core bottom. So the model predicts the formation of a fabric with a smaller concentration of c-axes around the vertical direction than the measured fabric.

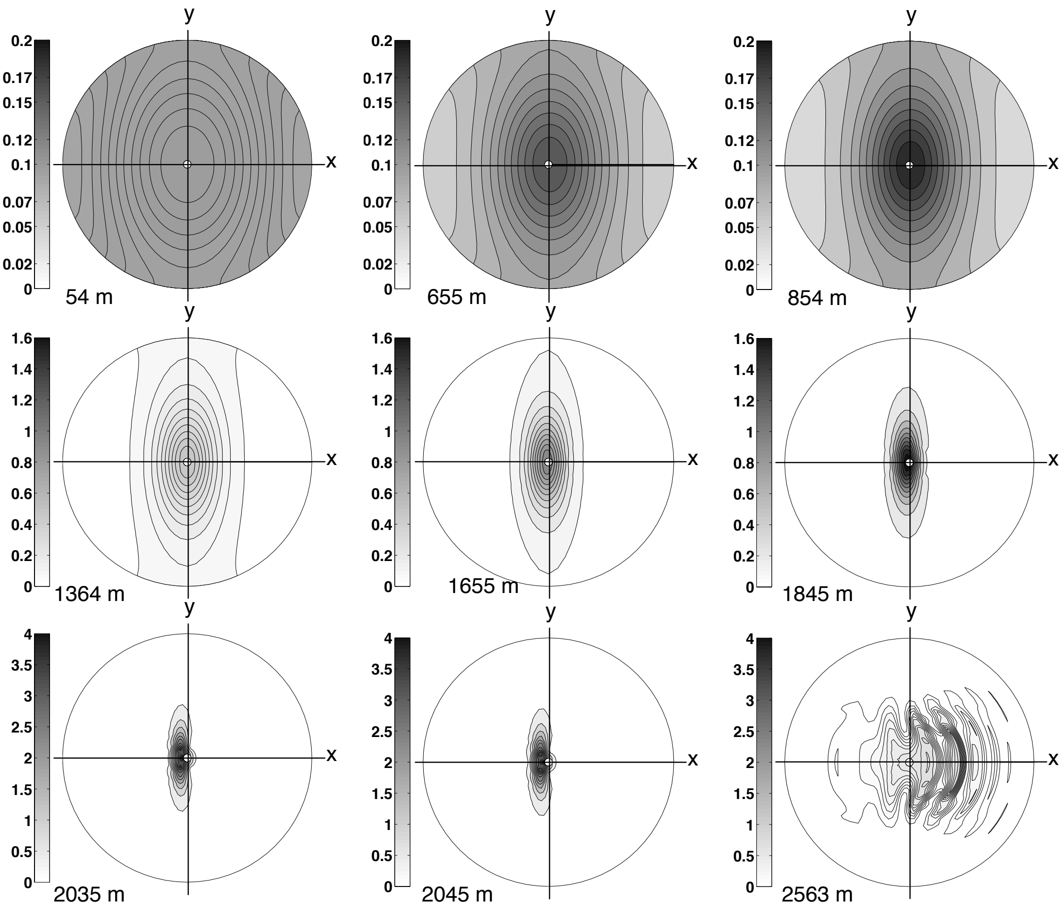

Figure 4.7: Schmidt diagram representation of the EDML fabrics (ODF) at depths between 54 m and 2563 m computed by Eq. (4.14). Like in Fig. 4.1, the centers of the diagrams coincide with the core axis, and the projection is done on the horizontal (x-y) plane.

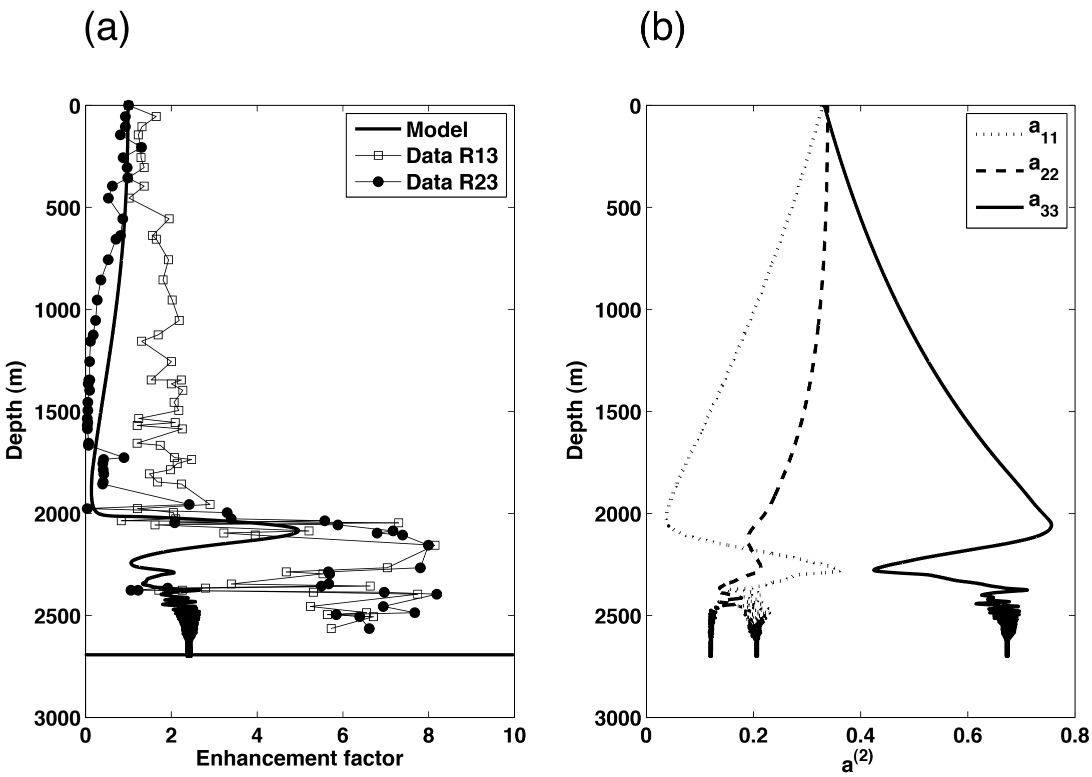

Figure 4.8: Variation along the EDML ice core of (a) the enhancement factor and (b) the three non-zero components of the second-order orientation tensor $\mathsf{a}^{(2)}$. "Model" represents the solutions based on the fabric evolution equation (4.14). For "Data R13" and "Data R23" see the caption of Fig. 4.5. Panel (b) shows only the "Model" solutions.

If the shear rate γ in Eq. (4.14) is ignored, a strong single maximum fabric forms in the near-basal parts of the core, and the enhancement factor becomes similar to that obtained under the assumption of transverse isotropy (see above, Sect. 4.4.2) as depicted in Figures 4.9 and 4.10. For the latter case, note that the shear rate does not appear at all in Eq. (4.15), which is a direct consequence of averaging over the azimuth angle. The decay of the single maximum fabric (decreasing values of $a_{33}^{(2)}$) is therefore due to the dominance of bed-parallel simple shear in the bottommost 100's of meters. Inspection of the constitutive relation (3.18) for the orientation transition rate shows that, under simple shear and for $\iota < 1$, the local rigid-body rotation always outweighs the deformational contribution, so that $\mathbf{u}^\star = \mathbf{0}$ is not possible for any orientation $\mathbf{n}$, and a stable single maximum fabric cannot form by grain rotation only. However, as already stated at the end of Sect. 4.4.2, neglecting recrystallization processes is critical in this part of the core, and it is therefore not surprising that the model results deviate from the data. In particular, migration recrystallization will drive the fabric back towards a vertical single maximum which is most favorable for bed-parallel simple-shear deformations. Therefore, the discrepancy between modeled and observed fabrics below 2100 m depth, and the resulting discrepancy of the enhancement factors, becomes qualitatively understandable.

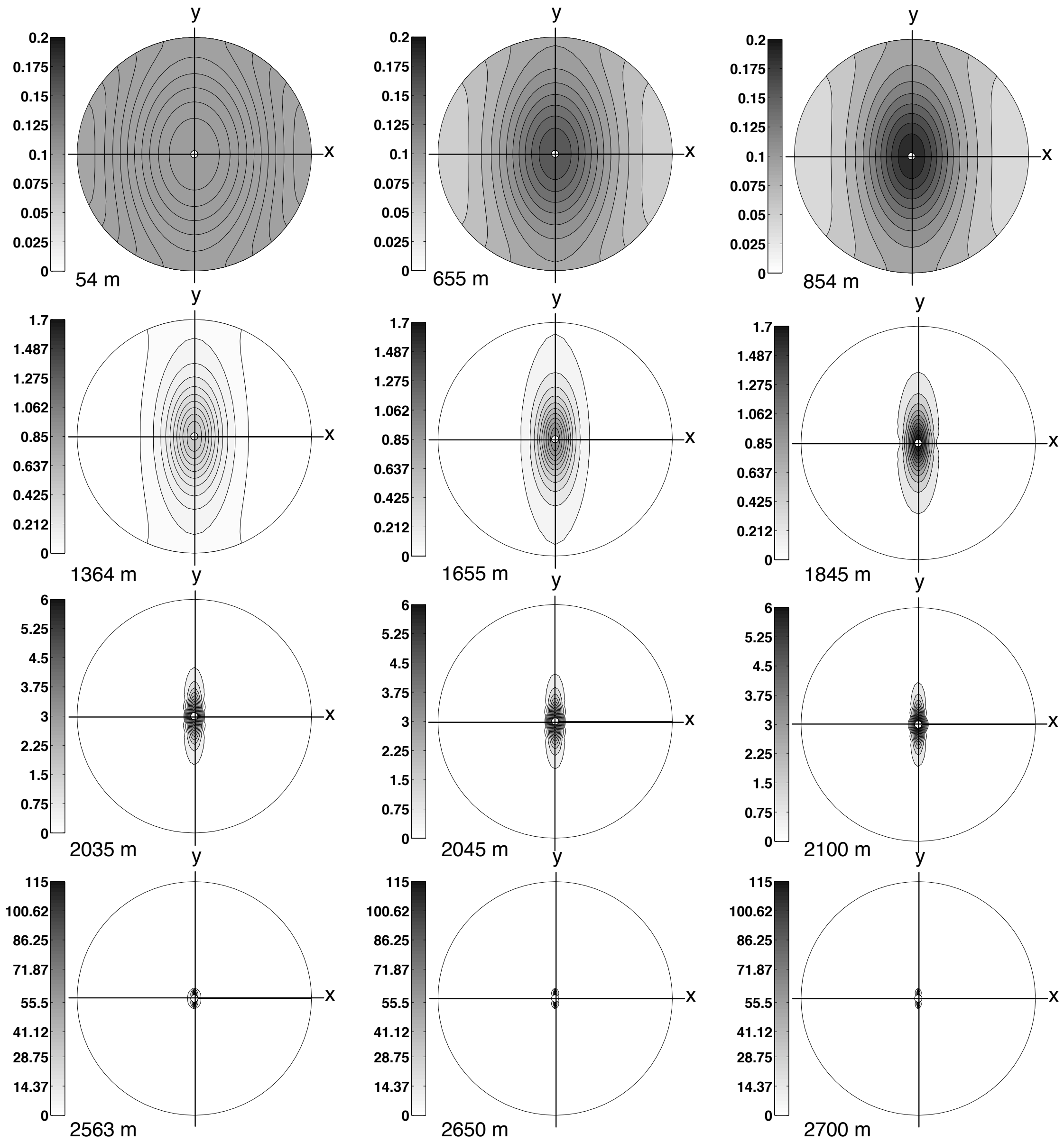

Figure 4.9: Schmidt diagram representation of the EDML fabrics (ODF) at depths between 54 m and 2700 m computed by Eq. (4.14) with $\gamma = 0$. Like in Fig. 4.1, the centers of the diagrams coincide with the core axis, and the projection is done on the horizontal (x-y) plane.

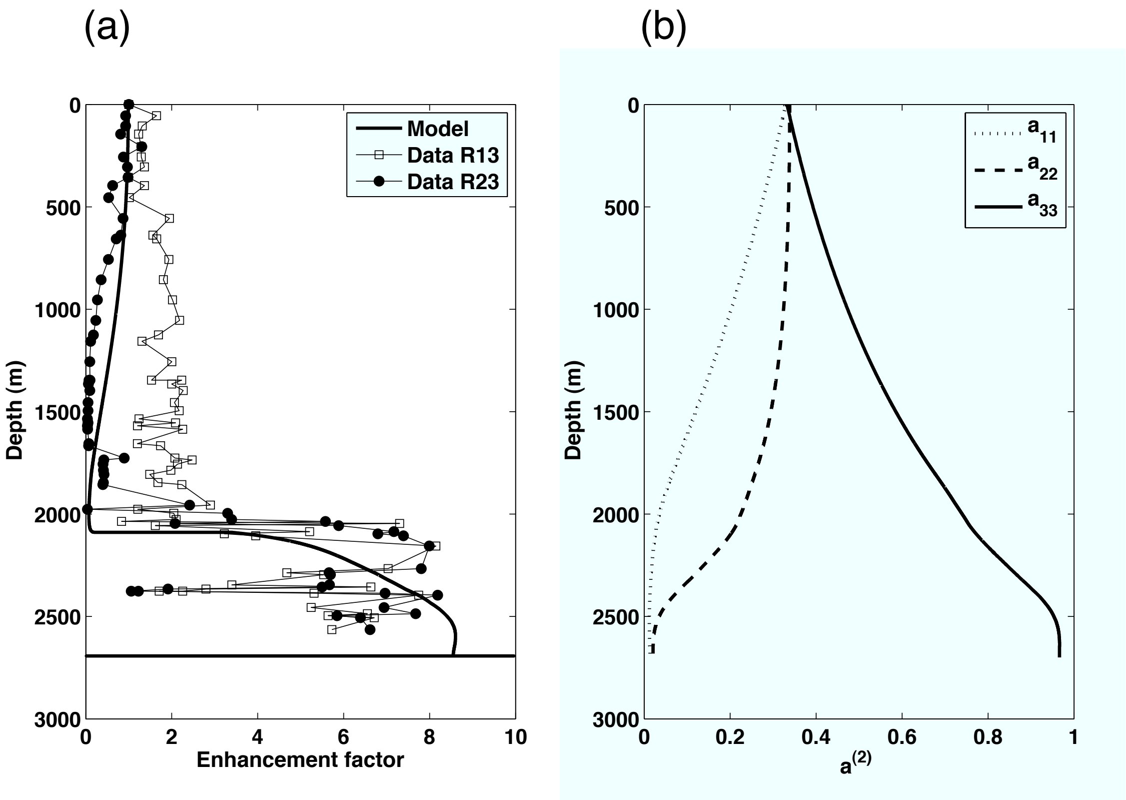

Figure 4.10: Variation along the EDML ice core of (a) the enhancement factor and (b) the three non-zero components of the second-order orientation tensor $\mathsf{a}^{(2)}$. "Model" represents the solutions based on the fabric evolution equation (4.14) with $\gamma = 0$. For "Data R13" and "Data R23" see the caption of Fig. 4.5. Panel (b) shows only the "Model" solutions.

4.5 Lagrangian solution for the fabric evolution equation

In order to assess the dependence of the results on the numerical technique used in this work for the solution of Eq. (4.14) [see Sect. 4.3, last paragraph], we have also applied a Lagrangian approach that computes the evolution of the c-axis orientation for discrete grains, contrary to the finite volume method in the Eulerian frame (Appendix D). For this simulation, we have used 4900 discrete grains to describe the fabric, with isotropic fabric at the surface. Fig. 4.11 shows the evolution of the fabric computed with this model for the first 1845 m depth. We observe, similarly to the finite volume method, the transition from an isotropic fabric to the girdle fabric.

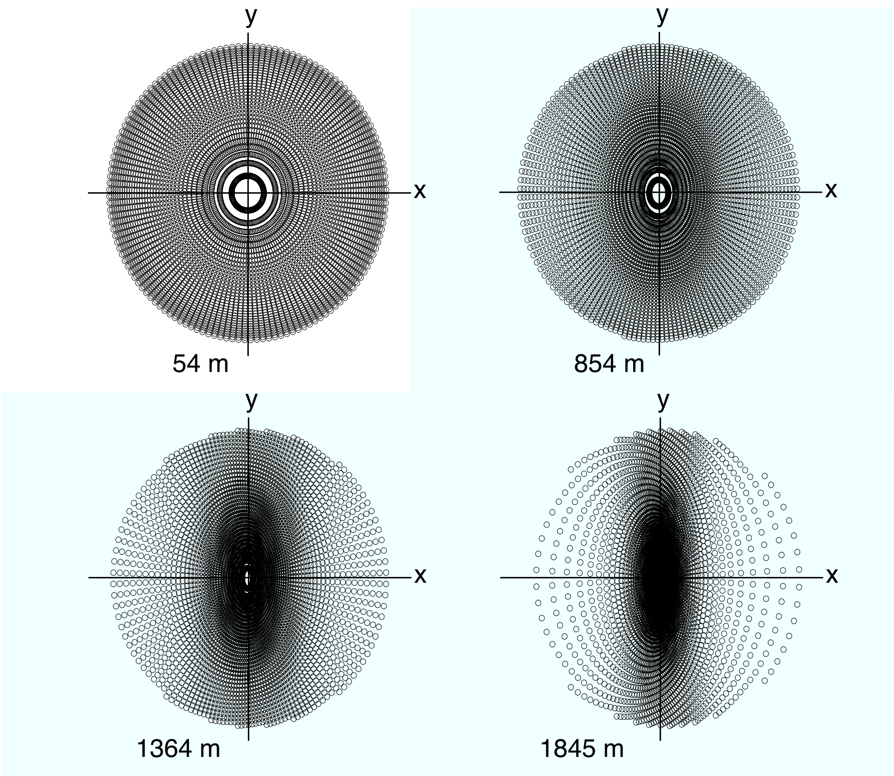

Figure 4.11: Schmidt diagram representation of the EDML fabrics at depth between 54 m and 1845 m computed by the Lagrangian model with each grain represented by a circle in the diagram. Like in Fig. 4.1, the centers of the diagrams coincide with the core axis, and the projection is done on the horizontal (x-y) plane.

Below 2200 m depth (Fig. 4.12), the concentration of the fabric at 2035 and 2045 m is somewhat less important in comparison to the finite volume method. However the deviation from the vertical is also reproduced and it is more pronounced as the decay of the single maximum occurs due to the shearing (2200 m). Therefore, this model provides similar results, and in particular the same trend of the c-axes to rotate away from the vertical direction beyond 2100 m depth. The results presented in Section 4.4.3 are therefore numerically robust and the solution of the fabric evolution equation does not depend on the numerical method.

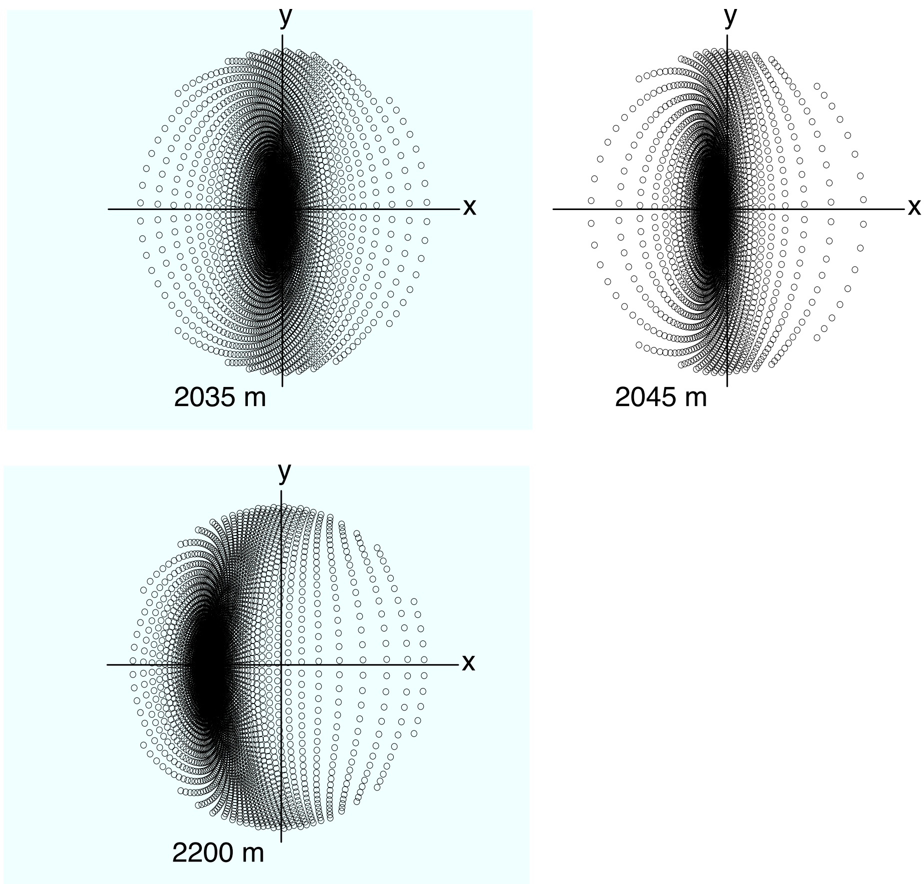

Figure 4.12: Schmidt diagram representation of the EDML fabrics at depth between 2035 m and 2200 m computed by the Lagrangian model with each grain represented by a circle in the diagram. Like in Fig. 4.1, the centers of the diagrams coincide with the core axis, and the projection is done on the horizontal (x-y) plane.

4.6 Stability analysis of the anisotropic flow law

In the previous section, we have verified that the numerical method used in the model is robust enough and that the model results do not depend on the numerical method employed for solving the equations. In order to validate our flow law and the results exposed in this section, we lastly need to verify the stability of the anisotropic flow law itself. For that purpose, we need to verify the stability of the flow law when the fabric is gradually evolving to a vertical single maximum configuration. The method used here, consists on the analysis of the equipotentials defined on the space of the stresses S_{13}-S_{33} (Appendix E). The flow low is stable when for a given stress S_{13}, there is only one corresponding solution for S_{33}. In such case, the equipotential generally depicts a perfect ellipse and it is convex. On the other hand, equipotentials which depict strong concavity can be interpreted as the possible existence of instabilities in the flow law, because for a given stress S_{13}, several solutions for S_{33} are possible. In the following, we trace the equipotentials at several representative depths by computing the second and fourth-order tensors associated with the flow law (cf. Section 5). We are primarily interested in studying the behavior of the flow law with the evolution of the fabric, so that the value of the rate factor in Eq. (E.7) is set to 1. The equipotentials obtained between 54 m and 1364 m are presented in Fig. 4.13. We observe that the flow law describes a well-defined ellipse, therefore there are no instabilities occurring where the girdle fabric is developed. The flow law produces a stable response.

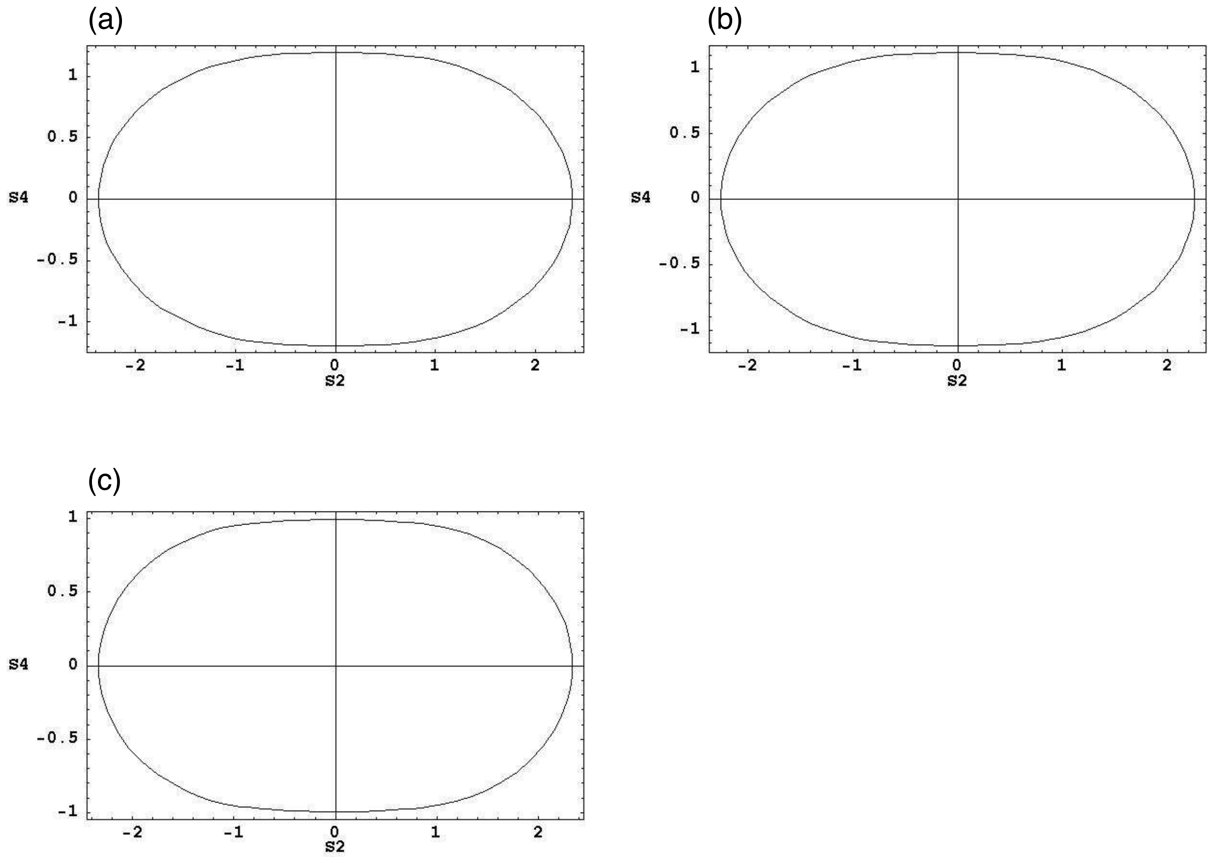

Figure 4.13: Equipotentials obtained at depths 54 m (a), 854 m (b) and 1364 m (c).

Below 1800 m depth (Fig. 4.14), when the fabric develops toward a single vertical maximum configuration, we observe the slight flatness of the equipotentials which corresponds to the development of concave shapes at the poles of the equipotentials. Although, the shape of the equipotentials during the transition towards a single maximum fabric are not perfect ellipse, the stability of the flow law is nevertheless preserved as clearly, a given stress S_{13} corresponds to a single solution for S_{33}.

Deeper in the ice core, when the decay of the fabric occurs, the shape of the equipotentials returns to ellipsoidal (Fig. 4.15). This shows that equipotentials defined by our flow law develop toward somewhat concave shapes when the fabric is evolving to a vertical single maximum, but as noted previously, this concavity does not produce instabilities. We can therefore conclude that the stability flow law is verified for the application to the EDML ice core.

We can lastly assess the behavior of the flow law when the fabric reach a single maximum. This can been done by neglecting the shear rate γ and the obtained fabric is presented in Fig. 4.9. Fig. 4.16 shows the equipotentials obtained for such fabric for the last 300 m depth. At 2400 m depth, we observe that the ellipse tends to narrow from the poles, and that noticeable concavities are developing. At the 2500, 2600 and 2700m depth, the equipotentials do not describe an ellipse anymore, but rather a "bow tie" and the narrowing at the poles is only slightly larger than at 2400 m depth. Even in such case, we can postulate that the flow law is stable. In fact, we can observe that the bow is not pronounced enough to create instabilities where for a given stress S_{13}, several solutions of S_{33} are possible. Or in other words, the flow law is stable as long as the bow is not too tied. Therefore, this results allows us to conclude that our anisotropic flow law is stable when strong concentrated single maximum fabrics are formed.

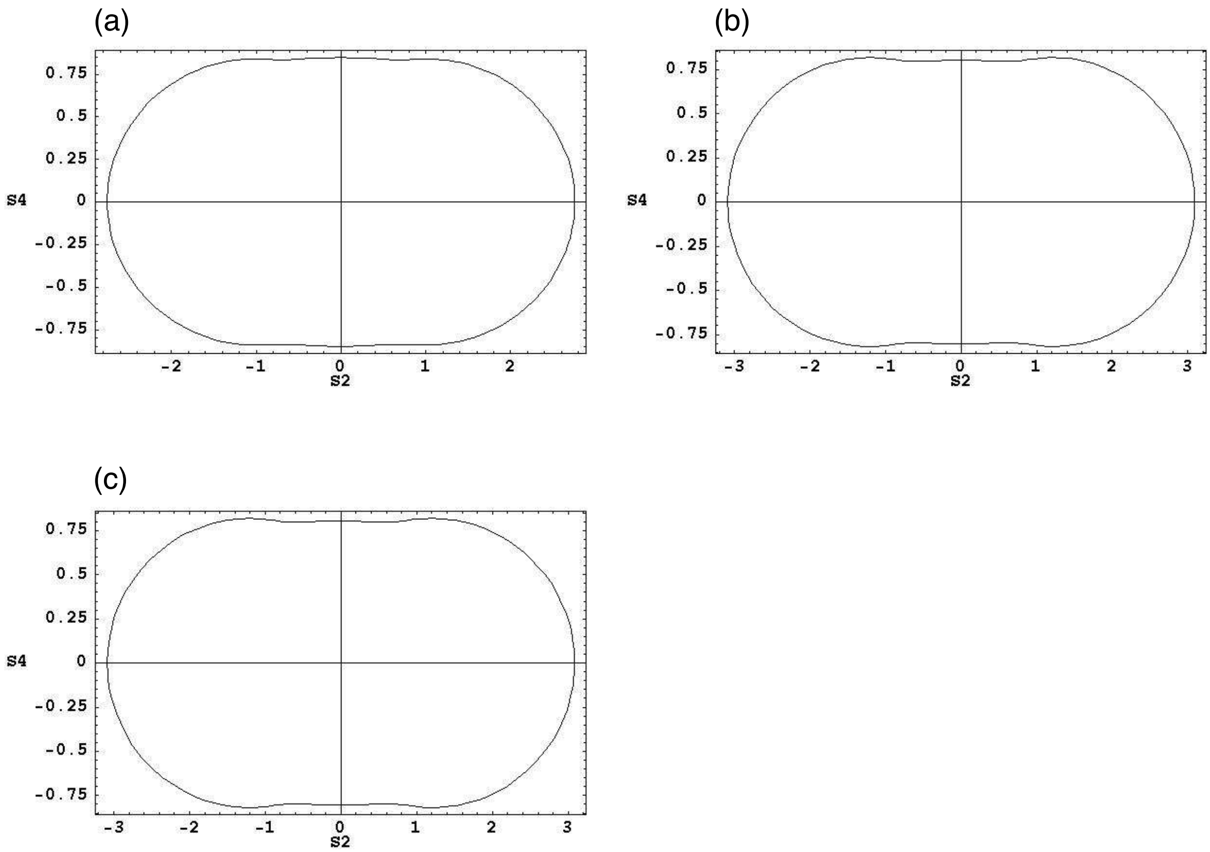

Figure 4.14: Equipotentials obtained at depths 1845 m (a), 2035 m (b) and 2045 m (c).

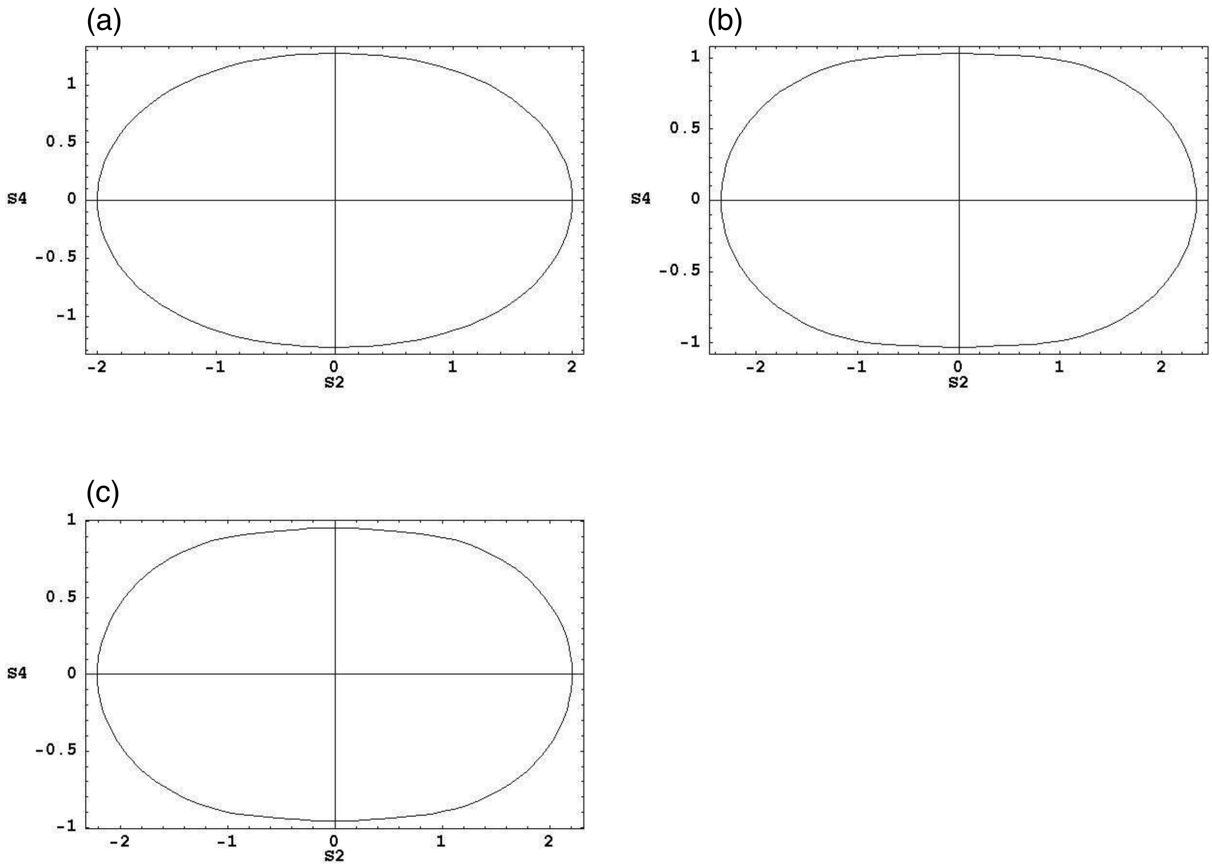

Figure 4.15: Equipotentials obtained at depths 2200 m (a), 2300 m (b) and 2600 m (c).

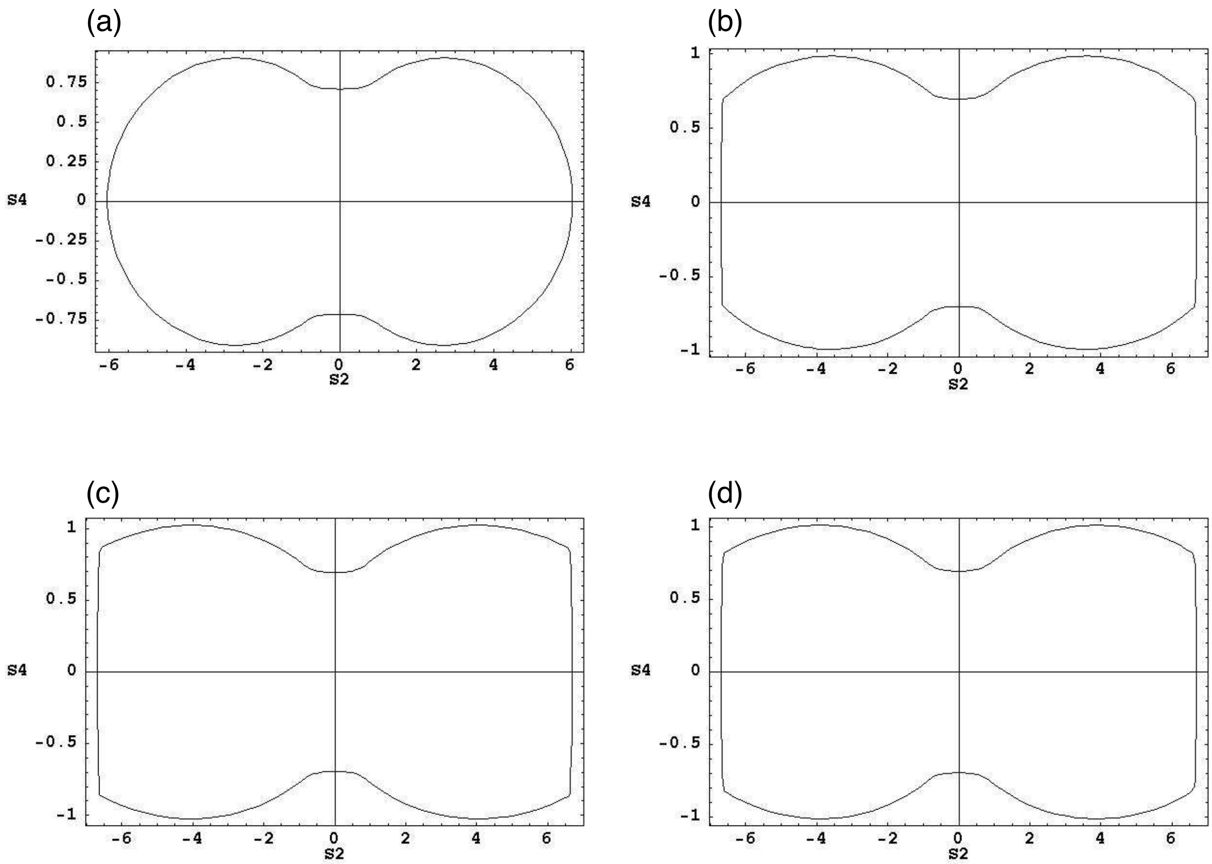

Figure 4.16: Equipotentials obtained at depths 2400 m (a), 2500 m (b), 2600 m (c) and 2700 m (d) with $\gamma = 0$.

4.7 Conclusion

The CAFFE model was successfully applied to the site of the EDML ice core in East Antarctica. Three different methods were employed, (i) computing the anisotropic enhancement factor and the horizontal flow based on fabrics data, (ii) solving the fabric evolution equation under the simplifying assumption of transverse isotropy, and (iii) solving the full fabric evolution equation. Method (i) demonstrated clearly the importance of the anisotropic fabric in the ice column for the flow velocity, and better agreement with the measured surface velocity was achieved compared to an isotropic computation.

The anisotropic enhancement factor produced with method (ii) agreed reasonably well with that of method (i), despite the fact that the measured fabric is not transversely isotropic in large parts of the ice core. For method (iii), which is the most sophisticated one from a modeling point of view, we found that the measured fabric is reproduced well by the model down to approximately 2100 m depth, encompassing the change with depth from an isotropic fabric via broad and narrow girdle fabrics to a single maximum fabric. Only further down, in the warm, near-basal part of the ice core, a systematic disagreement emerged, in that the modeled fabric shows a more pronounced decay than the measured one. This is probably due to the disregard of migration recrystallization in the model as we have shown that the results are independent of the employed numerical method and that the stability of the anisotropic flow law is verified.

The following work presented in this study will focus on the implementation of the CAFFE model in the three-dimensional, full-Stokes ice-flow model Elmer/Ice.

Chapter 5

Anisotropic flow law and fabric evolution: the orientation tensor approach

5.1 Introduction

As stated in the general introduction of this dissertation, the goal of the development of the anisotropic flow model is its application to Dome Fuji in the context of paleo-climatic studies. The previous chapters have presented the theoretical background of the anisotropic law and its application to the EDML ice core with an one dimensional model. However, for large scale finite-element modeling which is intended to be carried out for Dome Fuji, we need to formulate the anisotropic flow law and the fabric evolution equations in terms of orientation tensors. This approach will guaranty the feasibility of the simulation regarding the computing time needed for solution. We have chosen the orientation tensors, because they have been largely used in material science to model anisotropy and because such approach has proven to be robust in ice sheets modeling (Gillet-Chaulet and others, 2006). This chapter will presents some theoretical background about orientation tensors and the orientation tensors based mathematical implementation of the flow law and the fabric evolution equations in the finite-element code.

5.2 Orientation tensors

The fabric can be described in tensorial form by the different moments of an Orientation Distribution Function(ODF) $f^*(\mathbf{n})$ which satisfies the normality condition

$$\int_{S^2} f^*(\mathbf{n})\, d^2n = 1,$$

and $f^*(\mathbf{n})$ represents the fraction of the number of crystallites that have orientations directed towards $\mathbf{n}$ within the solid angle d^2n. The relation of $f^*(\mathbf{n})$ with the orientation mass density $\rho^*(\mathbf{n})$ discussed in Chapter 3 can be formulated as

$$f^*(\mathbf{n}) = \frac{\rho^*(\mathbf{n})}{\rho},$$

where ρ is the mass density. We can note the analogy with the inertial product which characterizes the distribution of mass in a sphere: orientation tensors characterize then the distribution of intersections of c-axis with the sphere of orientations. A orientation tensor of order m, denoted $\mathsf{a}^{(\mathsf{m})}$ is defined as

$$\mathsf{a}^{(\mathsf{m})} = \int_{S^2} f^*(\mathbf{n})\ \mathbf{n}^{\otimes m}\, d^2n = \int_{S^2} f^*(\mathbf{n})\ \mathbf{n}\otimes\mathbf{n}\otimes ...\mathbf{n}\, d^2n, \tag{5.1}$$

Orientation tensors are therefore a good tool for comparing continuous fabrics described by the ODF. Because f^* is a centrosymmetric function, by definition odd-ordered orientation tensors are null. The fabric is then represented by an infinite series of even ordered orientation tensors. Advani and Tucker III (1987) have shown for example that for a medium when there are not interactions between grains, the second and fourth-order tensors are sufficient to describe the macroscopic behavior of an assemblage of components with linear orthotropic behavior.

5.3 Second and fourth order orientation tensors

The mathematical proof of using the second and fourth order orientation tensors in this work will be discussed in the next sections, however we will give here their general mathematical definitions and their relation to $f^*(\mathbf{n})$ as well as the motivation of their use in describing ice fabrics. Using Eq. (5.1), the second and fourth order tensors are given by,

$$\begin{aligned} \mathsf{a}^{(2)} &= \int_{S^2} f^* \; \mathbf{n} \otimes \mathbf{n} \, d^2 n \\ \mathsf{a}^{(4)} &= \int_{S^2} f^* \; \mathbf{n} \otimes \mathbf{n} \otimes \mathbf{n} \otimes \mathbf{n} \, d^2 n. \end{aligned} \tag{5.2}$$

This reads in index notation,

$$\begin{aligned} a^{(2)}_{ij} &= \int_{S^2} f^* n_i n_j \, d^2 n \\ a^{(4)}_{ijkl} &= \int_{S^2} f^* n_i n_j n_k n_l \, d^2 n. \end{aligned} \tag{5.3}$$

With their definitions, those tensors are symmetric and we can define their independent components as,

$$a^{(2)}_{\{ij\}} = \{ a^{(2)}_{ij} = a^{(2)}_{ji} \}, \tag{5.4}$$

and

$$\begin{aligned} & a^{(4)}_{\{ijkl\}} = \\ & \quad \{ a^{(4)}_{ijkl} = a^{(4)}_{klij} = a^{(4)}_{jikl} = a^{(4)}_{ijlk} = a^{(4)}_{klji} = a^{(4)}_{lkij} = a^{(4)}_{lkji} = a^{(4)}_{iljk} = a^{(4)}_{ilkj} \\ & \quad = a^{(4)}_{iljk} = a^{(4)}_{ikjl} = a^{(4)}_{iklj} \}. \end{aligned} \tag{5.5}$$

In addition, higher order orientation tensors completely describe lower-order orientation tensors which can be shown using the normalization condition of the orientation distribution function $f^*(\mathbf{n})$ along with Eqs. (5.3) and (5.5) (Advani and Tucker III, 1987)

$$a^{(4)}_{\{ijkk\}} = a^{(2)}_{\{ij\}}, \tag{5.6}$$

with summation over k. However, two fabrics with the same second-order tensor can have two different fourth-order tensors and then a different macroscopic behavior. This observation constitutes the motivation for using the fourth-order orientation tensor in the description of ice fabrics in ice sheet flow modeling because it allows for differencing multiple pattern of evolution of fabrics which the use of the second-order tensor alone does not permit. We illustrate this point with typical values of the second and fourth-order tensors for different fabrics observed in ice sheets:

- For a vertical single maximum fabric (Fig. 5.1a), there is no uncertainties and the fabric can be fully described by the second-order tensor defined as

$$\mathsf{a}^{(2)} = \begin{pmatrix} 0 & 0 & 0 \\ 0 & 0 & 0 \\ 0 & 0 & 1 \end{pmatrix}.$$

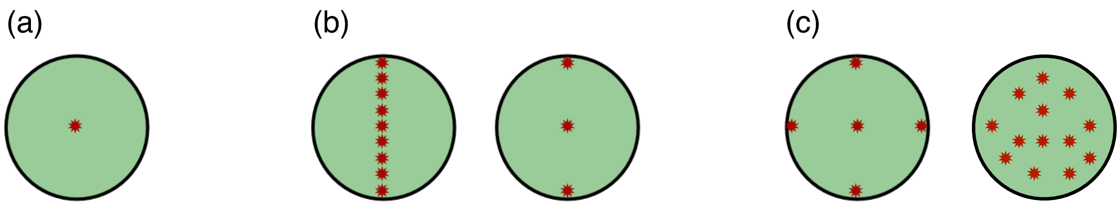

Figure 5.1: Typical fabrics observed in ice sheets: (a) Vertical single maximum fabric. (b) Girdle (left circle) and two maxima fabric (right circle). (c) Three maxima (left circle) and isotropic fabric (right circle)

- The distinction between a girdle fabric (planar isotropic) and a two maxima fabric (Fig. 5.1b) can however not be realized with the second-order tensor which for both fabrics is equal to

$$\mathsf{a}^{(2)} = \begin{pmatrix} 0 & 0 & 0 \\ 0 & 1/2 & 0 \\ 0 & 0 & 1/2 \end{pmatrix}.$$

  The use of the fourth-order tensor can be then justified as it provides a mean of clear distinction between those fabrics as

$$\text{girdle fabric}: a^{(4)}_{1122} = \frac{1}{8}; \quad a^{(4)}_{1111} = a^{(4)}_{2222} = \frac{3}{8}$$

$$\text{two maxima fabric}: a^{(4)}_{1111} = a^{(4)}_{2222} = \frac{1}{2}$$

- Similarly for a three maxima fabric and an isotropic fabric (Fig. 5.1c), the second-order tensor is

$$\mathsf{a}^{(2)} = \begin{pmatrix} 1/3 & 0 & 0 \\ 0 & 1/3 & 0 \\ 0 & 0 & 1/3 \end{pmatrix},$$

whereas the fourth-order tensor gives,

$$\text{three maxima fabric} : a^{(4)}_{1111} = a^{(4)}_{2222} = \frac{1}{3}$$

$$\begin{aligned} \text{isotropic fabric} : a^{(4)}_{1122} &= a^{(4)}_{2233} = a^{(4)}_{1133} = \frac{1}{15} \\ a^{(4)}_{1111} &= a^{(4)}_{2222} = a^{(4)}_{3333} = \frac{1}{5}. \end{aligned}$$

5.4 Formulation of the anisotropic flow law based on orientation tensors

The implementation of the anisotropic flow law presented in this dissertation in a finite-element code requires to formulate a law that is efficient in terms of computing time. If we recall our anisotropic flow law (3.7)

$$\mathsf{D} = \hat{E}(\mathcal{A})\, A(T')\, \sigma^{n-1}\, \mathsf{S},$$

the implementation in a finite-element code requires to reformulate the equation of the deformability $\mathcal{A}$

$$\mathcal{A} = 5 \int\limits_{S^2} \frac{\mathsf{D}\mathbf{n} \cdot \mathsf{D}\mathbf{n} - (\mathsf{D}\mathbf{n} \cdot \mathbf{n})^2}{\mathrm{tr}\,(\mathsf{D}^2)} f^\star(\mathbf{n})\, \mathrm{d}^2 n,$$

so that the computationally intensive integration does not need to be performed in the finite-element procedure. The orientation tensors provides a way to do that. We first write the equation of $\mathcal{A}$ as

$$\mathcal{A} = \frac{5}{\mathrm{tr}\,(\mathsf{D}^2)} \int\limits_{S^2} \mathsf{D}\mathbf{n} \cdot \mathsf{D}\mathbf{n} - (\mathsf{D}\mathbf{n} \cdot \mathbf{n})^2 f^\star(\mathbf{n})\, \mathrm{d}^2 n.$$

In index notations, the above equation reads

$$\mathcal{A} \;=\; \frac{5}{\mathrm{tr}\,(\mathsf{D}^2)} \int_{S^2} f^*[D_{ij}n_jD_{ih}n_h - (D_{ij}n_jn_i)^2]\, d^2n,$$

and

$$\mathcal{A} \;=\; \frac{5}{\mathrm{tr}\,(\mathsf{D}^2)} \left[\int_{S^2} f^* D_{ij}n_jD_{ih}n_h\, d^2n - \int_{S^2} f^*(D_{ij}n_jn_i)^2\, d^2n \right].$$

With Eq. (5.3), we obtain

$$\mathcal{A} \;=\; \frac{5}{\mathrm{tr}\,(\mathsf{D}^2)} [D_{ij}a^{(2)}_{ih}D_{hj} - a^{(4)}_{ijkl}D_{kl}D_{ij}], \tag{5.7}$$

or

$$\mathcal{A} \;=\; \frac{5}{\mathrm{tr}\,(\mathsf{D}^2)} [(\mathsf{D}\cdot\mathsf{a}^{(2)}) : \mathsf{D} - (\mathsf{a}^{(4)} : \mathsf{D}) : \mathsf{D}]. \tag{5.8}$$

Eq. (5.7) and (5.8) have been obtained with the condition of microscopic independent deformation rates. This results shows that our flow law can therefore been mathematically formulated by using orientation tensors, for the case at hand, the flow law depends on the second and fourth-order orientation tensors. Note that Eq. (5.7) can also be expressed with the deviatoric stress tensor S, as its collinearity with the deformation rate tensor D allows writing

$$\mathcal{A} \;=\; \frac{5}{\mathrm{tr}\,(\mathsf{S}^2)} [(\mathsf{S}\cdot\mathsf{a}^{(2)}) : \mathsf{S} - (\mathsf{a}^{(4)} : \mathsf{S}) : \mathsf{S}]. \tag{5.9}$$

Finally, the contracted and double contracted products in Eq. (5.7) are evaluated in Appendix F.

5.5 Formulation of the fabric evolution equation in terms of orientation tensors

5.5.1 Evolution equation of the second-order tensor

We now turn to the fabric evolution equation (3.16) presented in Chapter 3. Similarly to the anisotropic flow law, it needs to be implemented in the finite-element code for the perspective of large scale modeling applied to Dome Fuji which accounts for fabric evolution. The numerical difficulties of using the formulation in Eq. (3.16) arise from the fact that such procedure would require to discretize the unit sphere similar to what has been done for the EDML model (Chapter 4). This approach is unfortunately unfeasible for a large scale finite-element model because of the resulting number of degrees of freedom in the finite-element formulation. Consequently, the approach for modeling the fabric evolution based on the orientation mass density in Eq. (3.16) is replaced with a formulation based on orientation tensors. The fabric evolution is then treated as the evolution of the second-order orientation tensor $\mathsf{a}^{(2)}$. Therefore, the differentiation of Eq. $(5.2)_1$ with respect to the orientation $\mathbf{n}$ gives

$$\dot{\mathsf{a}}^{(2)} = \int_{S^2} f^* \dot{\mathbf{n}} \otimes \mathbf{n}\, d^2n + \int_{S^2} f^* \mathbf{n} \otimes \dot{\mathbf{n}}\, d^2n. \tag{5.10}$$

By inserting the relation in Eq. (3.18) for the orientation transition rate that accounts for the deformation induced grain rotation, Eq. (5.10) reads,

$$\begin{aligned}\dot{\mathsf{a}}^{(2)} = &\int_{S^2} f^* [\mathsf{W}\mathbf{n} + \iota[(\mathsf{D}\mathbf{n}\cdot\mathbf{n})\mathbf{n} - \mathsf{D}\mathbf{n}]] \otimes \mathbf{n}\, d^2n + \\ &\int_{S^2} f^* \mathbf{n} \otimes [\mathsf{W}\mathbf{n} + \iota[(\mathsf{D}\mathbf{n}\cdot\mathbf{n})\mathbf{n} - \mathsf{D}\mathbf{n}]]\, d^2n,\end{aligned} \tag{5.11}$$

and

$$\begin{aligned}\dot{\mathsf{a}}^{(2)} = &\left[\int_{S^2} f^* \mathsf{W}\mathbf{n} \otimes \mathbf{n} + f^*\iota(\mathsf{D}\mathbf{n}\cdot\mathbf{n})\mathbf{n}\otimes\mathbf{n} - f^*\iota D\mathbf{n}\otimes\mathbf{n}\, d^2n\right] + \\ &\left[\int_{S^2} f^* \mathbf{n} \otimes \mathsf{W}\mathbf{n} + f^*\iota\mathbf{n}\otimes(\mathsf{D}\mathbf{n}\cdot\mathbf{n})\mathbf{n} - f^*\iota\mathbf{n}\otimes D\mathbf{n}\, d^2n\right].\end{aligned} \tag{5.12}$$

With mathematical manipulations and by using Eq. $(5.2)_2$, we obtain the evolution equation of the second-order tensor

$$\dot{\mathsf{a}}^{(2)} = \mathsf{W}\cdot\mathsf{a}^{(2)} - \mathsf{a}^{(2)}\cdot\mathsf{W} - \iota[(\mathsf{D}\cdot\mathsf{a}^{(2)} + \mathsf{a}^{(2)}\cdot\mathsf{D}) - 2\mathsf{a}^{(4)} : \mathsf{D}], \tag{5.13}$$

or in Eulerian form

$$\begin{aligned}\frac{\partial \mathsf{a}^{(2)}}{\partial t} + \mathbf{v}\cdot\nabla\mathsf{a}^{(2)} &= \mathsf{W}\cdot\mathsf{a}^{(2)} - \mathsf{a}^{(2)}\cdot\mathsf{W} \\ &- \iota[(\mathsf{D}\cdot\mathsf{a}^{(2)} + \mathsf{a}^{(2)}\cdot\mathsf{D}) - 2\mathsf{a}^{(4)} : \mathsf{D}].\end{aligned} \tag{5.14}$$

Eq. (5.14) is solved for $a_{11}^{(2)}$, $a_{22}^{(2)}$, $a_{12}^{(2)}$, $a_{23}^{(2)}$ and $a_{13}^{(2)}$ (Appendix G).

5.5.2 Closure approximation

The difficulty to obtain a solution for Eqs. (5.8) and (5.14) arises from computing the elements of the fourth-order tensor because the evolution equation of any even-ordered orientation tensor requires the next higher even-ordered orientation tensor. To avoid solving higher-order tensor evolution equations, closure approximations are introduced to represent a higher-order tensor in terms of lowered-ordered tensors. A fourth-order closure may be written as

$$a^{(4)}_{ijkl} \approx F_{ijkl}(a^{(2)}_{mn}), \tag{5.15}$$

where F_{ijkl} is a function of the second-order tensor $a^{(2)}_{ij}$. There exist many closures for the fourth-order orientation tensor $a^{(4)}_{ijkl}$ as a function of $a^{(2)}_{ij}$ [Hand (1962), Doi (1981), Advani and Tucker III (1987), Lipscomb and others (1988), Cintra and Tucker (1995), Dupret and others (1997), Chung and Kwon (2002), Han and Im (2002), etc.]. For the purpose of this work and following Gillet-Chaulet and others (2006), we choose to adopt the invariant-based optimal fitting closure approximation (IBOF) proposed by Chung and Kwon (2002) because of its physical accuracy and numerical stability in comparisons to previous proposed functions.

The IBOF begins with the most general expression of a full symmetric fourth-order tensor $a^{(4)}_{ijkl}$ in terms of $a^{(2)}_{ij}$ and the Kronecker δ_{ij}, which can be derived using the Cayley-Hamilton theorem:

$$\begin{aligned} \mathsf{a}^{(4)} &= \beta_1 S(\mathsf{I}\otimes\mathsf{I}) + \beta_2 S(\mathsf{I}\otimes\mathsf{a}^{(2)}) + \beta_3 S(\mathsf{a}^{(2)}\otimes\mathsf{a}^{(2)}) + \beta_4 S(\mathsf{I}\otimes\mathsf{a}^{(2)}\cdot\mathsf{a}^{(2)}) \\ &+ \beta_5 S(\mathsf{a}^{(2)}\otimes\mathsf{a}^{(2)}\cdot\mathsf{a}^{(2)}) + \beta_6 S(\mathsf{a}^{(2)}\cdot\mathsf{a}^{(2)}\otimes\mathsf{a}^{(2)}\cdot\mathsf{a}^{(2)}), \end{aligned} \tag{5.16}$$

where I is the identity tensor and S indicates the symmetric part of its arguments, as

$$\begin{aligned} &S(T_{ijkl}) = \\ &\quad \frac{1}{24}(T_{ijkl} + T_{jikl} + T_{ijlk} + T_{jilk} + T_{klij} + T_{lkij} + T_{klji} + T_{lkji} + T_{ikjl} \\ &\quad +T_{kijl} + T_{iklj} + T_{kilj} + T_{jlik} + T_{ljik} + T_{jlki} + T_{ljki} + T_{iljk} \\ &\quad +T_{lijk} + T_{ilkj} + T_{likj} + T_{jkil} + T_{kjil} + T_{jkli} + T_{kjli}). \end{aligned} \tag{5.17}$$

Introducing Eq. (5.17) into Eq. (5.16) results in the following equation

$$\begin{aligned} a^{(4)}_{ijkl} &= \beta_1(\delta_{ij}\delta_{kl} + \delta_{ik}\delta_{jl} + \delta_{il}\delta_{jk})/3 \\ &+ \beta_2(\delta_{ij}a^{(2)}_{kl} + \delta_{kl}a^{(2)}_{ij} + \delta_{ik}a^{(2)}_{jl} + \delta_{il}a^{(2)}_{jk} + \delta_{jl}a^{(2)}_{ik} + \delta_{jk}a^{(2)}_{il})/6 \\ &+ \beta_3(a^{(2)}_{ij}a^{(2)}_{kl} + a^{(2)}_{ik}a^{(2)}_{jl} + a^{(2)}_{il}a^{(2)}_{jk})/3 \\ &+ \beta_4(\delta_{ij}b_{kl} + \delta_{kl}b_{ij} + \delta_{ik}b_{jl} + \delta_{il}b_{jk} + \delta_{jl}b_{ik} + \delta_{jk}b_{il})/6 \\ &+ \beta_5(a^{(2)}_{ij}b_{kl} + a^{(2)}_{kl}b_{ij} + a^{(2)}_{ik}b_{jl} + a^{(2)}_{il}b_{jk} + a^{(2)}_{jl}b_{ik} + a^{(2)}_{jk}b_{il})/6 \\ &+ \beta_6(b_{ij}b_{kl} + b_{ik}b_{jl} + b_{il}b_{jk}/3, \end{aligned} \tag{5.18}$$

with $b_{ij} = a^{(2)}_{im} a^{(2)}_{mj}$. The coefficients $\beta_1 - \beta_6$ are functions of the second and third invariants (II, III) of $a^{(2)}_{ij}$. It can be show that there are only three independent β_i's among the six β_i's given in Eq. (5.18) and the rest can be expressed in terms of the three independent coefficients. Chung and Kwon (2002) have proposed to choose β_3, β_4 and β_6 as independent coefficients, the rest being expressed in terms of those coefficients and the invariants. We adopt this choice, so that β_1, β_2 and β_5 are given by (Chung and Kwon, 2002):

$$\begin{aligned} \beta_1 &= \frac{3}{5}[-\frac{1}{7} + \frac{1}{5}\beta_3 \left(\frac{1}{7} + \frac{4}{7} II + \frac{8}{3} III\right) - \beta_4 \left(\frac{1}{5} - \frac{8}{15} II - \frac{14}{15} III\right) \\ &- \beta_6 \left(\frac{1}{35} - \frac{24}{105} III - \frac{4}{35} II + \frac{16}{15} II\ III + \frac{8}{35} II^2\right)]. \end{aligned}$$

$$\beta_2 = \frac{6}{7}\left[1 - \frac{1}{5}\beta_3 \left(1 + 4\ II\right) + \frac{7}{5}\beta_4 \left(\frac{1}{6} - II\right) - \beta_6 \left(-\frac{1}{5} + \frac{2}{3} III + \frac{4}{5} II - \frac{8}{5} II^2\right)\right].$$

$$\beta_5 = -\frac{4}{5}\beta_3 - \frac{7}{5}\beta_4 - \frac{6}{5}\beta_6 \left(1 - \frac{4}{3} II\right). \tag{5.19}$$

Finally, the functional forms of the independent coefficients β_3, β_4 and β_6 must be determined in terms of the second and third invariants, II and III. Chung and Kwon (2002) have proposed the fifth order polynomial functions defined as

$$\begin{aligned} \beta_i &= C(i,1) + C(i,2)\ II + C(i,3)\ II^2 + C(i,4)\ III + C(i,5)\ III^2 \\ &+ C(i,6)\ II\ III + C(i,7)\ II^2\ III + C(i,8)\ II\ III^2 + C(i,9)\ II^3 \\ &+ C(i,10)\ III^3 + C(i,11)\ II^3\ III + C(i,12)\ II^2\ III^2 \\ &+ C(i,13)\ II\ III^3 + C(i,14)\ II^4 + C(i,15)\ III^4 \\ &+ C(i,16)\ II^4\ III + C(i,17)\ II^3\ III^2 + C(i,18)\ II^2\ III^3 + C(i,19)\ II\ III^4 \\ &+ C(i,20)\ II^5 + C(i,21)\ III^5 \quad (i = 3,4,6), \end{aligned} \tag{5.20}$$

where

$$II = \frac{1}{2}(1 - a^{(2)}_{ij} a^{(2)}_{ji},$$

$$III = a^{(2)}_{11}(a^{(2)}_{22} a^{(2)}_{33} - a^{(2)}_{23} a^{(2)}_{32}) + a^{(2)}_{12}(a^{(2)}_{23} a^{(2)}_{31} - a^{(2)}_{21} a^{(2)}_{33}) + a^{(2)}_{13}(a^{(2)}_{21} a^{(2)}_{32} - a^{(2)}_{22} a^{(2)}_{31}).$$

Eq. (5.18) can be further reduced and categorized according to the number of identical indices in a_{ijkl}, as follows:

- Groupe 1: $a^{(4)}_{1111}$, $a^{(4)}_{2222}$,

$$a^{(4)}_{iiii} = \beta_1 + \beta_2 a^{(2)}_{ii} + \beta_3 (a^{(2)}_{ii})^2 + \beta_4 b_{ii} + \beta_5 a^{(2)}_{ii} b_{ii} + \beta_6 (b_{ii})^2, \tag{5.21}$$

  where $i = 1, 2$ (no sum on i).

- Group 2: $a^{(4)}_{1122}$,

$$\begin{aligned} a^{(4)}_{1122} &= \frac{\beta_1}{3} + \frac{\beta_2}{6}(a^{(2)}_{22} + a^{(2)}_{11}) + \frac{\beta_3}{3}(a^{(2)}_{11} a^{(2)}_{22} + 2(a^{(2)}_{12})^2) + \frac{\beta_4}{6}(b_{22} + b_{11}) \\ &+ \frac{\beta_5}{6}(a^{(2)}_{11} b_{22} + a^{(2)}_{22} b_{11} + 4a^{(2)}_{12} b_{12}) + \frac{\beta_6}{3}(b_{11} b_{22} + 2(b_{12})^2). \end{aligned} \tag{5.22}$$

- Group 3: $a^{(4)}_{1123}$, $a^{(4)}_{2231}$,

$$\begin{aligned} a^{(4)}_{ijkl} &= \frac{\beta_2}{6} a^{(2)}_{kl} + \frac{\beta_3}{3}(a^{(2)}_{ij} a^{(2)}_{kl} + 2a^{(2)}_{ik} a^{(2)}_{jl}) + \frac{\beta_4}{6} b_{kl} \\ &+ \frac{\beta_5}{6}(a^{(2)}_{ij} b_{kl} + a^{(2)}_{kl} b_{ij} + 2a^{(2)}_{ik} b_{jl} + 2a^{(2)}_{jl} b_{ik}) + \frac{\beta_6}{3}(b_{ij} b_{kl} + 2b_{ik} b_{jl}). \end{aligned} \tag{5.23}$$

- Group 4: $a^{(4)}_{1131}$, $a^{(4)}_{1112}$, $a^{(4)}_{2223}$, $a^{(4)}_{2212}$,

$$a^{(4)}_{ijkl} = \frac{\beta_2}{2} a^{(2)}_{kl} + \beta_3 a^{(2)}_{ij} a^{(2)}_{kl} + \frac{\beta_4}{2} b_{kl} + \frac{\beta_5}{2}(a^{(2)}_{ij} b_{kl} + 3a^{(2)}_{kl} b_{ij}) + \beta_6 b_{ij} b_{kl}. \tag{5.24}$$

To determine the values of $C(i, j)$ in Eq. (5.20), a optimal fitting procedure is employed to provide a best fit to presumably exactly $a^{(4)}_{ijkl}$ obtained from an orthotropic ODF. Given the orthotropic nature of the IBOF, an orthotropic ODF provides a good fitting solution, so that following Gillet-Chaulet and others (2006), we use the ODF proposed by Gagliardini (1999), defined as

$$\begin{aligned} f^*(\theta, \varphi, k_1, k_2, k_3) &= \frac{1}{[\sin^2\theta(k_1^2\ \cos^2\varphi + k_2^2\ \sin^2\varphi) + k_3^2\ \cos^2\theta]^{3/2}}, \\ & k_1 k_2 k_3 = 1. \end{aligned} \tag{5.25}$$

For different states of fabrics given by the coefficients k_1, k_2 and k_3, Eq. (5.25) is computed, so that exact $a^{(2)}$ and $a^{(4)}$ can be evaluated by using Eq. (5.2). Solutions of $a^{(2)}$ from the ODF are then used to computes the approximated $a^{(4)}$ with Eq. (5.18). The values of the coefficients $C(i, j)$ are then obtained so that they minimize

$$\chi^2 = \sum_{l=1}^{N} (a^{(4)}_{ODF} - a^{(4)}_{IBOF}) \ :: \ (a^{(4)}_{ODF} - a^{(4)}_{IBOF}) \tag{5.26}$$

where N is the number of discretization points in the space of orientations such that $k_1 \leq k_2 \leq k_3$ [Gagliardini (1999), Gillet-Chaulet and others (2006)].

5.6 Conclusion

We have presented in this chapter the finite-element implementation of the anisotropic flow law together with the fabric evolution equation. An approach based on orientation tensors has been developed in order to allow for realistic time computation for large scale modeling. The implementation uses an Invariant-Based Optimal Fitting Closure approximation for the computation of the fourth-order tensor, function of the second-order tensor. Those tensors are used for the computation of the polycrystal deformability and the fabric evolution equation is therefore formulated by means of the evolution of the second-order tensor. The next chapter will present the application of this formulation for the modeling of the dynamics at the vicinity of Dome Fuji.

Chapter 6

Full-Stokes finite-element model for the vicinity of Dome Fuji

6.1 Introduction

In this section we are interested in modeling the flow in the vicinity of Dome Fuji. With an altitude of 3810 m, Dome Fuji is the second-highest summit of the Antarctic ice sheet and represents an ice divide. Owing to its location on the Antarctic plateau and the high elevation, it is one of the coolest places on Earth. Temperature rarely rise above -30°C in summer and can drop to -80°C in winter. The climate is that of a cold desert, with very dry conditions and an annual precipitation of about 27 millimeters of water equivalent, which falls entirely as snow.

A detailed description of the surface and bedrock topography is given by the fine resolution mapping (60 x 60 km domain, 500 m resolution) which was carried out there [Watanabe and others (2003); Fujita, S.; personal communication 2006]. The surface topography of the Dome Fuji area is smooth and flat. Surface elevations around 30 km from the dome summit are only 7 m to 30 m lower than at the summit. The mean surface slope in the circle of radius 30 km is estimated at about 1/1500 (Watanabe and others, 2003). The bedrock topography around the dome exhibits bedrock hills located to the southeast and northwest, and lowlands located to the west.

Dome Fuji deep ice core drilling was started in August 1995, and in December 1996 a depth of 2503 m was reached. This first core covers a period back to 340 ka. A second deep core was started in 2003. Drilling was carried out during four subsequent austral summers from 2003/2004 until 2006/2007 and by then a depth of 3035.22 m was reached. The drill did not hit the bedrock, but rock particles and refrozen water have been found in the deepest ice, indicating that the bedrock is close to the bottom of the borehole (Motoyama, 2007). This core greatly extends the climatic record of the first core, with preliminary dating indicating an age of $\sim$ 720-750 ka. The determination of the ice age for the first core has been realized using a method that gives the O_2/N_2 ratio of trapped air (Kawamura and others, 2007). This ratio is a proxy for the local summer insolation at the deposition sites, but because the O_2/N_2 fractionation during bubble formation is determined by the physical properties of surrounding ice, this method allows determining the age of ice. Ice-core air was extracted with a melting technique and measured with a mass spectrometer with $1\,\sigma$ uncertainties of 0.2‰, 0.02‰ and 0.04‰ for $\delta(O_2/N_2)$, $\delta^{15}N$ of N_2 and $\delta^{18}O$ of O_2, respectively. The O_2/N_2 and $\delta^{18}O$ were corrected for gravitational enrichment in the firn by subtracting 4 x $\delta^{15}N$ and 2 x $\delta^{15}N$, respectively. Because O_2/N_2 in clathrate ice gradually becomes depleted over years in a warm freezer ($-25°C$) owing to diffusive gas loss, the data were corrected according to the storage period. Also, in order to improve and extend the Dome Fuji O_2/N_2 time scale, tie points at 221.2, 230.8 and 334.9 ka ago were used from the Vostok core, by transferring them to the Dome Fuji core by visual matching of the isotopic records.

The second core has been dated by measuring the oxygen isotope ratio $\delta^{18}O$ of the ice core (Motoyama, 2007). The ice age was then estimated by comparing (synchronizing) the determined age with the Dome C ice core data from the European Project for Ice Coring in Antarctica (EPICA). The Dome C ice core age scale (EDC3) was constructed in three stages (Parrenin and others, 2007). The preliminary dating was first obtained by ice flow modeling where the initial annual layer thickness was evaluated from the deuterium content of ice, and the total thinning ratio was then evaluated with a mechanical model. The ice flow model parameters, the average Holocene accumulation, the slope between deuterium and logarithm of accumulation, the basal melting and the two parameters for the vertical profile of velocity (basal sliding and internal deformation) have been determined by independent age markers, using a Monte Carlo Markov Chain inverse method. For the second stage, an a posteriori strict match of the age scale to dated volcanoes and to the NorthGRIP GICC05 time scale in the top part was realized. Finally, the third stage was a correction of the modeling thinning function in the bottom 500 m of the core, where the ice flow model is unable to fit the $\delta^{18}O_{atm}$ age markers.

We are interested in the application of our anisotropic flow model to the vicinity of the location of the Dome Fuji ice core so that the model can be used for better interpretation of the core. We present first the general finite-element method employed and the model settings required for the simulation. We introduce the domain geometry, equations that are solved, and the boundary conditions. We study then the results obtained with isotropic conditions and we compare them with the anisotropic solution. The field variables velocity, temperature and age are compared and the fabric evolution is discussed.

6.2 Field equations

6.2.1 Stokes equation

For the flow of ice sheets, the acceleration term is negligible so that the equation of motion is given by

$$-\mathrm{grad}\; p + \eta \nabla^2 \mathbf{v} + (\nabla \mathbf{v} + (\nabla \mathbf{v})^T) \cdot \nabla \eta + \rho \mathbf{g} = \mathbf{0}, \tag{6.1}$$

where p is the pressure, η is the viscosity [Eq. (3.15)], $\mathbf{v}$ is is the velocity vector, ρ is the ice density and $\mathbf{g}$ is the gravity acceleration ($g = |\mathbf{g}| = 9.81\,\mathrm{m\,s^{-2}}$). The ice is supposed incompressible (density-preserving) and therefore the mass balance applies,

$$\mathrm{div}\; \mathbf{v} = 0. \tag{6.2}$$

The constitutive relation for the ice is given by Eq. (3.7). For isotropic simulations, $\hat{E}(\mathcal{A})$ equals one.

6.2.2 Temperature equation

From the general internal-energy balance equation, the equation for the temperature field is given by,

$$\rho c(\frac{\partial T}{\partial t} + \mathbf{v} \cdot \nabla T) = \nabla \cdot (k \nabla T) + 4\eta d^2, \tag{6.3}$$

where T is the temperature, c is the specific heat and k is the heat conductivity. The term $4\eta d^2$ accounts for strain heating. The terms c and k are dependent on the temperature (hence the non-linearity of Eq. 6.3) and are given by

$$c(T) = (146.3 + 7.253\; T[K])\; \mathrm{J\,kg^{-1}\,K^{-1}}, \tag{6.4}$$

$$k(T) = 9.828e^{-0.0057\ T[k]}\ \mathrm{W\,m^{-1}\,K^{-1}}. \tag{6.5}$$

6.2.3 Age equation

The evolution of the age A of a particle of ice is given by

$$\frac{\partial A}{\partial t} + \mathbf{v} \cdot \nabla A = 1. \tag{6.6}$$

This equation is linear.

6.2.4 Fabric equation

The evolution of the fabric is given by Eq. (5.14) developed in the previous chapter.

6.3 Variational formulations and numerical methods

The field equations are solved using the finite-element method with the open source multi-physics package Elmer (Center for Scientific Computing (CSC), Finland, http://www.csc.fi /elmer/). In the following, the integration by parts are carried out by using Green's theorem (Appendix H).

6.3.1 Stokes equation

The variational formulations of Eqs. (6.1) and (6.2) can be derived by formulating Eq. (6.1) in general form as

$$T_{ij,j} + \rho g_i = 0, \tag{6.7}$$

where T is the Cauchy stress tensor given by

$$\mathsf{T} = -p\mathsf{1} + \mathsf{S}.$$

Integration by part using test functions Φ(scalar) and $\boldsymbol{\Phi}$(vector) gives

$$\int_V v_{i,i} \Phi \, dV = 0$$

$$\int_V (S_{ij} - p\delta_{ij}) \Phi_{i,j} \, dV = \oint_{\partial V} (S_{ij} - p\delta(ij) n_j \Phi_i \, dS - \rho \int_V g_i \Phi_i \, dV. \tag{6.8}$$

The unknown variables $\mathbf{v}$ and p are discretized with the interpolation functions

$$\mathbf{v} = \Psi_i v^i \qquad \text{and} \qquad p = \Psi_i p^i, \tag{6.9}$$

where v^i and p^i are the values of the velocity and pressure at the finite-element mesh node i. The solution of Eq. (6.8) is obtained with the method of residual bubbles (Baiocchi and others, 1993). This method is a stabilization method which introduces virtual nodes and interpolation functions for the variable velocity. This insures that the pressure is interpolated with polynomials of fewer degrees than the one used for the velocity.

6.3.2 Fabric evolution

By defining the vector $\mathbf{A} = (a^2_{11}, a^2_{22}, a^2_{12}, a^2_{23}, a^2_{13})$ for the components of the second-order orientation tensor to be solved, Eq. (5.14) can be rewritten as (cf. also Appendix G)

$$\frac{\partial A_i}{\partial t} + \mathbf{v} \cdot \nabla A_i + k_i A_i = f_i \quad (i = 1, ..., 5). \tag{6.10}$$

By multiplying Eq. (6.10) by a test function Φ and by integrating on the volume V, we obtain

$$\int_V \frac{\partial A_i}{\partial t} \Phi \, dV + \int_V v_k \frac{\partial A_i}{\partial x_k} \Phi \, dV + \int_V k A_i \Phi \, dV = \int_V f \Phi \, dV \tag{6.11}$$

And after integration by part, it follows

$$\begin{aligned} &\int_V \frac{\partial A_i}{\partial t} \Phi \, dV - \int_V A_i \frac{\partial v_k}{\partial x_k} \Phi \, dV - \\ &\quad \int_V A_i \frac{\partial \Phi}{\partial x_k} v_k \, dV + \int_V k A_i \Phi \, dV = \int_V f \Phi \, dV - \oint_{\partial V} A_i v_k n_k \Phi \, dS. \end{aligned} \tag{6.12}$$

A Dirichlet type boundary condition shall be prescribed on the boundary S when the velocity is entering the domain. Eq. (5.14) being a transport (hyperbolic type) equation without a diffusive term, the variational equation (Eq. 6.12) can not be solved with the classic Galerkin method. The solution is computed instead using the discontinuous Galerkin method (Brezzi and others, 2004).

6.3.3 Temperature equation

The temperature field T is discretized with

$$T = \Psi_j T^j, \tag{6.13}$$

where T^j is the value of T at the finite-element mesh node j and Ψ_j are the interpolation functions. In order to obtain the variational formulation of Eq. (6.3), we first rewrite this equation in the form

$$\rho c(\frac{\partial T}{\partial t} + \mathbf{v} \cdot \nabla T) = \nabla \cdot (k \nabla T) + \mathsf{S} : \mathsf{D}.$$

The variational formulation is then given by

$$\begin{aligned} \rho c \frac{\partial T^j}{\partial t} \int_V \Psi_j \Phi \, dV + T^j \int_V (\rho c v_i \Psi_{j,i} \Phi + k \Psi_{j,i} \Phi_{,i}) \, dV = \\ T^j \oint_{\partial V} k \Psi_{j,i} \Phi n_i \, dS + \int_V \mathsf{D} : \mathsf{S} \; \Phi \, dV. \end{aligned} \tag{6.14}$$

Stabilization methods of type residual bubbles (Baiocchi and others, 1993) or more general methods [Franca and others (1992), Franca and Frey (1992)] are employed to obtain the solution of Eq. (6.14). Boundary conditions are of Dirichlet type (imposed at the surface) or Newman type (heat flux at the bedrock).

6.4 Steady state solution procedure

Every field equations that govern the flow (Stokes, temperature, fabric) depend on the solution of others. The solution is therefore obtained by coupling the equations. For a steady state isotropic simulation (diagnostic), the algorithm is the following

- (1) A steady-state linear solution is computed for the velocity $\mathbf{v}$ and the pressure p. The viscosity is assumed to be linear and temperature independent. The non-linearity of the Stokes equation is treated within a Picard type iteration.

- (2) A solution for the temperature field T is computed from step (1) using the uncoupled linear solution for the velocity. The non-linearity of the temperature equation is treated within a Picard type iteration.

- (3) The solution of step (2) is then used as initial condition to compute the thermo-mechanical non-linear solution. The coupled system (flow and temperature) is solved with a Picard type iteration.

- (4) The solution for the age is computed when the coupled system for the flow and the temperature has converged.

The convergence criteria for the solution vector $\mathbf{q}$ at the iteration n for both the non-linearity iterations and the coupling iterations is given by

$$||q_{(n)} - q_{(n-1)}|| \leq \epsilon ||q_{(n)}||, \tag{6.15}$$

where $||q_{(n)}||$ is the norm defined by

$$||q_{(n)}|| = \sqrt{\sum_{1}^{N} (q^i)^2}, \tag{6.16}$$

where q^i is the value of $\mathbf{q}$ at the nodes i and N is the total number of nodes.

In order to compute the fabric evolution equation, the obtained steady state isotropic solution for the flow and the temperature is used as initial condition. Given the nature of the fabric evolution equation, the solution is obtained with a time discretization scheme using the Backward Differences Formulae (BDF) method with isotropic conditions everywhere in the domain as initial condition for the fabric. The coupling between fabric and flow is introduced by the viscosity term η in Eq. (6.1). In Appendix I, we formulate again the equation that computes the viscosity, function of the type of the power law which relates the deviatoric stress tensor S to the deformation rate tensor D used in Elmer.

6.5 Boundary conditions

We adopt in the following a Cartesian coordinate system, where x and y lie in the horizontal plane and z is positive upward

6.5.1 Free surface

At the free surface $h(x, y)$,

- Stress free condition is assumed so that the momentum jump condition reduces to

$$\mathsf{T}\,\mathbf{n} = 0 \tag{6.17}$$

- The fabric is assumed isotropic and the second-order orientation $\mathsf{a}^{(2)}$ reads

$$\mathsf{a}^{(2)} = \begin{pmatrix} 1/3 & 0 & 0 \\ 0 & 1/3 & 0 \\ 0 & 0 & 1/3 \end{pmatrix}. \tag{6.18}$$

- The age is null

$$A(h(x, y)) = 0.$$

- The temperature is prescribed as the measured annual mean air temperature at Dome Fuji (Watanabe and others, 2003).

$$T(h(x, y)) = -54.3°\text{C}.$$

6.5.2 Ice base

At the ice base, $b(x, y)$,

- No slip conditions is assumed

$$\mathbf{v}(b(x, y)) = 0 \tag{6.19}$$

- For the temperature equation, a geothermal heat flux is prescribed,

$$q_{geo} = 60 \text{ mW m}^{-2}.$$

  This value has been chosen in order to obtain pressure melting conditions as observed at the Dome Fuji ice core drilling site and to tune the basal melting to obtain values for the age close to the in-situ estimated basal age.

- In order to avoid infinite age at the ice base, we compute a vertical normal outflow velocity due to the ice melting. This basal melting velocity is computed by

$$a_b = \frac{1}{L\rho}(q_{geo} - q), \tag{6.20}$$

  where L is the latent heat for ice and the difference $q_{geo} - q$ gives the available heat for melting, with $q = |\mathbf{q}|$ being the heat flux into the ice, given by

$$\mathbf{q} = -k\nabla T. \tag{6.21}$$

6.5.3 Side boundaries

On the side boundaries, we prescribe shallow-ice stresses. With the Cauchy stress tensor T given by

$$\mathsf{T} = -\rho g(h-z)\begin{bmatrix} 1 & 1 & \frac{\partial h}{\partial x} \\ 0 & 1 & \frac{\partial h}{\partial y} \\ \frac{\partial h}{\partial x} & \frac{\partial h}{\partial y} & 1 \end{bmatrix} = \tag{6.22}$$

$$\begin{bmatrix} -\rho g(h-z) & 0 & -\rho g(h-z)\frac{\partial h}{\partial x} \\ 0 & -\rho g(h-z) & -\rho g(h-z)\frac{\partial h}{\partial y} \\ -\rho g(h-z)\frac{\partial h}{\partial x} & -\rho g(h-z)\frac{\partial h}{\partial y} & -\rho g(h-z) \end{bmatrix}, \tag{6.23}$$

$\mathsf{T}\,\mathbf{n}$ is

- On the northern boundary of the domain,

$$\begin{pmatrix} 0 \\ -\rho g(h-z) \\ -\rho g(h-z)\frac{\partial h}{\partial y} \end{pmatrix}. \tag{6.24}$$

- On the southern boundary,

$$\begin{pmatrix} 0 \\ \rho g(h-z) \\ \rho g(h-z)\frac{\partial h}{\partial y} \end{pmatrix}. \tag{6.25}$$

- On the eastern boundary,

$$\begin{pmatrix} -\rho g(h-z) \\ 0 \\ -\rho g(h-z)\frac{\partial h}{\partial x} \end{pmatrix}. \tag{6.26}$$

- On the western boundary,

$$\begin{pmatrix} \rho g(h-z) \\ 0 \\ \rho g(h-z)\frac{\partial h}{\partial x} \end{pmatrix}. \tag{6.27}$$

6.6 Finite-element mesh

The three dimensional finite-element mesh for the computational domain has been created with two topographic data sets, the fine resolution (500 m) data obtained at Dome Fuji [Watanabe and others (2003); Fujita, S.; personal communication 2006] and a coarse resolution (20.3092 km) data set created from the RAMPDEM V2/BEDMAP data sets [Liu and others (2001); Lythe and others (2000)]. The RAMPDEM V2/BEDMAP data sets were used to create a new topography for the surface and the bedrock with a $\sim$ 20 km resolution (Greve, R.; personal communication, Ice-Core-Consortium Dating-Reasearch Consortium meeting at NIPR, Tokyo, Japan, 2006). This new data set has then been merged with the fine resolution area, which represent a 60 x 60 km area around the Dome Fuji station, to create a single domain of 203.092 x 203.092 km size (Fig. 6.1). This procedure has been carried out in order to keep the lateral boundaries sufficiently far away from the dome, so that shallow-ice stresses can be prescribed there. The mesh consists of a coarse resolution near the boundaries (7 km) and a mesh resolution refinement (up to 500 m) towards the position of the dome located at the center of the domain. A first square domain (6 x 6 km) is meshed with mapped elements with a 500 m resolution. This domain is surrounded by a second square domain (60 x 60 km) meshed with mapped elements using a 6 km resolution. The connection between those two square sub-domains is performed with a resolution refinement towards the inner square. To connect the outer square to the domain boundaries, four sub-domains are created and meshed with paved elements. With a vertical resolution consisting of 20 layers, the resulting mesh contains 5406 bilinear quadrilateral elements and 30860 trilinear bricks elements for a total of 33642 nodes (Fig. 6.2). Finally, Fig. 6.3 and Fig. 6.4 show the free surface topography and the ice thickness inside the computational domain.

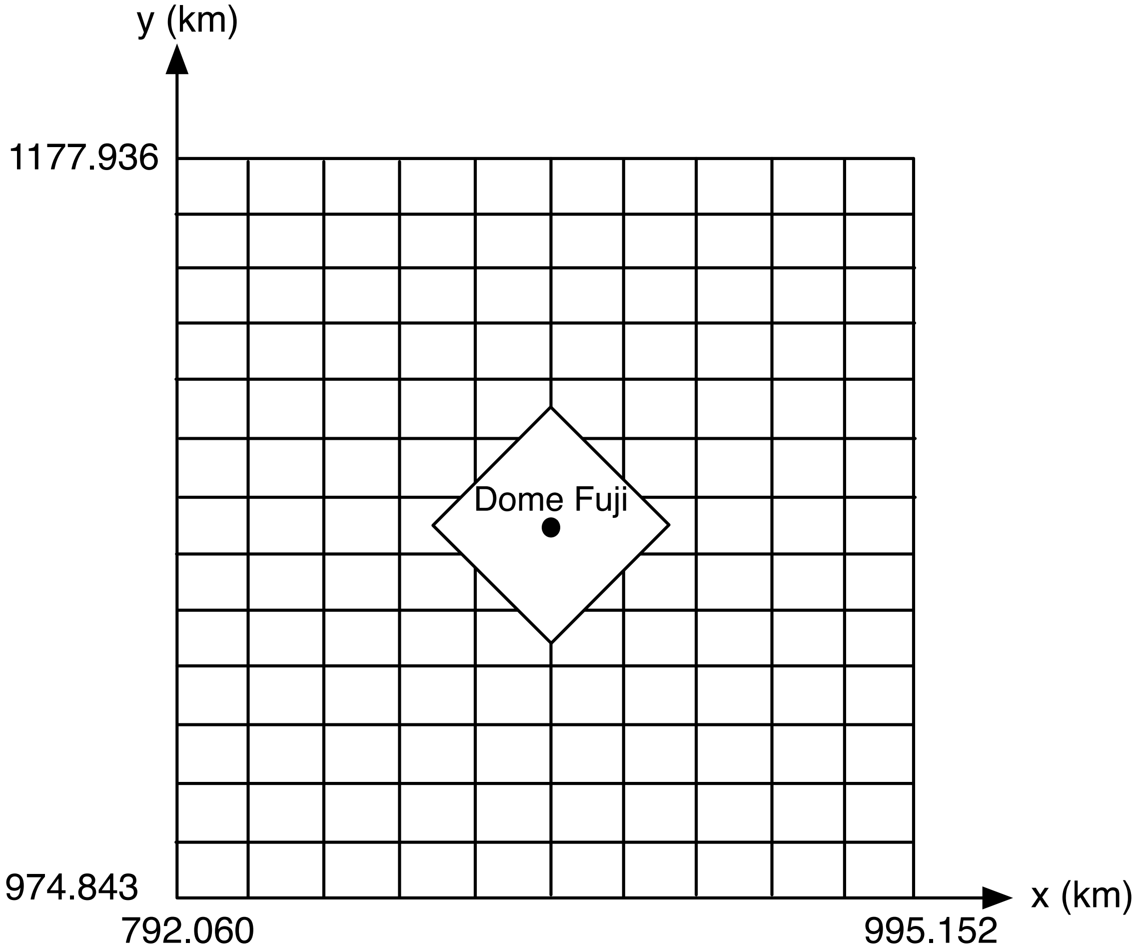

Figure 6.1: Domain of computation. The inner white square represents the fine resolution 60 x 60 km domain which is merged to the RAMPDEM V2/BEDMAP grid. The location of the domain relative to Antarctica is shown in Fig. 1.3.

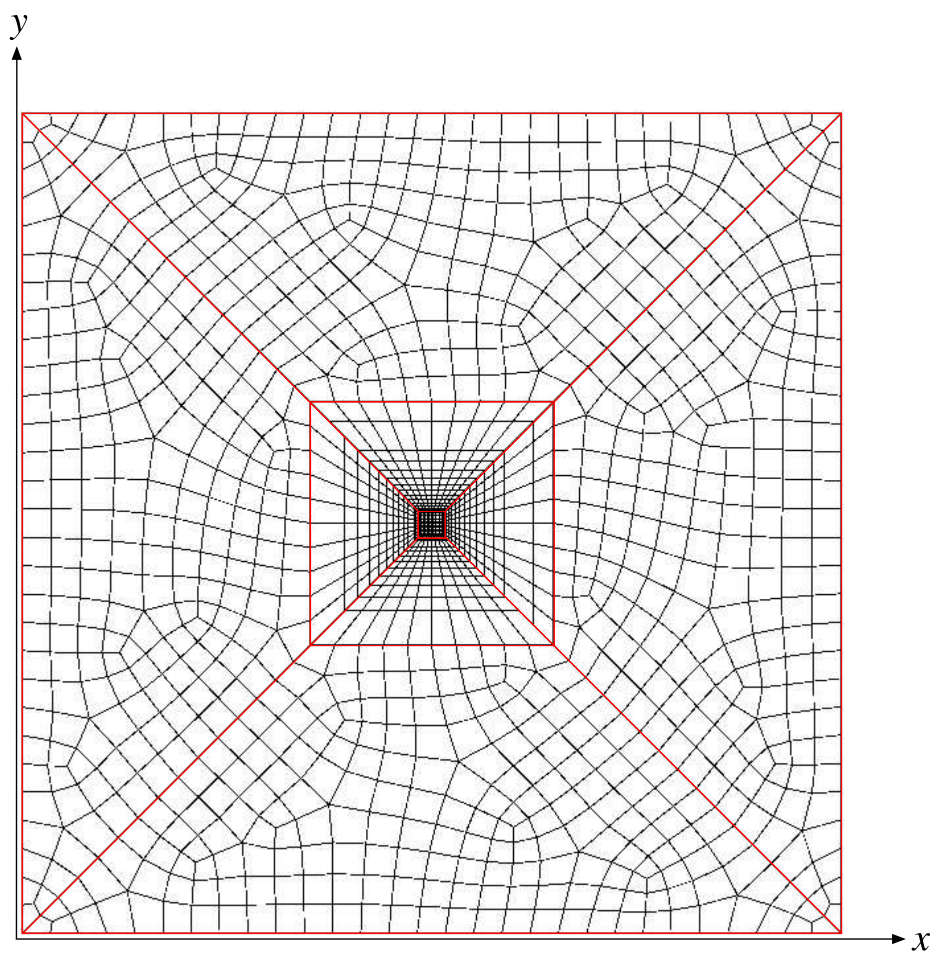

Figure 6.2: Finite-element mesh produced for the computation. Mesh created with the pre-processing software Gambit (Fluent-Ansys).

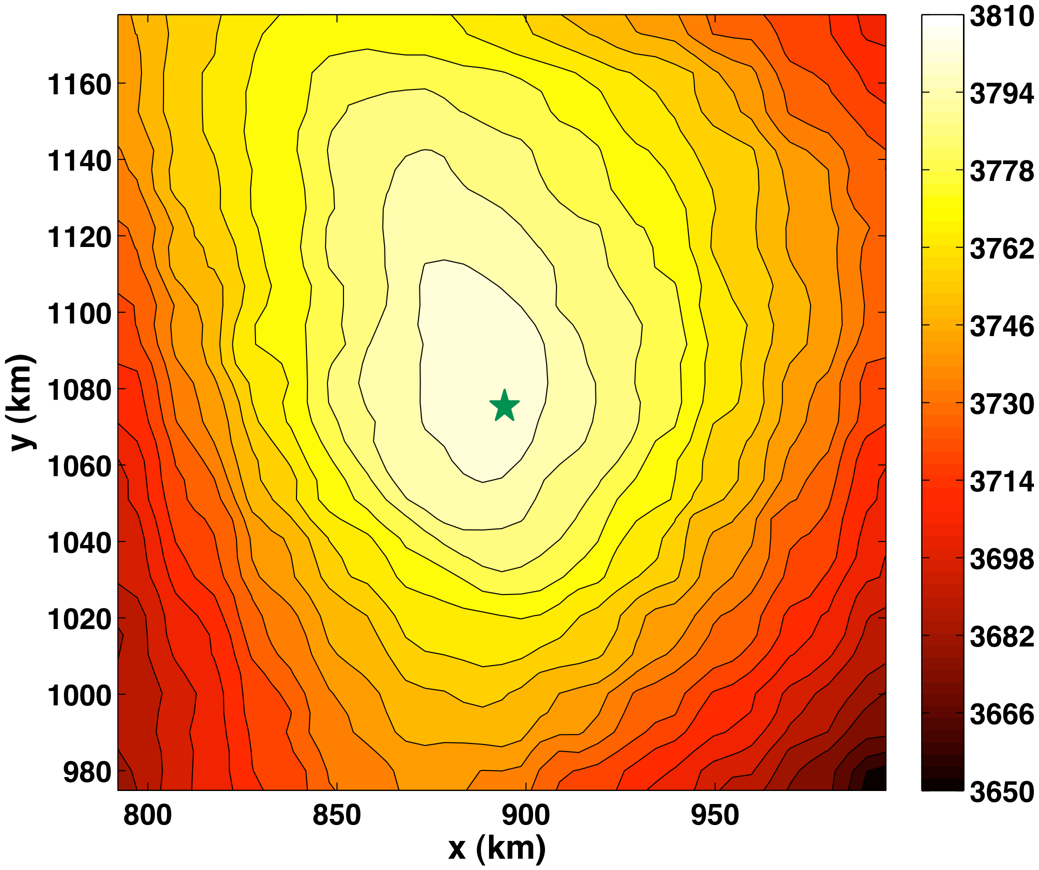

Figure 6.3: Free surface topography (m). Iso-contours at every 8 meters. The star indicates the location of the Dome Fuji ice core drilling site.

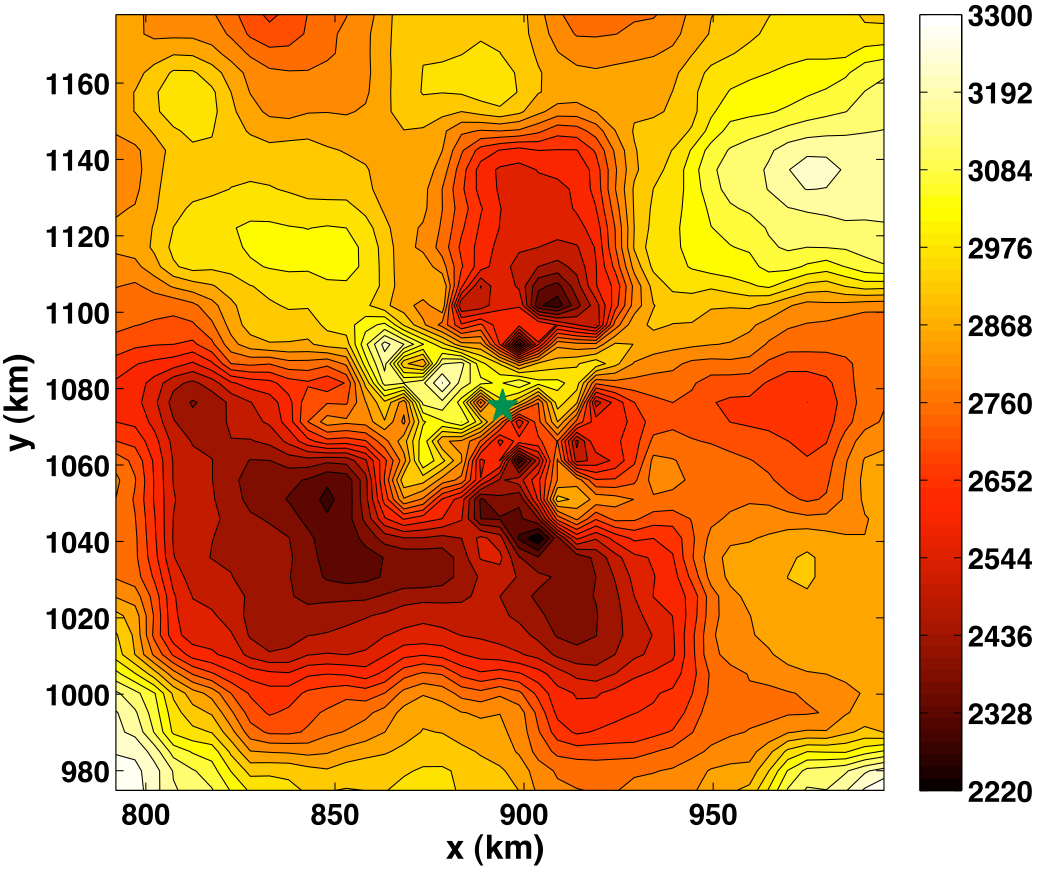

Figure 6.4: Ice thickness (m). The star indicates the location of the Dome Fuji ice core drilling site.

6.7 Steady-state isotropic simulation

6.7.1 Modeling of the flow

The isotropic steady state results for the horizontal velocity field are shown in Fig 6.5. We observe a good distribution of the velocity across the domain with slow dynamics at the center of the domain where the dome is located. The absolute values are in good agreement with what should expect in this region. We also observe that the velocity field is somewhat elongated as it seems that the flow is faster towards the x-direction. This

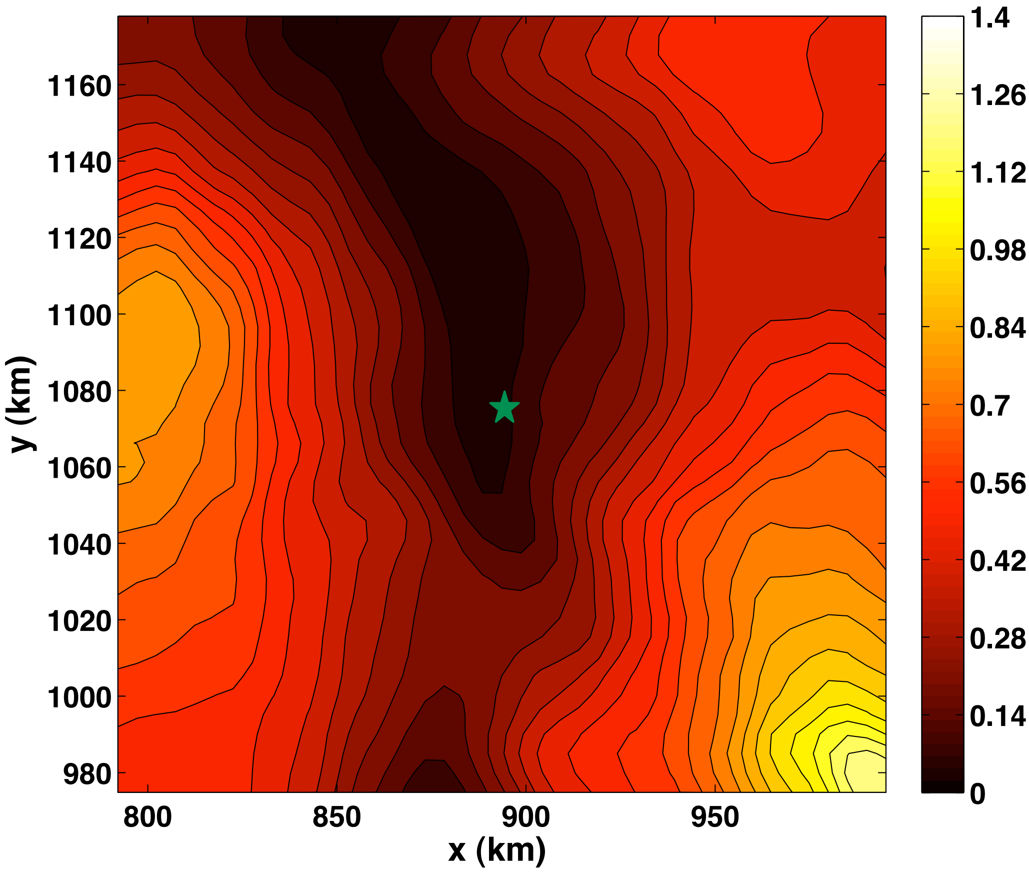

Figure 6.5: Surface horizontal velocities ($\mathrm{m\,a^{-1}}$) obtained with steady-state isotropic simulation. The star indicates the location of the Dome Fuji ice core drilling site.

can be better understood by inspection of Fig 6.6 which depicts the vector velocities. We observe that the flow of ice away from the dome is well reproduced and the vectors are perpendicular to the surface elevation iso-contours as shown in Fig 6.7

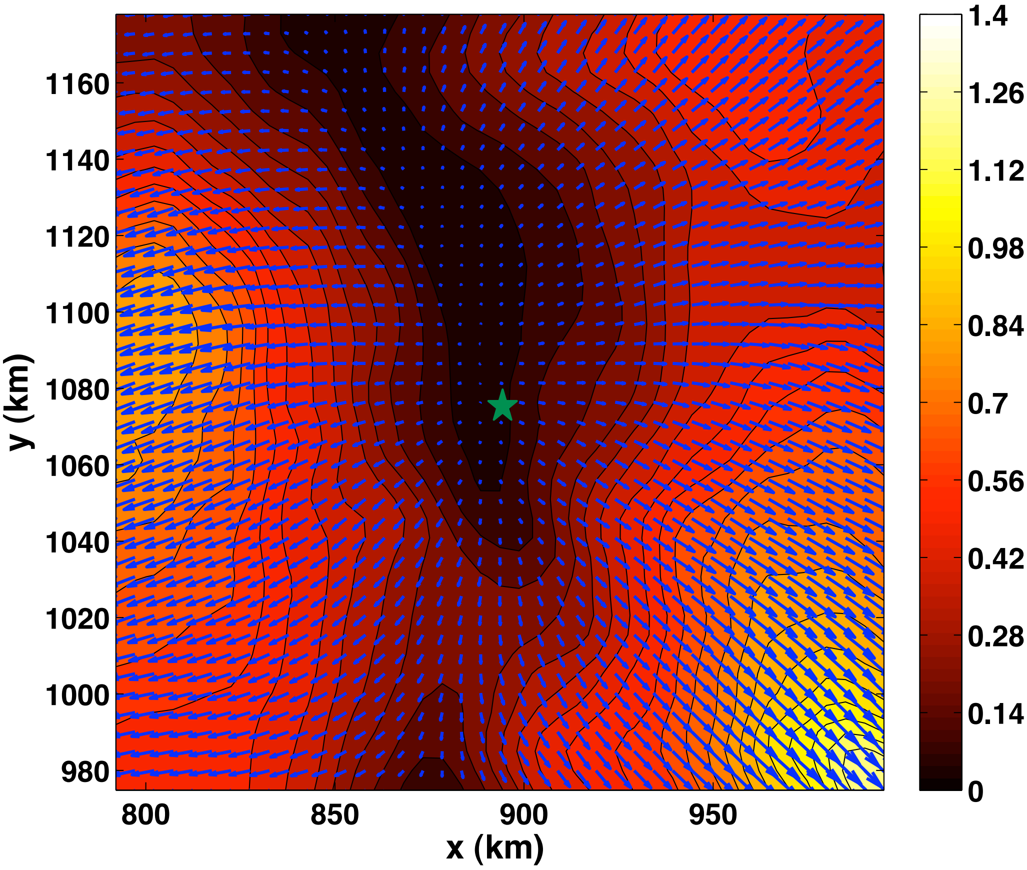

Figure 6.6: Surface horizontal velocities ($\mathrm{m\,a^{-1}}$) and associated vectors obtained with steady-state isotropic simulation. The star indicates the location of the Dome Fuji ice core drilling site.

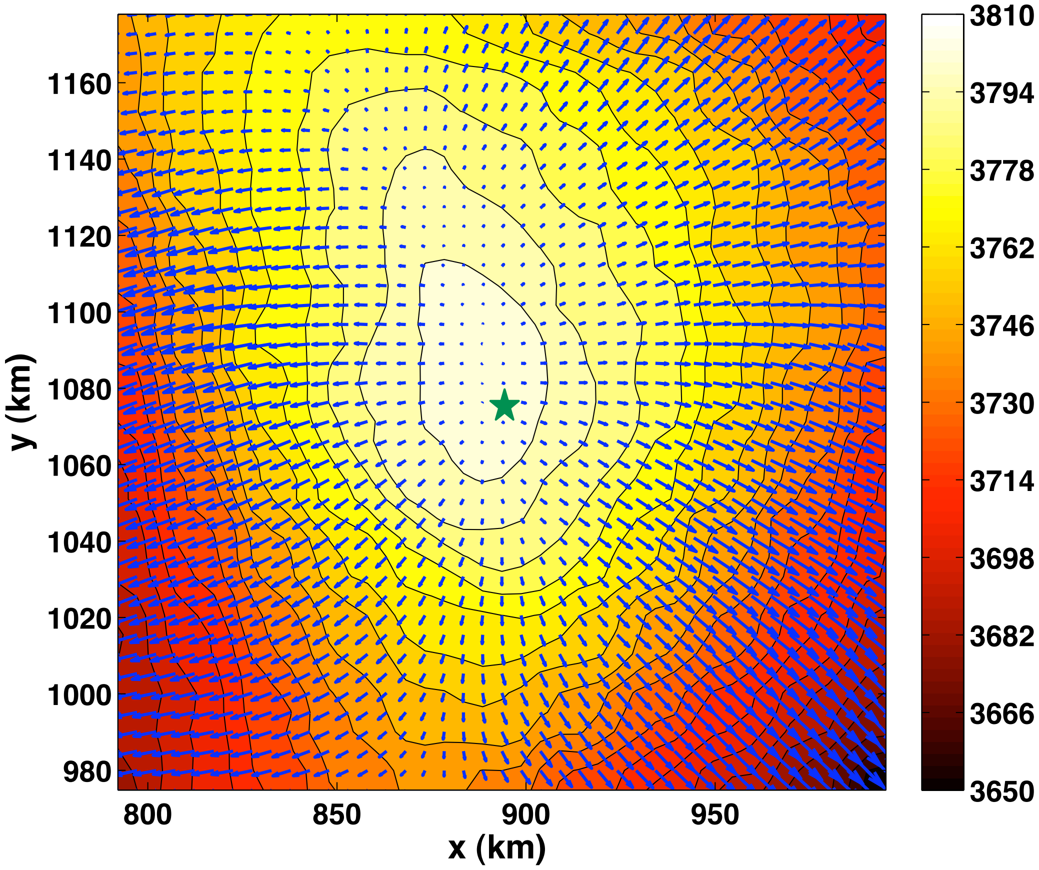

Figure 6.7: Free surface topography (m) and surface horizontal velocity vectors obtained with steady-state isotropic simulation. Iso-contours at every 8 meters. The star indicates the location of the Dome Fuji ice core drilling site.

The surface vertical velocity computed for the domain is shown in Fig 6.8. The vertical velocity at the vicinity of the dome is well reproduced in comparison to the observed surface accumulation, $27.3 \pm 1.5\ \mathrm{kg\,m^{-2}\,a^{-1}}$ (Kameda and others, 2008). However, we observe positive values for the vertical velocity at both the interior of the domain and across the boundaries. While the positive values across the boundaries might be associated with the boundary effects associated with the uncertain boundary conditions applied on the domain sides, at the interior domain, the topography of the bedrock can explain the regions where the vertical velocity is positive as the ice is lifted up due to the presence of ridges at the bedrock. This is also a consequence of the diagnostic simulation where the surface can't adjust itself to the ice flow dynamics.

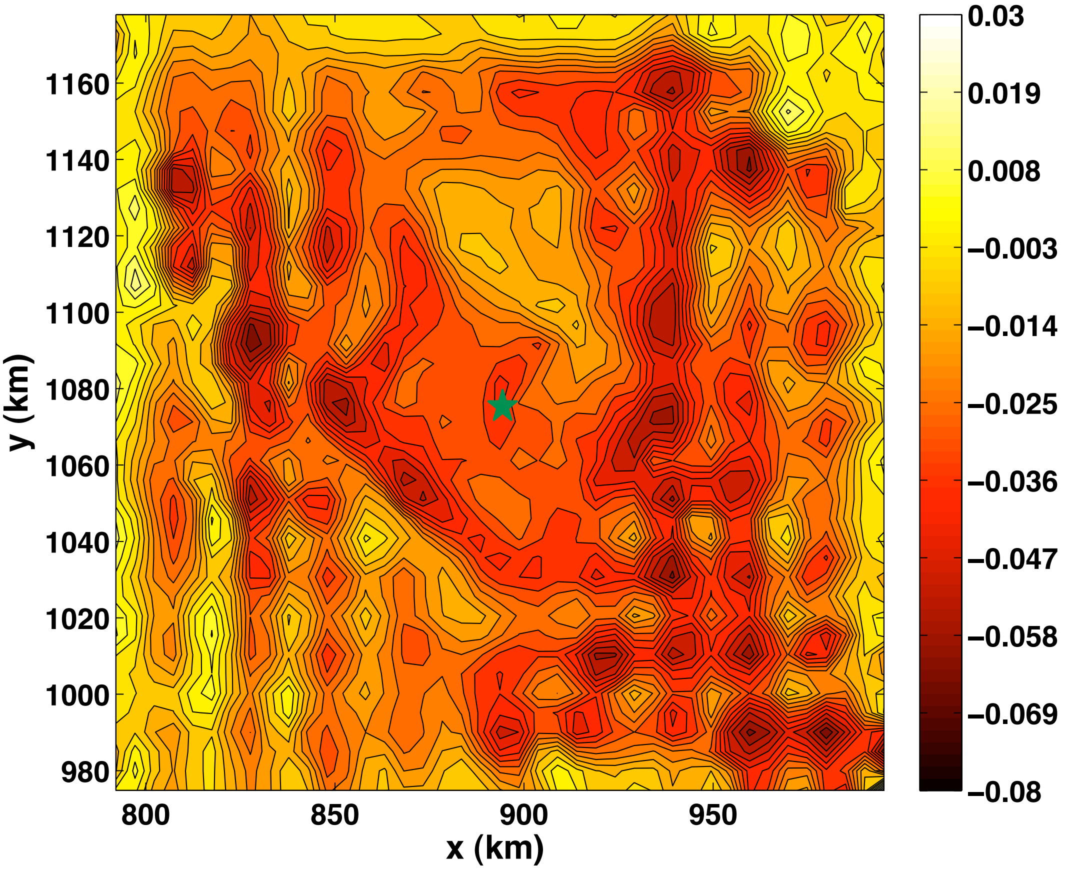

Figure 6.8: Surface vertical velocities ($\mathrm{m\,a^{-1}}$) obtained with steady-state isotropic simulation. The star indicates the location of the Dome Fuji ice core drilling site.

The relation between bedrock topography and horizontal velocity vectors at the surface is further considered in Fig 6.9. Although the velocity vectors are perpendicular to surface elevation iso-contours, we observe that the flow direction seems to be driven by the direction of the deep valley separating the two ridges located on the northern and souther part of the domain center. The faster horizontal velocities towards the x-direction are also a consequence of the orientation East-West of the valley (cf. Section 6.8).

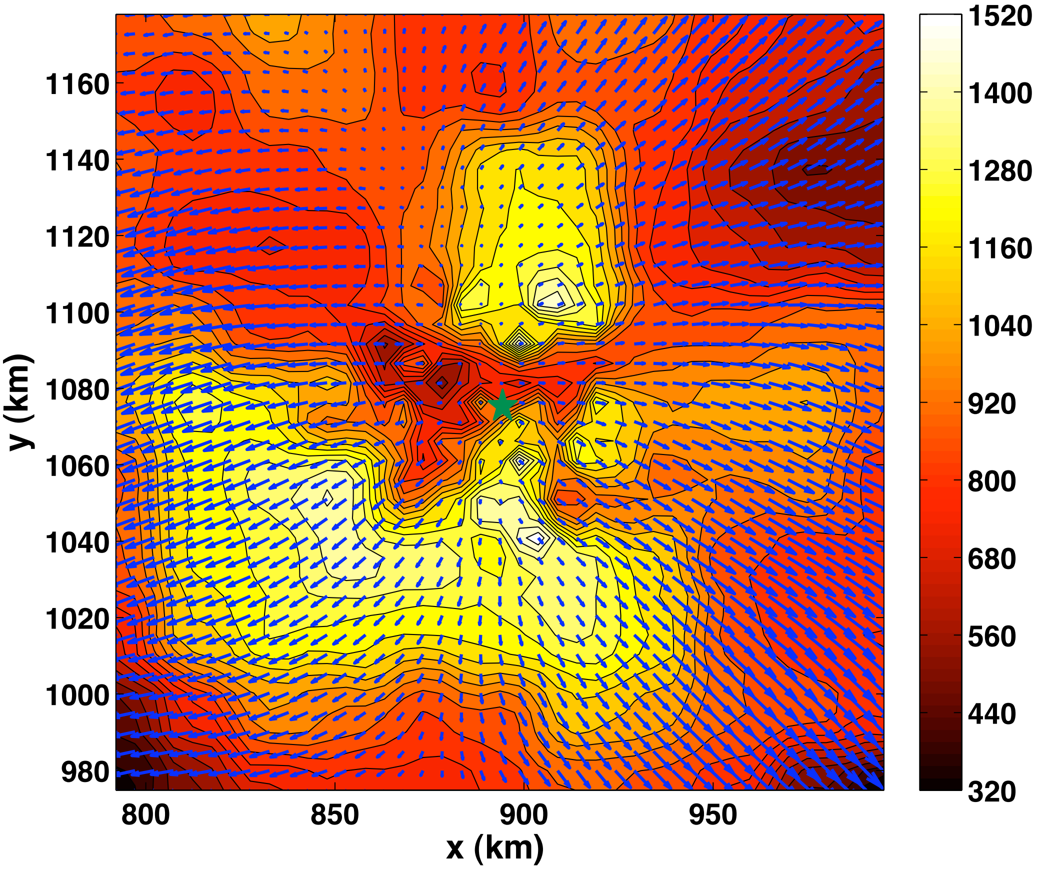

Figure 6.9: Bedrock elevation (m) and surface horizontal velocity vectors obtained with steady-state isotropic simulation. The star indicates the location of the Dome Fuji ice core drilling site.

6.7.2 Modeling of the temperature

The computed absolute temperature distribution is shown in Fig. 6.10. Given the prescribed geothermal heat flux, 60 mW m^{-2}, the model predicts large regions of ice at the melting point. Due to the uncertainties arising from a constant geothermal heat flux for all the domain, the distribution of the temperature by the model may not reflect the exact natural situation. We note however that those results fit well with the distribution of the ice thickness: warmer ice where the ice is thick and colder ice where the ice is thinner. At the location of the Dome Fuji ice core, ice at the melting point has been observed, which is also well reproduced by the model. The vertical distribution of the temperature is linear, with the linear warming from the surface towards the bedrock (Fig. 6.11).

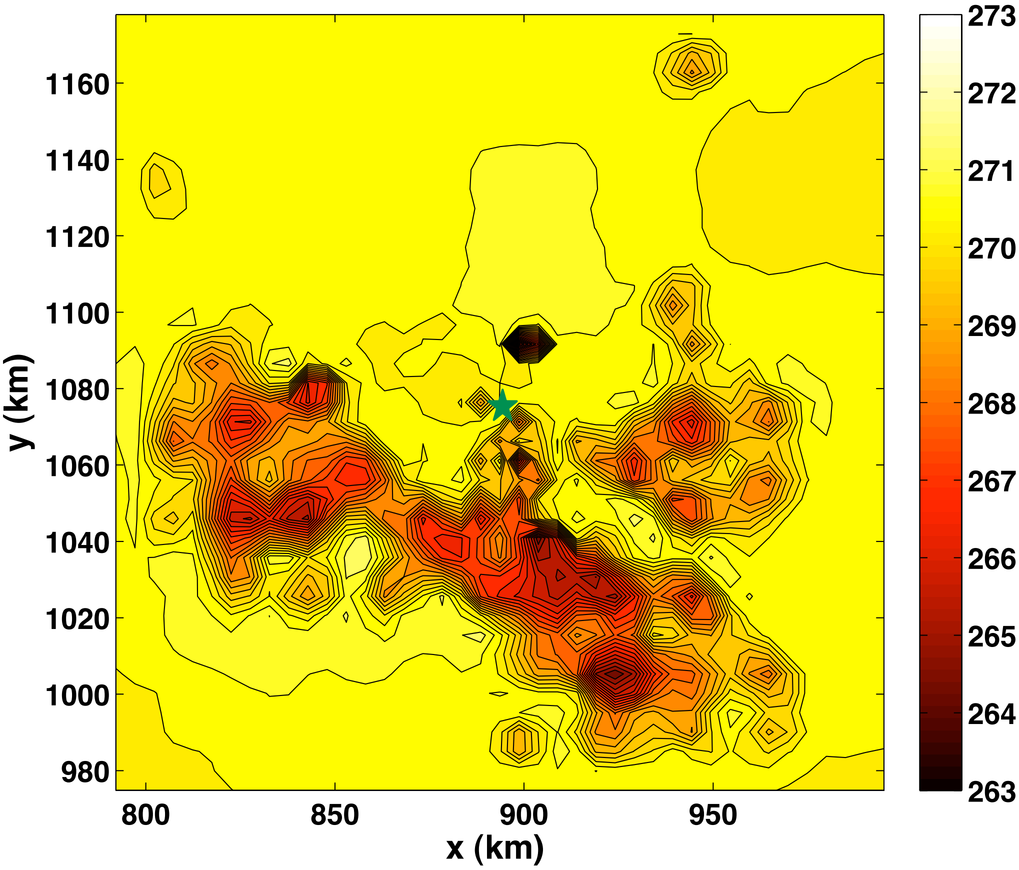

Figure 6.10: Temperature (K) at the ice base obtained with steady-state isotropic simulation. The star indicates the location of the Dome Fuji ice core drilling site.

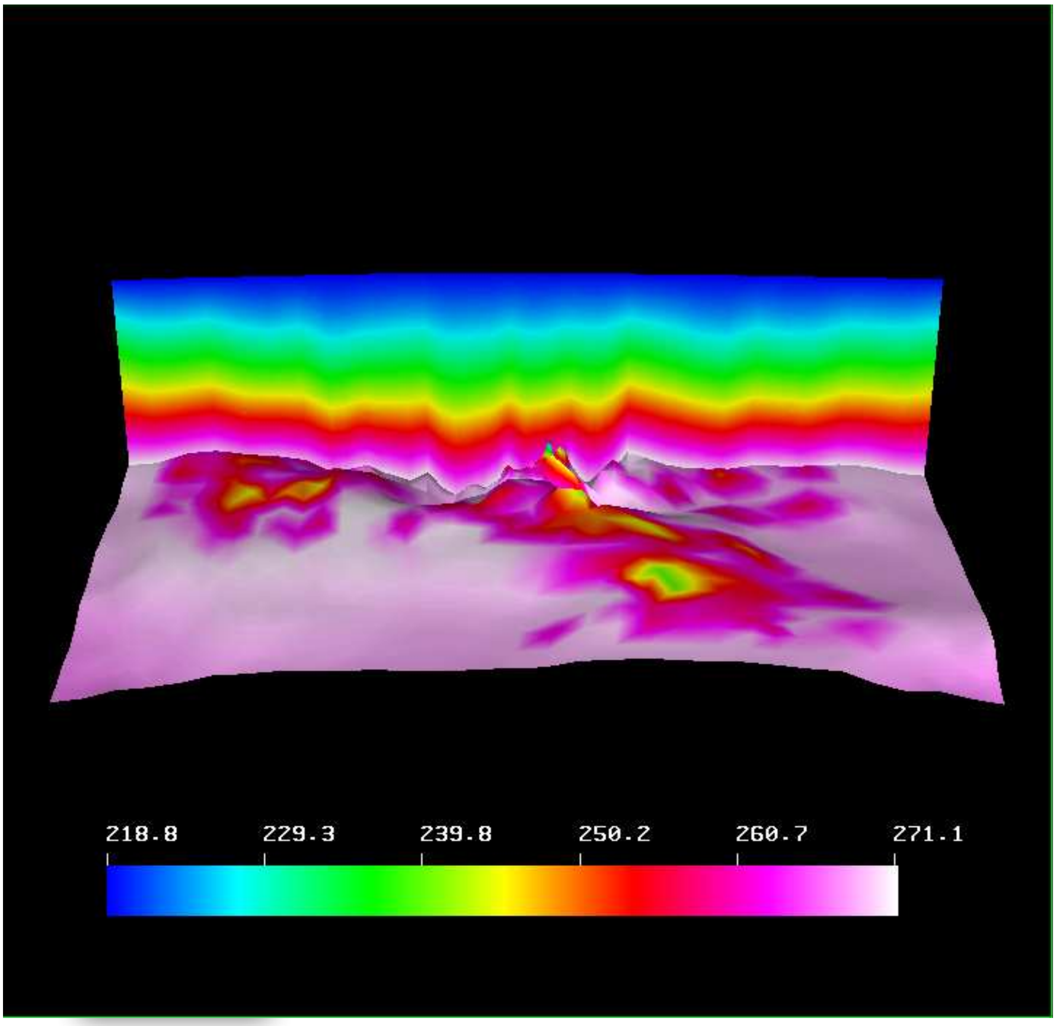

Figure 6.11: Vertical cross-section of the temperature (K) obtained with steady-state isotropic simulation. For the visualization clarity, the bedrock elevation is exaggerated by a factor 20.

6.7.3 Modeling of the age

The solution of the age obtained from a steady-state solution of the velocity field is shown in Fig. 6.12. Here the results are surprising. By comparison with the ice thickness (Fig. 6.4), we observe that the distribution of old ice does not correspond to the locations where it is thick. Intuitively, it is common to think that high values for the age would occur where the ice is thick, but the model depicts an opposite trend: old ice where the ice is thinner. This result is due to the melting conditions at the bedrock. Indeed, the ice being at the melting point, it tends to melt away leaving younger ice whereas where the ice is frozen to the bedrock, old ice can be accumulated there (Fig. 6.13). The model somehow reproduces an observation that has been done for the Dome Fuji ice core, where the ice has been measured to be surprisingly younger than expected ($\sim$ 720-750 ka). The Dome Fuji ice core has been drilled in a location where the basal ice is at the melting condition. The model clearly explains why the ice is younger in those particularly deep locations. In general, we observe that the high values of the age are located on the bedrock ridges whereas younger ice is located in the deep valleys. However, although the computed value for the basal age at the borehole is somewhat close to the measurements, the steady-state assumption used to obtain the age solution is not realistic as the age solution is obviously time dependent (the geothermal heat flux has been tuned to obtain the right basal age at the borehole). Consequently, although the correctness of the absolute values of the age is not guaranteed, its overall distribution inside the domain should be accurate and reflects the general distribution. Therefore, those results are important and in the perspective of future ice core drilling at the vicinity of Dome Fuji, the model provides possible locations for a new borehole.

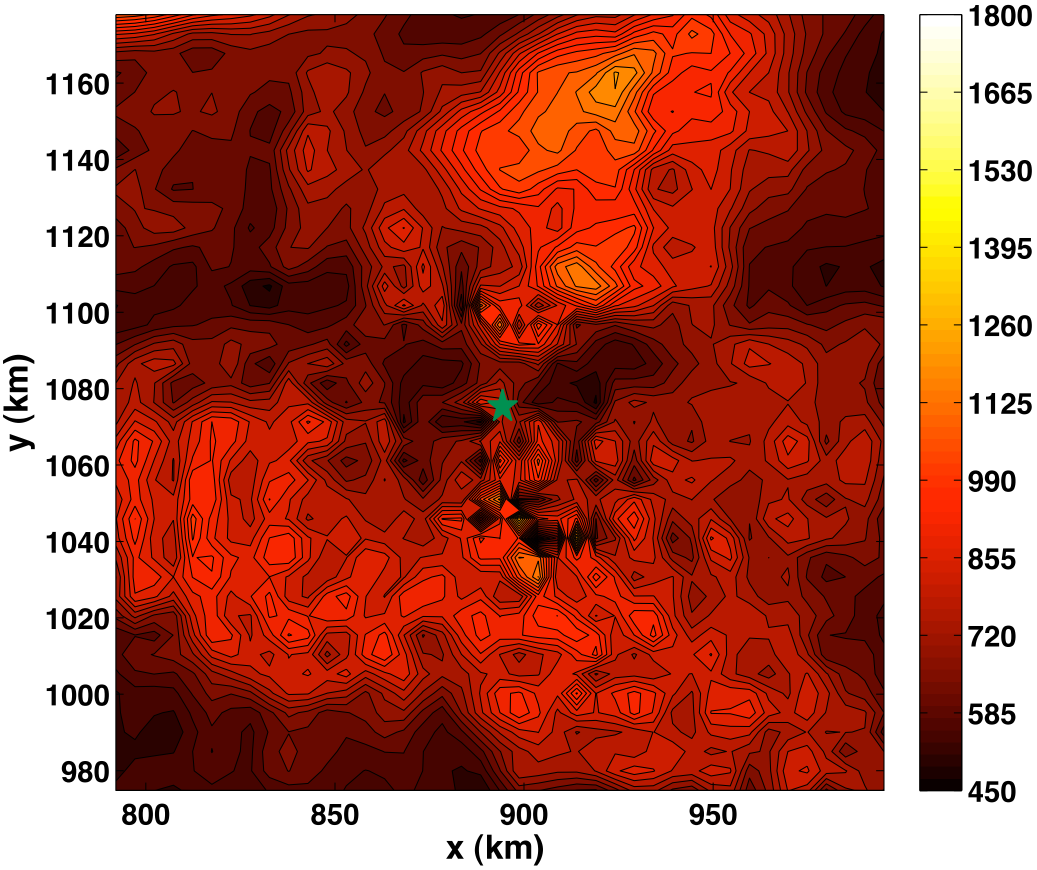

Figure 6.12: Age (ka) at the ice base obtained with steady-state isotropic simulation. The star indicates the location of the Dome Fuji ice core drilling site.

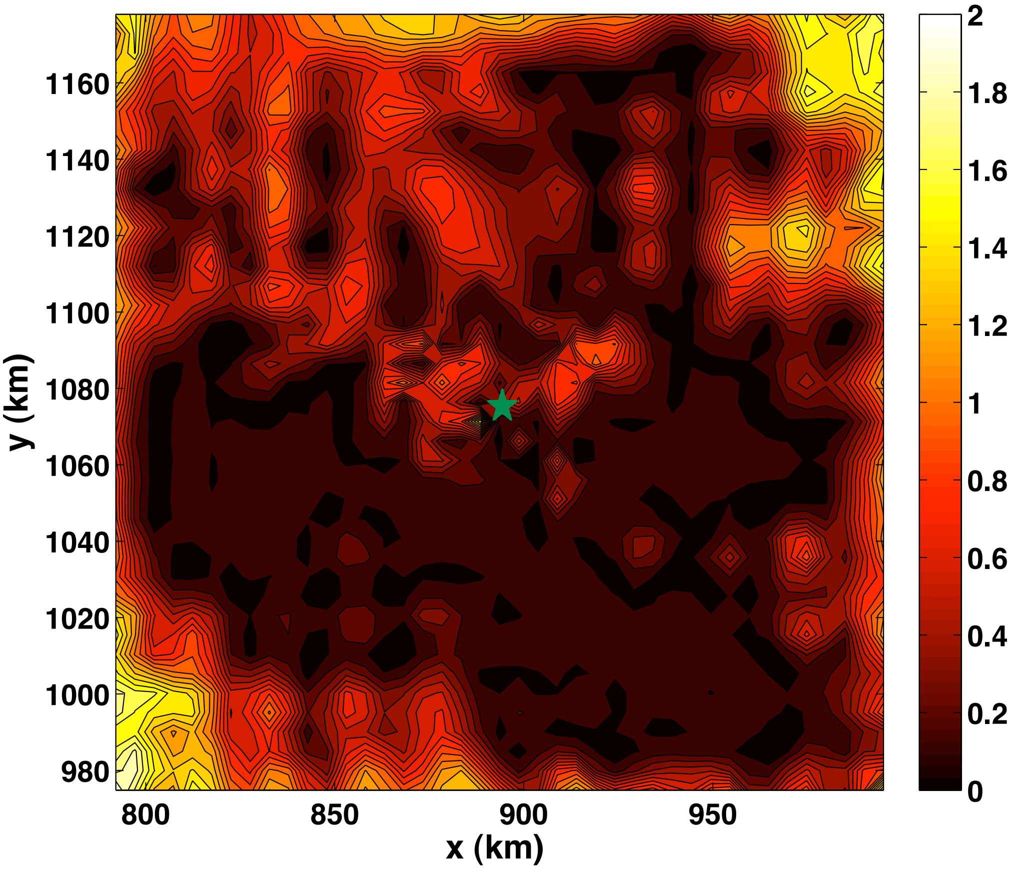

Figure 6.13: Outflow velocity due to melting (mm a^{-1}) at the ice base obtained with steady-state isotropic simulation. The star indicates the location of the Dome Fuji ice core drilling site.

6.8 Steady-state anisotropic simulation

6.8.1 Anisotropic velocities and temperature

Fig. 6.14 shows the anisotropic velocities computed by coupling the flow to the fabric evolution equation. In comparison to the isotropic velocities (Fig. 6.6), we observe that velocity field is elongated and noticeably faster in areas away of the dome, closer to the domain lateral boundaries. This is due to the development of a slight favorably oriented fabric in those regions where ice deforms mainly by shearing which results in faster velocities as the ice is deformed more easily.

For the observation of the velocities at the dome, Fig. 6.15 shows the comparison of the velocity vectors obtained with the isotropic and anisotropic simulations on a 60 x 60 km area at the center of the computational domain. We can observe slight differences between the absolute isotropic and anisotropic velocities as the resulting flow from the dome is slower in the case of the anisotropic simulation (regime of deformation by compression where fabrics tend to develop to a vertical single maximum). The most important observation concerns however the interaction between the flow at the surface and the bedrock topography. As mentioned previously, at the location of the dome, the bedrock topography is characterized by a deep valley formation oriented East-West in our domain and Fig. 6.15 allows to observe in more details the relation between the flow at the surface and this topographical structure. The results show that the flow at the surface is clearly driven by the topography at the bed. The orientation East-West of the flow coincides with the orientation of the valley and the flow velocity is also dependent on the constrains being exerted by the bedrock topography on the ice to flow. For this reason, the velocity is higher when the ice flows above the valleys and slower when the ice flows above the ridges. This observation is important because it highlights the benefit of using the full-Stokes equation in order to resolve all stress components, while ignoring or establishing assumptions to simplify the solution of the dynamics would therefore not provide a mean of understanding the relation between bedrock topography and velocities at the surface. Consequently, this model also shows the consequence of the assumptions made when the shallow-ice approximation is used to model ice dynamics by only computing two components of stress (parallel to the bedrock), which are only dependent on the surface topography. Such assumption does not allow to take into consideration the interaction between bedrock topography and ice flow that are also important elsewhere than ice sheet domes, particularly for the modeling of ice streams.

In terms of absolute values, the differences between isotropy and anisotropy are better assessed by the observation of velocities at the borehole (Fig. 6.16). The difference are larger and more evident for v_x where the ice is noticeably faster in the case of isotropy.

For the anisotropic case, the flow being dependent on the fabric, the model shows that the ice flow is slower. Note again that the isotropic and anisotropic vertical velocities at the surface are in good agreement with the measured surface accumulation, the anisotropy case being closer to observations.

Fig. 6.17 shows the comparison of the vertical velocity at the surface for isotropy and anisotropy at the dome. As observed in Fig. 6.16, the results for the anisotropic model are better in agreement with the observed surface accumulation at the Dome Fuji station whereas the isotropic simulation overestimates the surface accumulation. Here the contribution of the anisotropy is clearly demonstrated because of the trend of a single vertical maximum development for the fabric which contributes to harden the ice for vertical compression. The values of the anisotropic vertical velocity are nevertheless slightly higher than observations, this is due to the development of a weaker vertical fabric obtained by the model in comparison to the in-situ fabric (observed with the Dome Fuji ice core) as described in the next section.

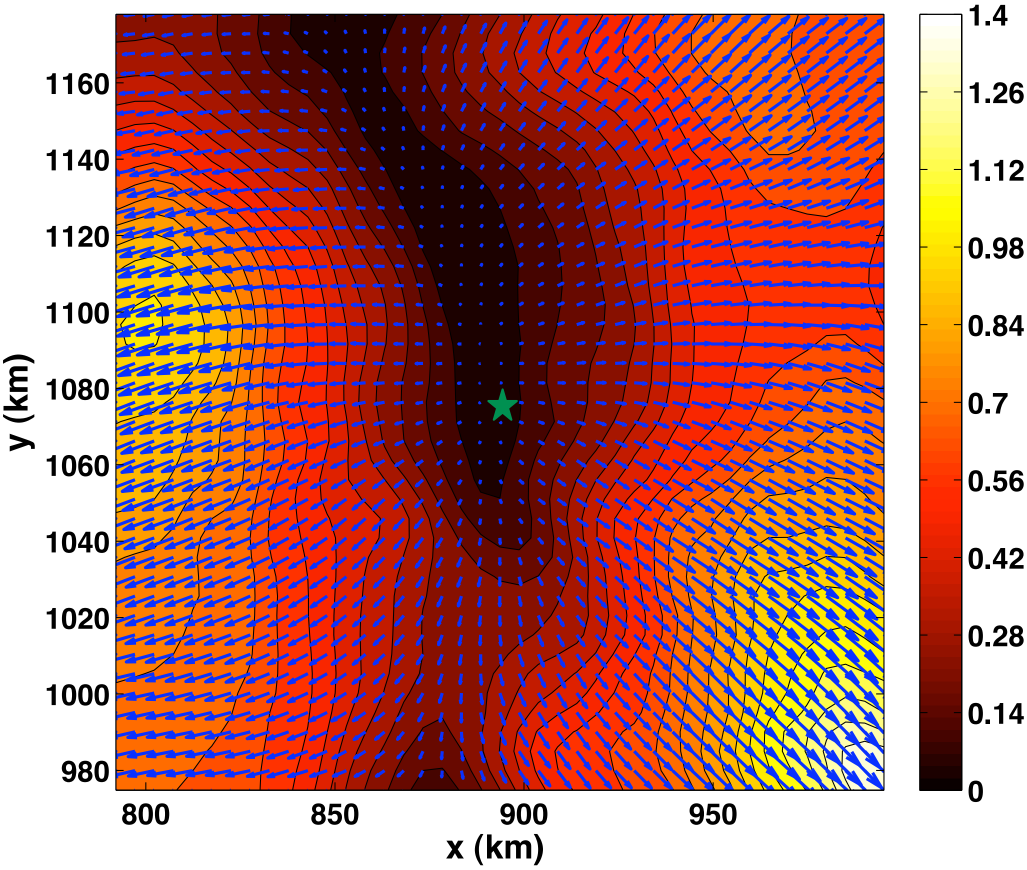

Figure 6.14: Surface horizontal velocities ($\mathrm{m\,a^{-1}}$) and associated vectors obtained with steady-state anisotropic simulation. The star indicates the location of the Dome Fuji ice core drilling site.

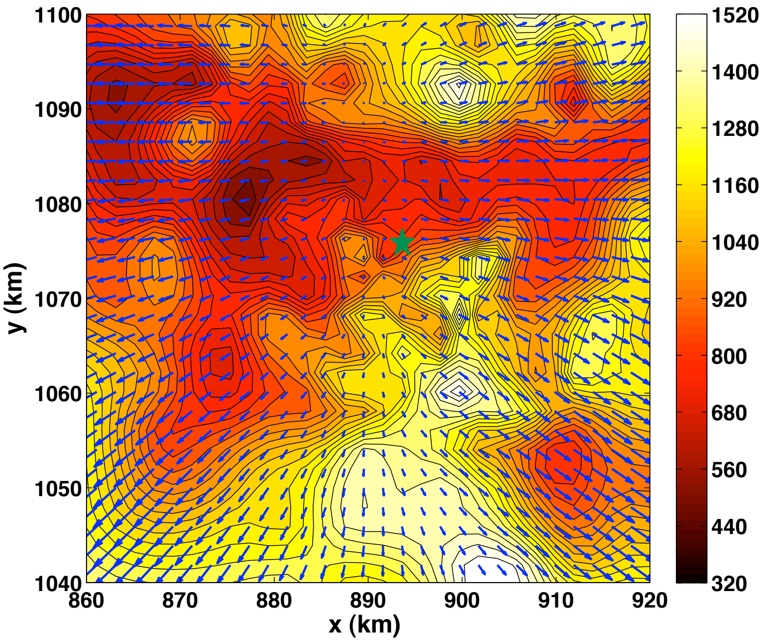

(a) Isotropic

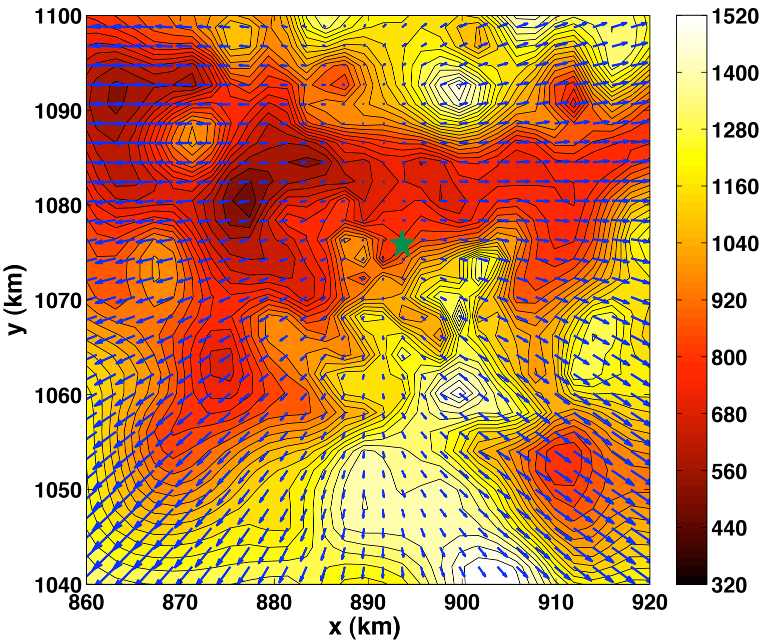

(b) Anisotropic

Figure 6.15: Bedrock elevation (m) and surface horizontal velocity vectors at the vicinity of the dome. The star indicates the location of the Dome Fuji ice core drilling site.

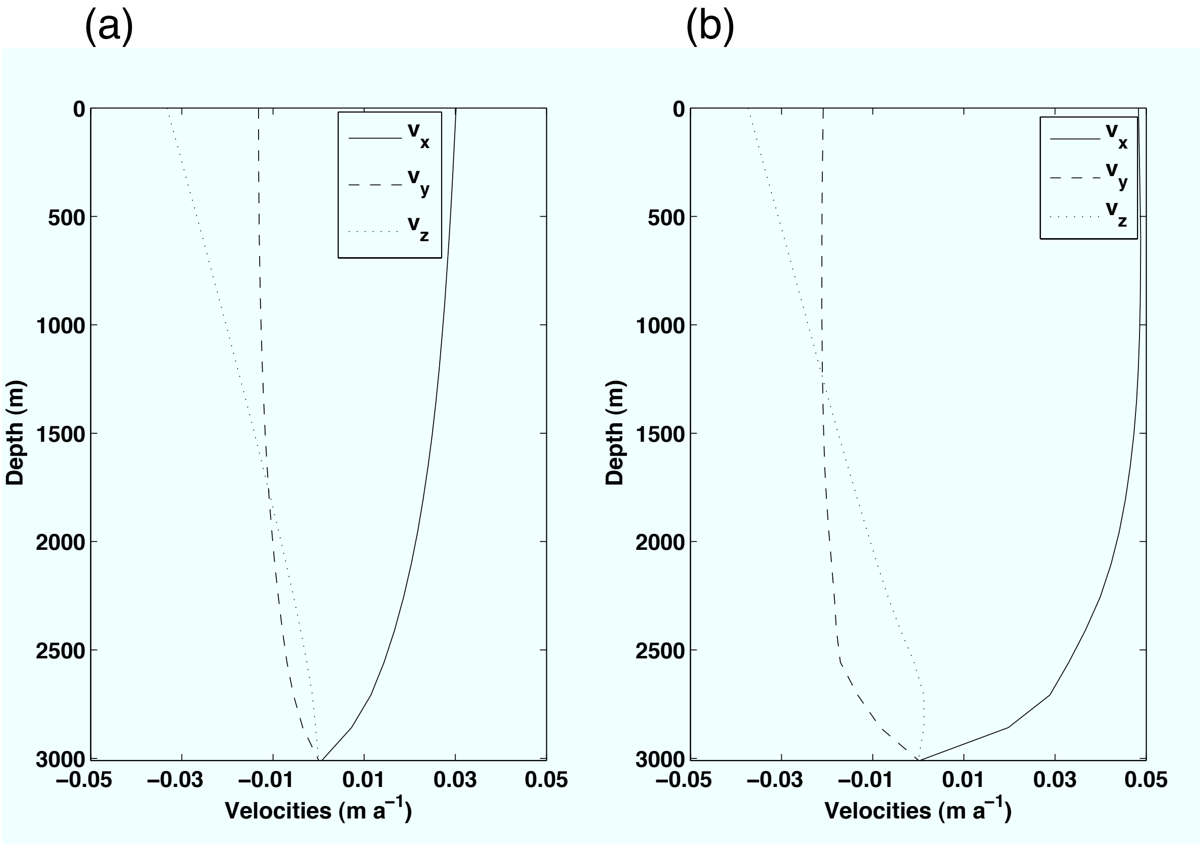

Figure 6.16: Computed anisotropic (a) and isotropic (b) velocities at the borehole.

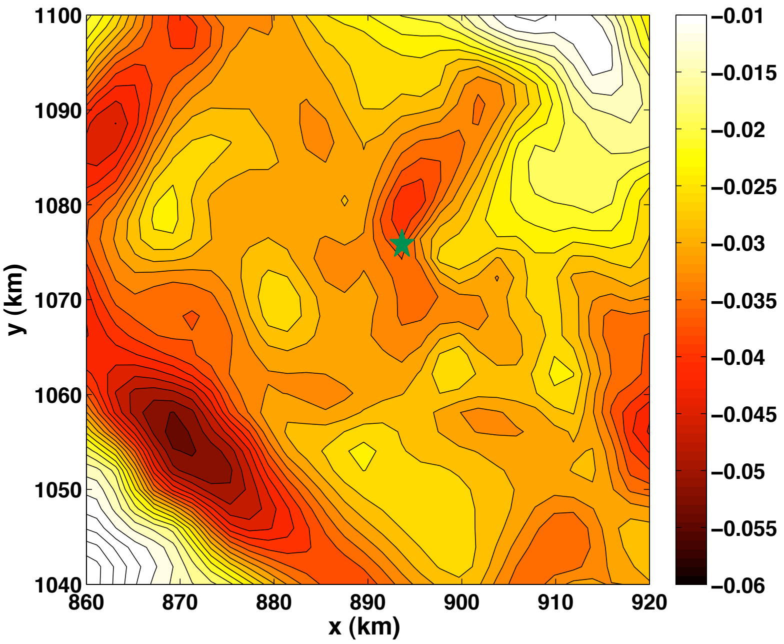

(a) Isotropic

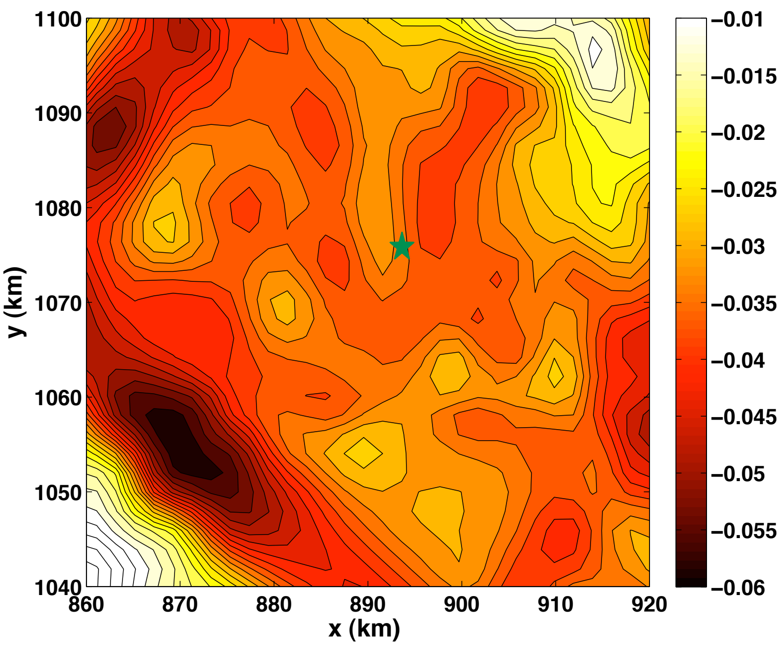

(b) Anisotropic

Figure 6.17: Surface vertical velocities ($\mathrm{m\,a^{-1}}$) at the vicinity of the dome. The star indicates the location of the Dome Fuji ice core drilling site.

The computed basal temperature is shown in Fig. 6.18. The distribution is somewhat similar to the results obtained with the isotropic flow law with the good agreement between temperature distribution and ice thickness. We observe however larger areas of cold ice surrounding the ridges due to the smaller deformations rates associated with the anisotropy which results in a smaller strain heating in comparison to the isotropic simulation. The same observation can be made at the dome (Fig. 6.19) where we can also better observe the melting conditions at the bed rock.

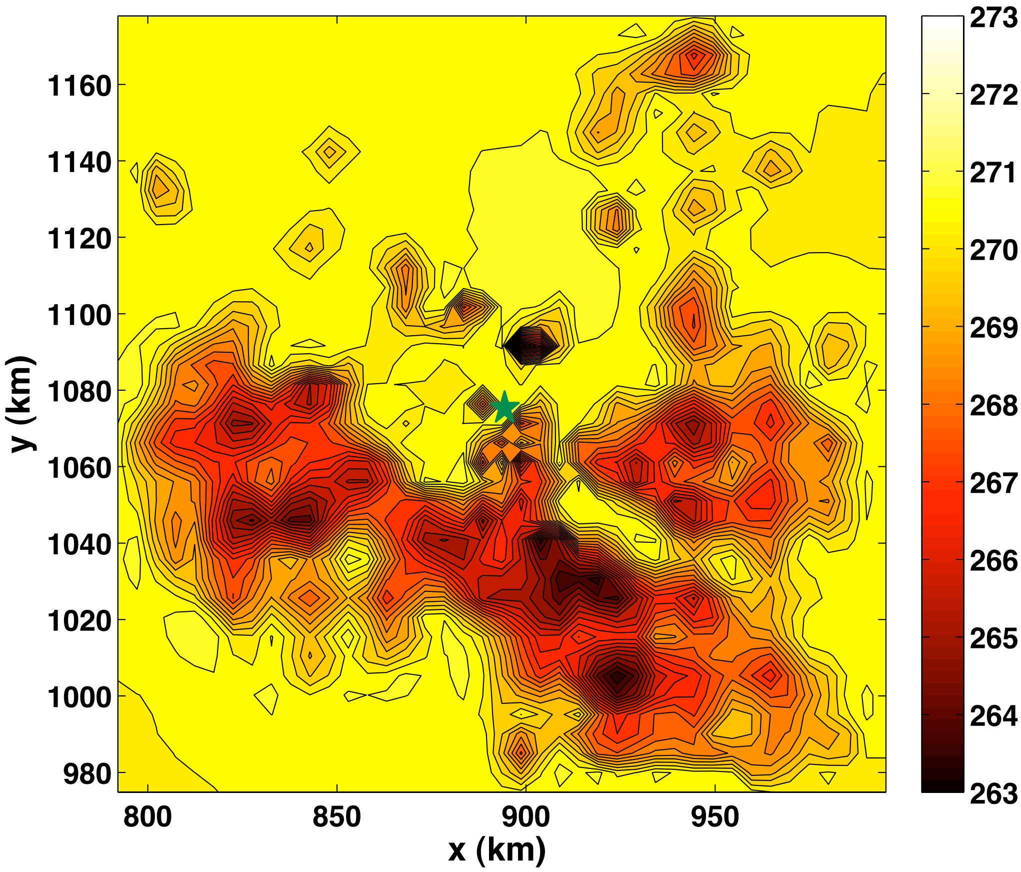

Figure 6.18: Temperature (K) at the ice base obtained with steady-state anisotropic simulation. The star indicates the location of the Dome Fuji ice core drilling site.

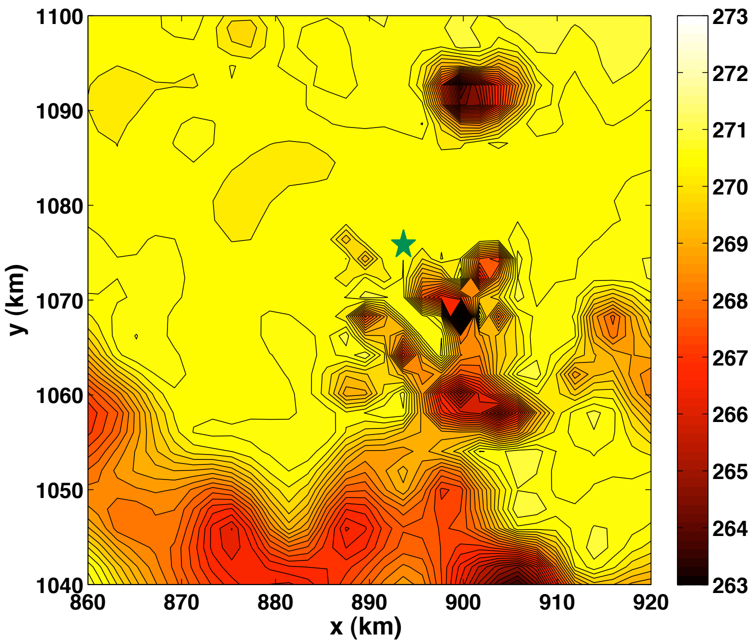

(a) Isotropic

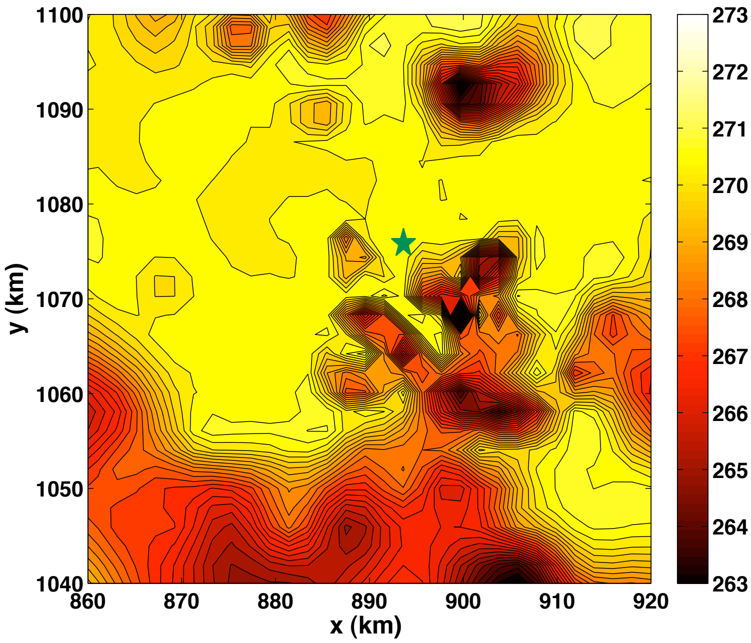

(b) Anisotropic

Figure 6.19: Basal temperature (K) at the vicinity of the dome. The star indicates the location of the Dome Fuji ice core drilling site.

6.8.2 Fabric evolution

The fabric evolution was computed until the flow and fabric solutions have reached a steady-state. The three components of the diagonal of the second-order tensor are shown in Figs 6.20-6.21-6.22 (results for the other components of the tensor $\mathsf{a}^{(2)}$ are presented in Appendix J). In a dome, the principal regime of deformation is the vertical normal deformation. For this reason, a single vertical maximum fabric should form (c-axis rotates towards the axis of compression), which translates in decreasing values for $a_{11}^{(2)}$ and $a_{22}^{(2)}$ towards 0, and increasing values for $a_{33}^{(2)}$ towards 1. The model predicts the evolution of the fabric to a vertical single maximum. We observe decreasing values for $a_{11}^{(2)}$ and $a_{22}^{(2)}$ at the dome. However it seems that the evolution of $a_{22}^{(2)}$ is slower than $a_{11}^{(2)}$, this is due to the principal flow being oriented towards the x-direction The values of $a_{33}^{(2)}$ show an increasing trend towards the dome, reaching valued of 0.8 in certain locations. We do however notice that at the domain center, the evolution of the fabric is slow with values of the second-order tensor being still close to the isotropic fabric. This slow evolution can be explained by the very slow dynamics acting on this area of the domain. By observation of the vertical distribution of $a_{33}^{(2)}$ for a cross-section at the domain center (Fig. 6.23), we notice the layer of high values (single maximum fabric) is somewhat not located at the bedrock (where the fabric is less concentrated), suggesting that values of the deformation rates are not high enough for the development of a single maximum fabric at the ice base. Fig. 6.24a shows the vertical profile at the location of the borehole of the three computed components of the diagonal of the second-order tensor. The evolution trend is in good agreement with the observed Dome Fuji ice core (Miyamoto, A.; personal communication, Japanese Society of Snow and Ice Annual Meeting, Toyama, Japan, 2007). It is particularly interesting to note that the sharp increase of $a_{33}^{(2)}$ values and decrease of $a_{11}^{(2)}$ and $a_{22}^{(2)}$ at around 2700-2800 m depth (trend to the formation of the single maximum fabric) is also observed in the ice core. However, the data have shown a stronger concentrated fabric than the model is able to reproduce. This difference can be explained by the occurrence of dome migration processes which are not taken into account in the model. The Dome Fuji ice core borehole is not exactly located at the dome but it exhibits strong maximum fabrics which are potentially the consequence of the dome migration. Another explanation can be found in considering that the dome has totally disappeared during the glaciological cycles. The disappearance of the dome can trigger the transition to a flow regime of deformation mainly by shearing, possibly resulting in the rapid development of concentrated fabrics. At the ice base, the observed ice core fabric contains large crystals without preferential orientations. Such fabric is not reproduced by the model as recrystallization processes are not taken into account (the model shows that the fabric is somewhat less concentrated but the reasons of this trend are only related to the induced deformations). Due to the temperature conditions at the ice base, migration recrystallization can occur which can explain the observed fabrics there.

Fig. 6.24b shows the computed deformation rates at the borehole. We observe that the main process of deformation is the vertical strain with larger extension towards the x-direction than in the y-direction. This also explains the slow decrease of $a_{22}^{(2)}$ in comparison to $a_{11}^{(2)}$ (Fig. 6.24a). Another remarkable observation is the occurrence of shear deformations parallel to the bedrock at the ice base. The pronounced topography can explain this shearing which is also responsible of the decreasing values of $a_{33}^{(2)}$ at the ice base. We remark therefore that this observation contradicts the assumptions generally made in order to date the bottom part of ice cores extracted from domes.

Fig. 6.25 shows the result for the two components $a_{11}^{(2)}$ and $a_{33}^{(2)}$ at the location of the dome. Although we observe areas where the fabric has achieved to develop towards pronounced singe maximum configurations ($a_{33}^{(2)} \sim 0.6-0.7$), the distribution is somewhat surprising. We observe variations between lower and higher values of the second-order orientation tensor which are physically difficult to justify so numerical artifacts can also be considered as one possible reason for these variations.

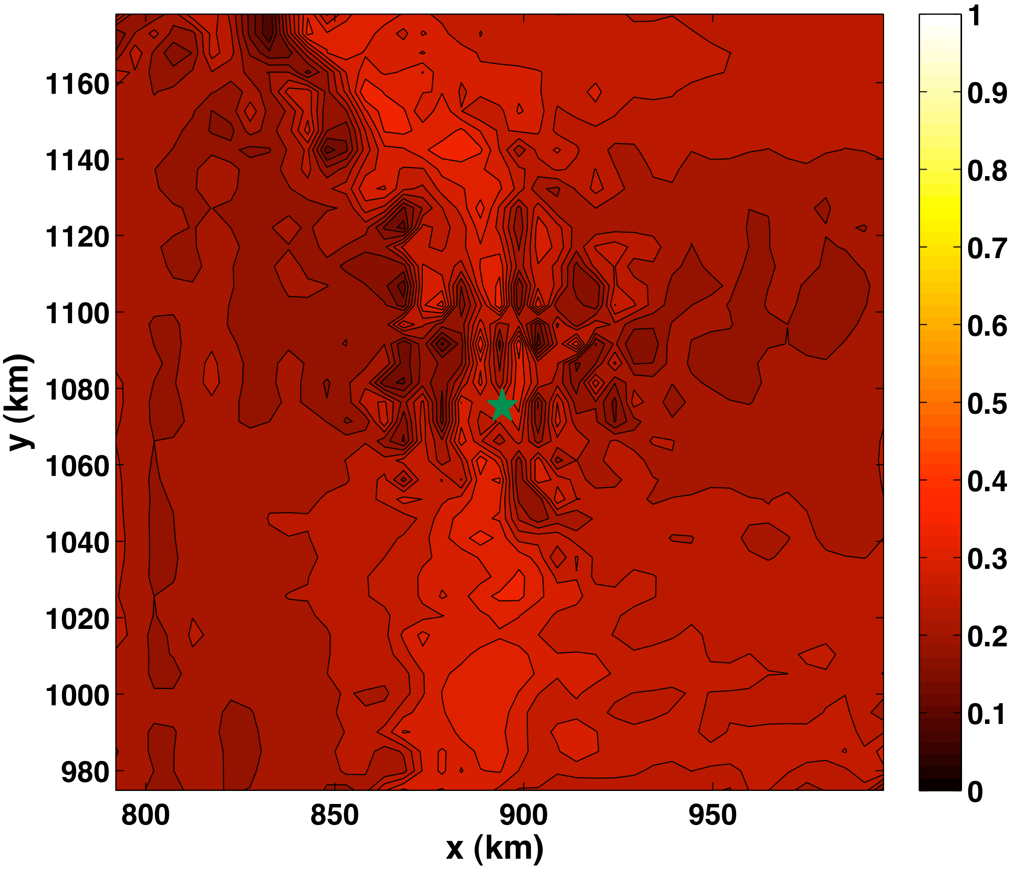

Figure 6.20: Distribution of $a_{11}^{(2)}$ at the ice base obtained with steady-state anisotropic simulation. The star indicates the location of the Dome Fuji ice core drilling site.

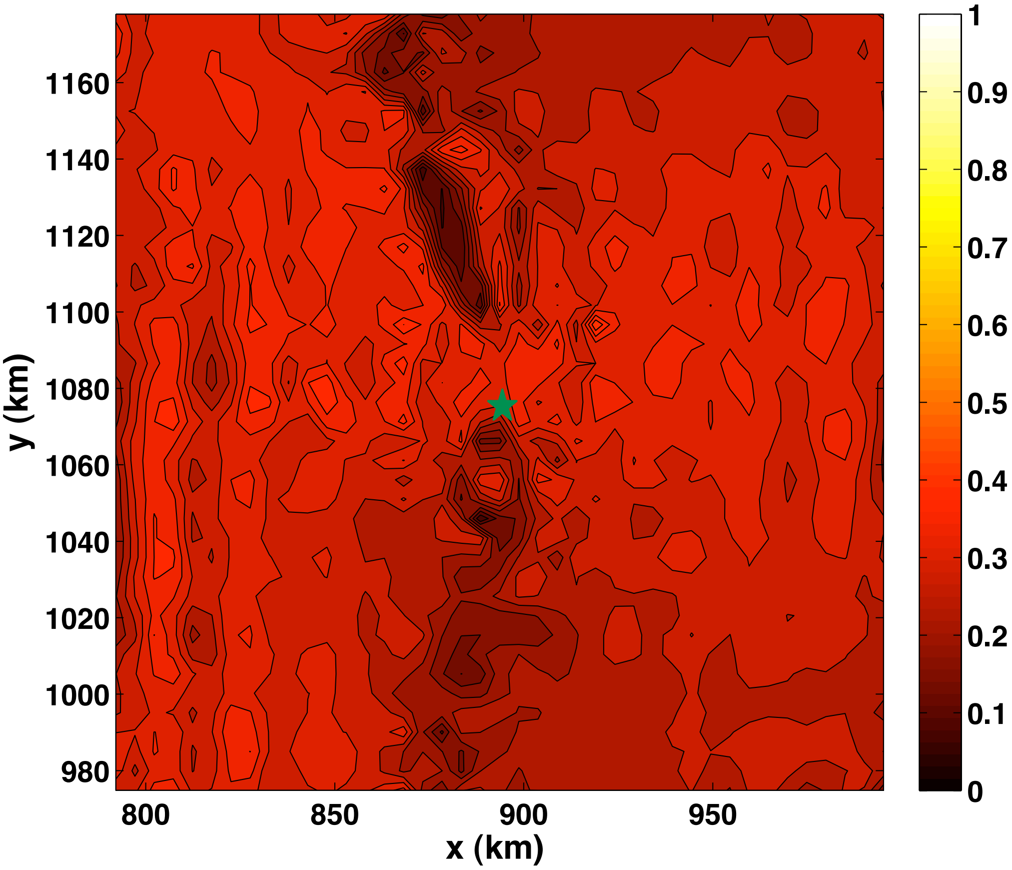

Figure 6.21: Distribution of $a_{22}^{(2)}$ at the ice base obtained with steady-state anisotropic simulation. The star indicates the location of the Dome Fuji ice core drilling site.

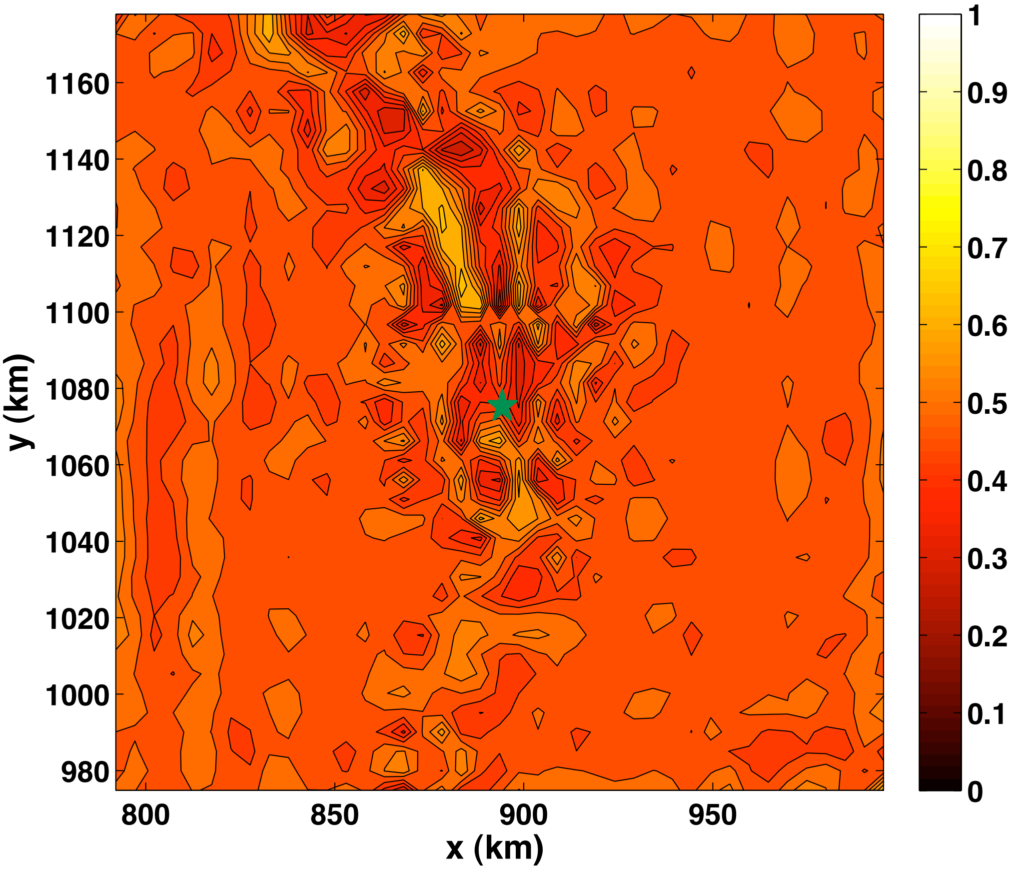

Figure 6.22: Distribution of $a_{33}^{(2)}$ at the ice base obtained with steady-state anisotropic simulation. The star indicates the location of the Dome Fuji ice core drilling site.

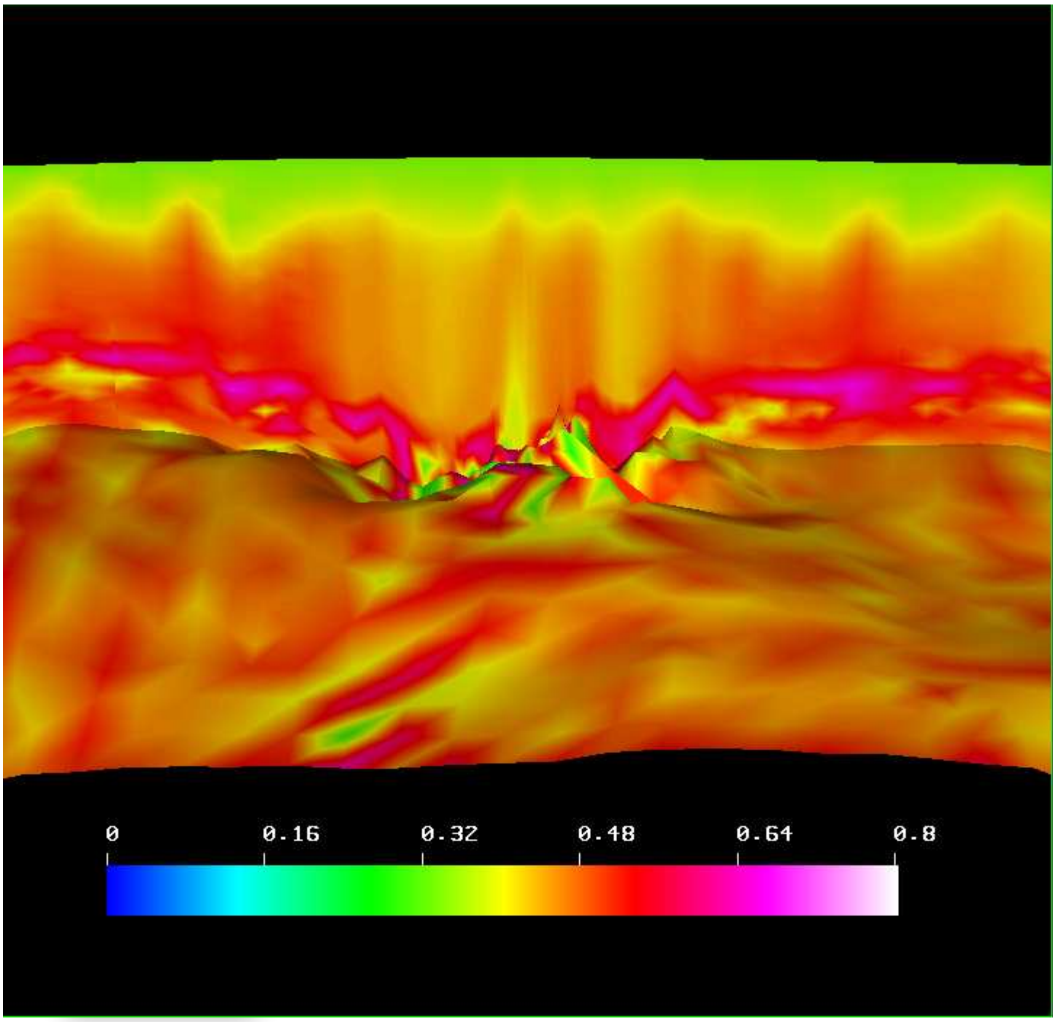

Figure 6.23: Vertical cross-section of $a^{(2)}_{33}$ obtained with steady-state anisotropic simulation. For the visualization clarity, the bedrock elevation is exaggerated by a factor 20.

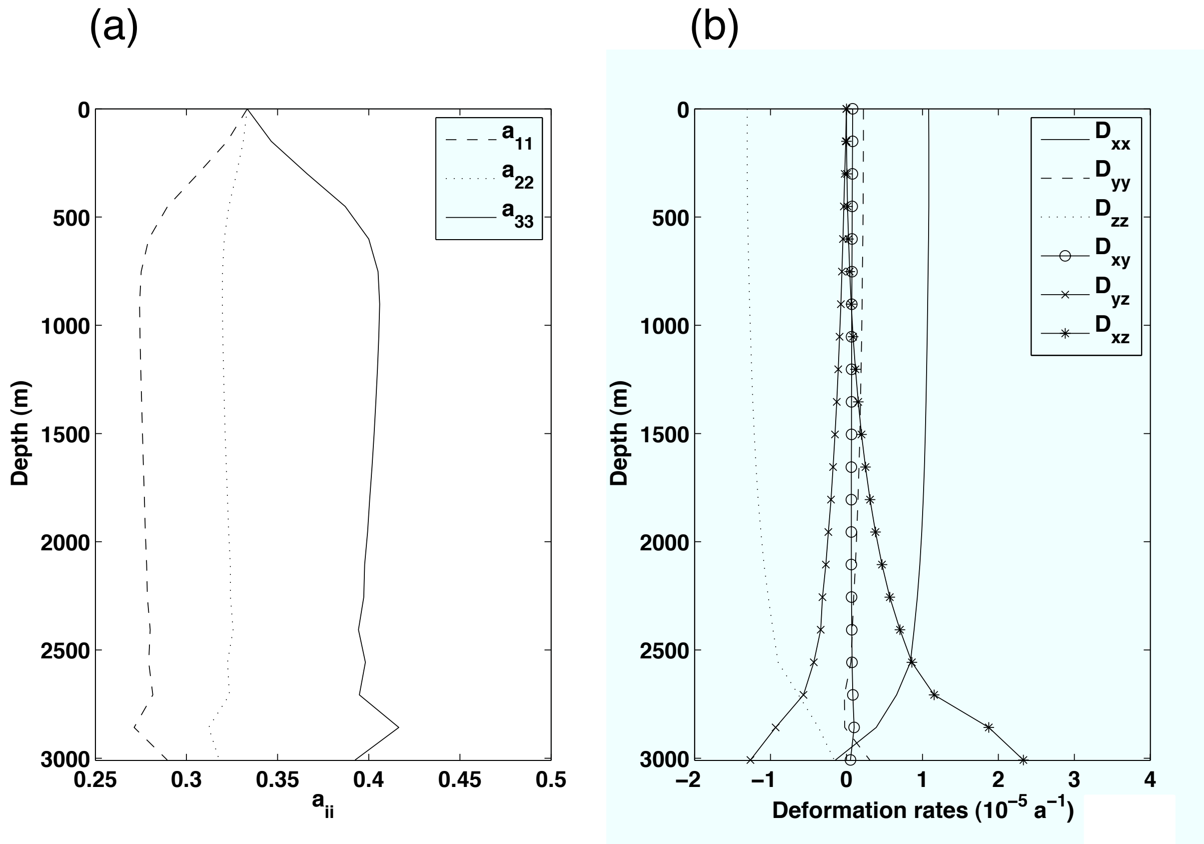

Figure 6.24: Computed components of the second-order tensor $\mathsf{a}^{(2)}$(a) and deformation rates (b) at the borehole.

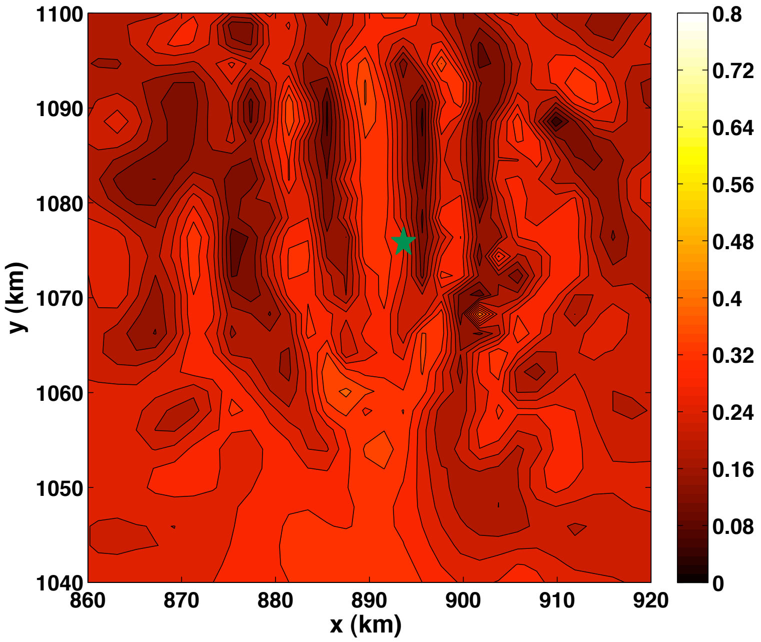

(a) $a_{11}^{(2)}$

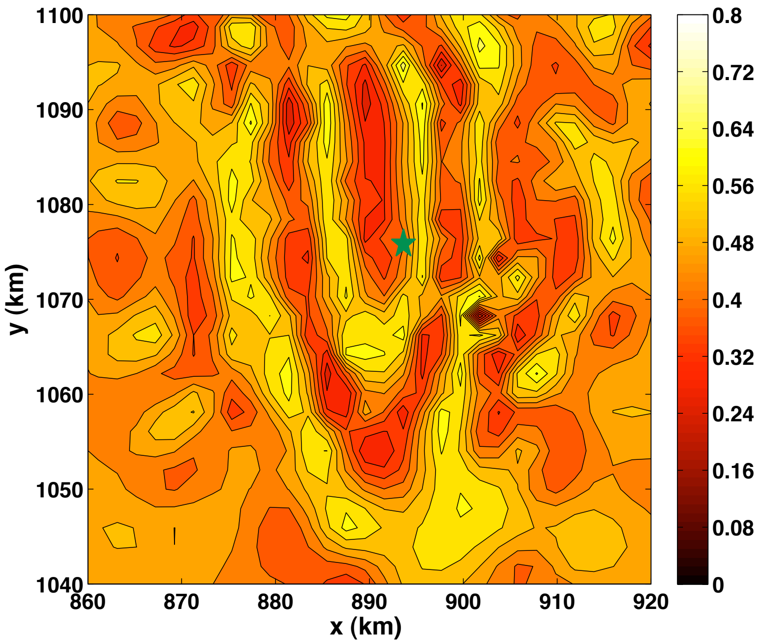

(b) $a_{33}^{(2)}$

Figure 6.25: Basal distribution of $a_{11}^{(2)}$ and $a_{33}^{(2)}$ at the vicinity of the dome. The star indicates the location of the Dome Fuji ice core drilling site.

6.8.3 Anisotropic age

The anisotropic flow solution is used to compute the anisotropic dependent age shown in Fig. 6.26. We have seen that the trend of the fabric evolution is the formation of concentrated fabrics which results in slower ice flow in comparison to isotropic conditions. The computed anisotropic age reflects this trend. In comparison to isotropic conditions (Fig. 6.12), we observe higher absolute values, the ice is therefore older due to the anisotropy. We remark that similarly to the isotropic results, due to the melting conditions at the deepest part of the domain, the old ice is located at the bedrock ridges.

Fig. 6.27 shows the comparison between isotropic and anisotropic ages at the ice core borehole. Here again, the trend of the fabric development towards a single maximum contributes to the higher values of age in comparison to the isotropic age. At the bottom part of the borehole, the model predicts an age of 900 ka, which is older in comparison to the observed age ($\sim$ 720-750 ka) and to the isotropic simulation ($\sim$ 720 ka). Note that, due to the migration recrystallization processes which produce the particular observed fabric at the borehole bottom (large crystals without preferred orientation), we expect that such fabrics have an isotropic mechanical behavior. Therefore, the measured age is likely obtained by isotropic deformation of the remaining ice at the ice core bottom.

Fig. 6.28 and Fig. 6.29 show the comparison between isotropy and anisotropy for the age and melting at the bedrock and at the dome. Here again the distribution of the age follows the variation of the fabric where older age is obtained in comparison to the isotropic age where the fabric is more vertically concentrated. Therefore, due to the anisotropy, old ice is expected to be found on the high ridge which can be observed on the southern part of the dome vicinity. Finally, similarly to the isotropic simulation, the absolute age values are not reliable (due to the steady-state simulation) but the distribution should reflect the reality.

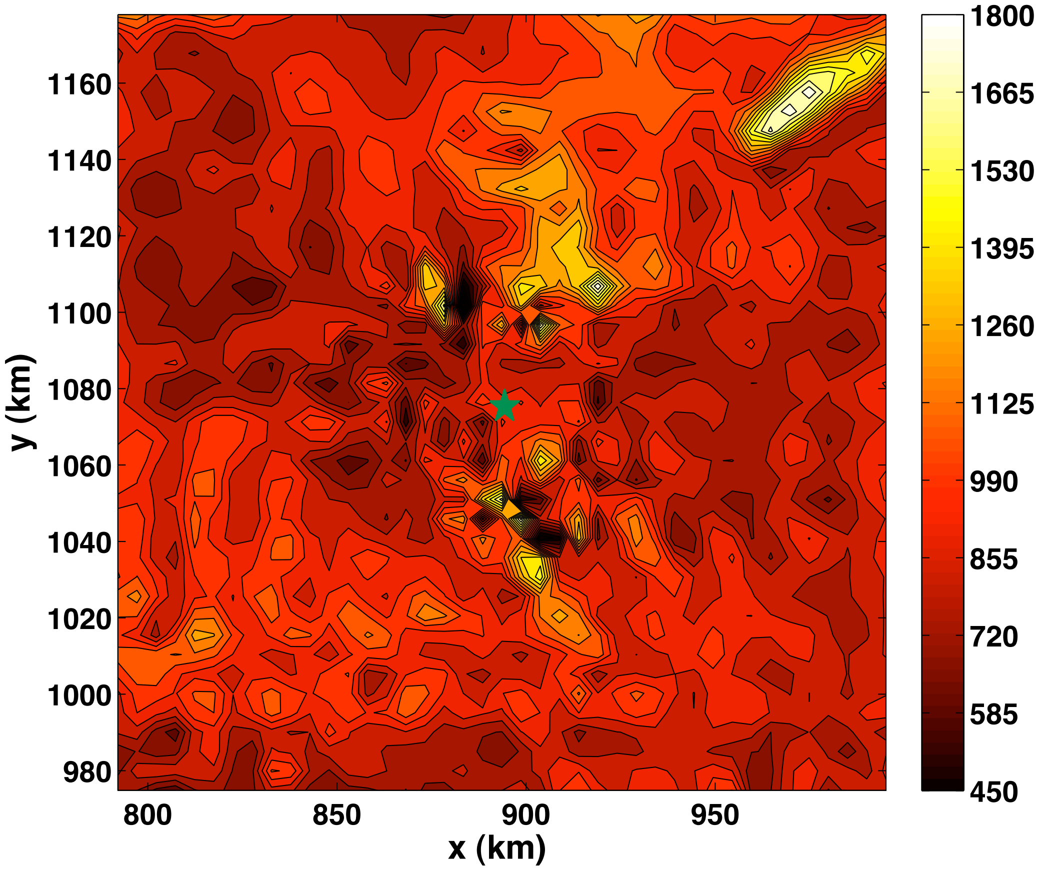

Figure 6.26: Age (ka) at the ice base obtained with steady-state anisotropic simulation. The star indicates the location of the Dome Fuji ice core drilling site.

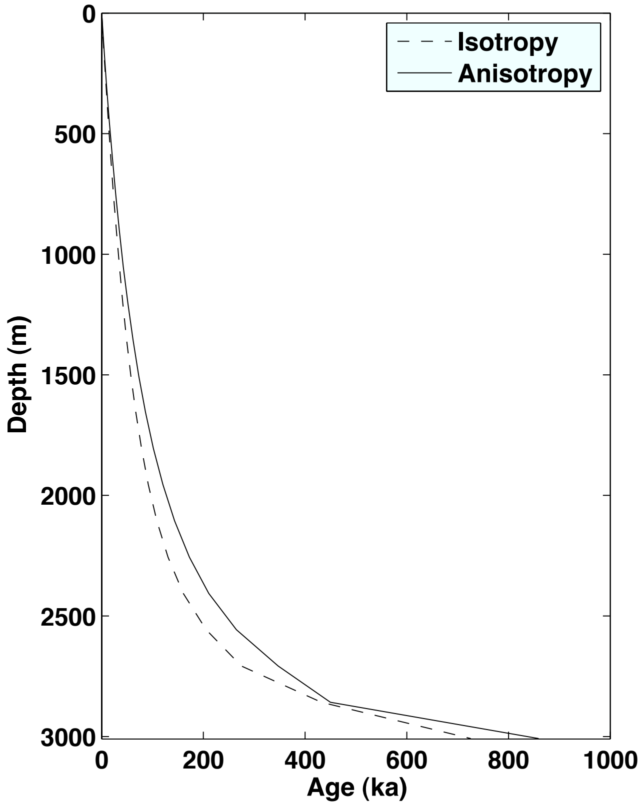

Figure 6.27: Comparison between anisotropic and isotropic age at the borehole.

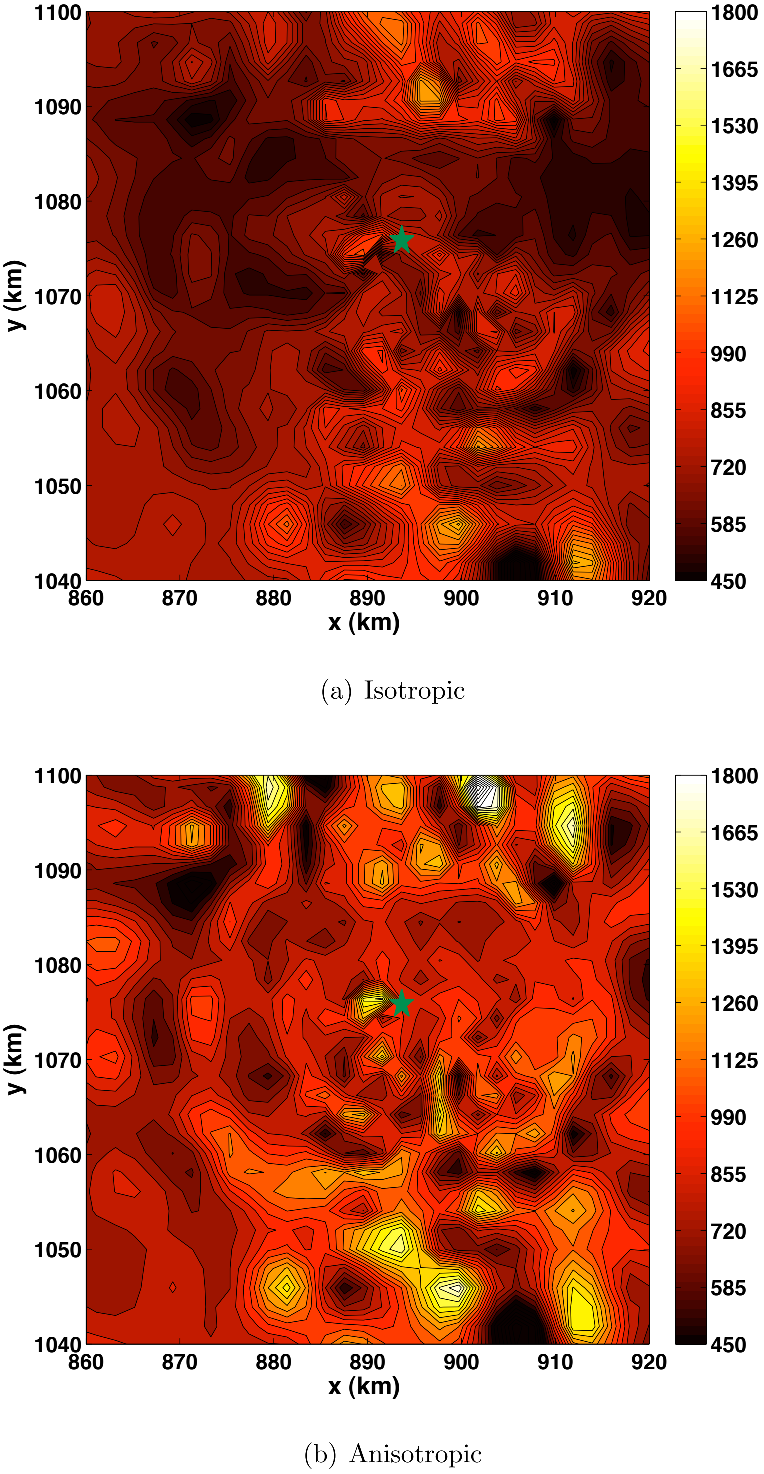

(a) Isotropic

(b) Anisotropic

Figure 6.28: Basal age (ka) at the vicinity of the dome. The star indicates the location of the Dome Fuji ice core drilling site.

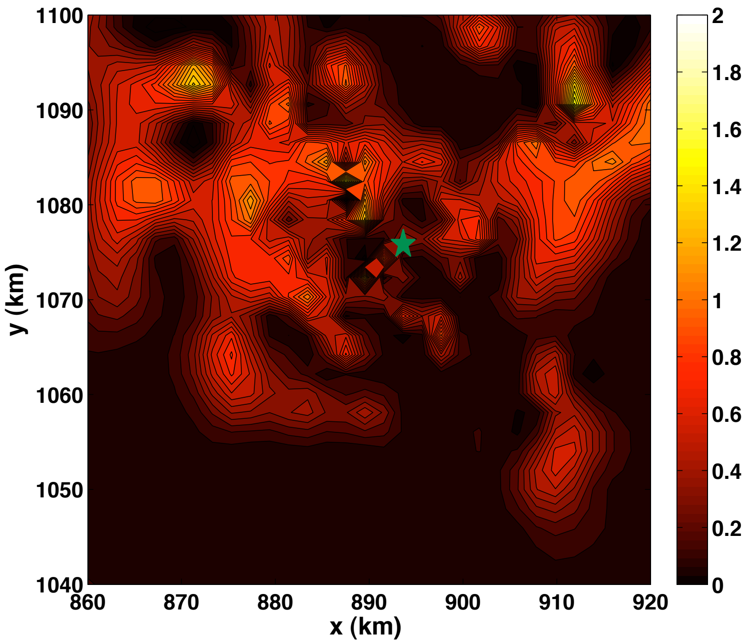

(a) Isotropic

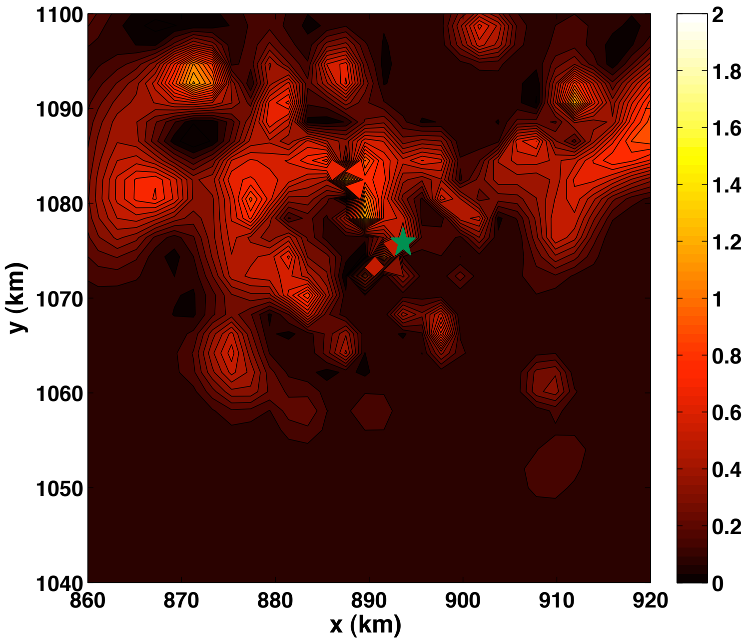

(b) Anisotropic

Figure 6.29: Basal outflow velocity due to melting ($\mathrm{mm\,a^{-1}}$) at the vicinity of the dome. The star indicates the location of the Dome Fuji ice core drilling site.

6.9 Conclusion

In this chapter we have developed a full-Stokes finite-element model for the vicinity of Dome Fuji that takes into account ice anisotropy and fabric evolution. Two types of simulation have been carried out: steady-state isotropic and steady-state anisotropic. The model has computed the ice dynamics at the Dome Fuji and the distribution of the temperature at the ice base has been determined. With the computed melting conditions, the distribution of the age has been assessed. The resulting computed age has shown surprising results due to the location of old ice where the ice is thinner. The anisotropic simulation has shown the effect of ice anisotropy on ice dynamics (ice flow) and on the age. The model predicts old ice in comparison to isotropic conditions, however the complexity of recrystallization processes at the bottom of the Dome Fuji ice core associated with dome migration/disappearance processes does not permit the exact modeling of the fabric and age at the borehole.

Chapter 7

Conclusion

In this dissertation, we have established the necessary framework for the modeling of ice anisotropy and fabric evolution and its application to large scale modeling at the Dome Fuji.

In Chapter 3, we have presented the CAFFE model, a continuum approach for the modeling of ice anisotropy. The anisotropic flow law is a generalization of the Glen's flow law to anisotropy, where the ice anisotropy is introduced by an enhancement factor function of the polycrystal deformability. The deformability contains all the information of ice crystals orientation and the basal deformation has been assumed to be the principal mechanism of deformation for the monocrystal of ice. The evolution of the anisotropy is implemented by means of the evolution of an orientation mass density. Three processes that enter in the ice fabric evolution has been considered: crystal rotation due to the induced deformation (orientation transition rate), rotation recrystallization (orientation flux) and migration recrystallization (orientation production rate).

In Chapter 4, we have constructed a one-dimension flow model applied to the EDML ice core, Antarctica. This model has been constructed in order to assess the performance and the validity of the CAFFE model. We have shown that the performance of the model are good. We have compared the computed anisotropic horizontal velocities to measurement and found good agreements. In the same time, we have shown the importance of ice anisotropy in comparison to isotropy. We have computed the evolution of the fabric and compared the results to the measured EDML ice core. The model has shown good agreements between the computed and observed fabrics. The girdle fabrics has been well reproduced and their orientation relative to the ice flow could be assessed by the model. Down to the deeper parts of the ice core, the model was not able to reproduce the single vertical maximum fabric obtained at EDML. We have shown that the reason of the differences were due to the disregard of recrystallization processes in the model. We have also showed that by eliminating the shearing in the fabric evolution equation, the model was able to produce as single vertical maximum fabric. This demonstrated clearly that the shearing is the factor contributing to the decay of the fabric computed by the model. Lastly, the independence of the results to the employed numerical method and the stability of the anisotropic flow law have been assessed.

In Chapter 5, we have developed a formulation of the CAFFE model that can be applied in a finite-element code for the purpose of large scale modeling. We have adopted orientation tensors for the description of the fabric and formulate the polycrystal deformability equation in terms of second and fourth-order tensors. The same procedure has then been applied for the fabric evolution equation, expressed as the evolution of the second-order orientation tensor. The components of the fourth-order tensor were computed by using a closure approximation function, IBOF.

In Chapter 6, we have established the general field equations for the construction of the full-Stokes finite-element model. We have described the numerical methods and the general procedures to obtain solutions. The model has then been applied to the vicinity of Dome Fuji. With the isotropic steady-state simulation, the velocities have ben computed and the general dynamics of the dome has been described. The striking results obtained with this simulation were given by the age. With the computation of the melting velocity due to ice melting at the bedrock, the model has shown that the location of old ice is associated with the location of thinner ice. This surprising results is an important achievement of this study. We have shown that the distribution of old ice does not not follow the general intuition that old ice is located where the ice is thick. In the particular case of Dome Fuji, the ice being at the melting point in large areas at the bedrock where the ice is thick, the values of the age there are surprisingly smaller than expected. Those results confirm the data for the age obtained with the Dome Fuji ice core.

The modeling of the fabric has shown that the general trend of the fabric evolution is the formation of a single vertical maximum fabric. The effects of the fabric on the flow and age have been clearly shown by the model. The model predicts higher values for the age in comparison to the isotropic results. With anisotropy, the ice is therefore older compared to the isotropic age. Combination of ice anisotropy and melting velocities at the bedrock allows the model to be able to provide possible locations for future ice core drilling. This study has therefore a practical impact on future decision concerning ice core drilling at Dome Fuji. At the borehole, fabric computed by the model has shown good agreement for the evolution trend in comparison to the Dome Fuji ice core. However, the Dome Fuji ice core has shown the formation of a stronger single vertical maximum fabric, the same fabric was not obtained with the model. Migration or disappearance of the dome has been proposed as as possible reason for those differences. Also the fabric texture observed at the bottom of the ice core were not reproducible by the model, the disregard of recrystallization processes is a possible explanation for this observation.

In conclusion, we can propose several future directions of research that can be developed to improve the model:

- For the fabric evolution equation, recrystallization processes (particularly migration recrystallization) should be included in the fabric evolution equation in order to better reproduce fabrics formed in warm temperatures. This can been done by expressing those processes with the orientation tensors. Another improvement can be obtained by introducing a six-order orientation tensor for the simulation of crystals rotation. Such tensors would allow to better reproduce measured fabrics, particularly where the ice deforms by shearing.

- A coupling with higher scales ice-sheets models (nested modeling) should provide more accurate boundary conditions. This should also allow for computing the variation of the free surface.

- Further comparisons between modeling and field data should also be carried out. Ice cores can provide important data for future model improvement strategies.

Appendix A

Derivation of the general fabric evolution equation

We set the following

$$\begin{aligned}
\mathsf{L} &= \begin{pmatrix} a\varepsilon & L_{xy} & L_{xz} \\ L_{yx} & (1-a)\,\varepsilon & L_{yz} \\ L_{zx} & L_{zy} & -\varepsilon \end{pmatrix}, \quad \mathsf{D} = \frac{1}{2}\left(\mathsf{L}+\mathsf{L}^T\right), \quad \mathsf{W} = \frac{1}{2}\left(\mathsf{L}-\mathsf{L}^T\right), \\
\mathbf{u} &= \lambda\left[\left(\mathsf{D}\mathbf{n}\cdot\mathbf{n}\right)\mathbf{n} - \mathsf{D}\mathbf{n}\right] + \mathsf{W}\mathbf{n}, \quad \mathbf{n} = \begin{pmatrix} \sin\theta\cos\varphi \\ \sin\theta\sin\varphi \\ \cos\theta \end{pmatrix}.
\end{aligned}$$

The evolution equation is

$$\frac{\partial\varrho^*}{\partial z}\upsilon_z + \partial_i\left(\varrho^* u_i\right) = 0.$$

We know that,

$$\begin{aligned}
\partial_i &= \frac{\partial}{\partial n_i} - n_i n_j \frac{\partial}{\partial n_j}, \quad u_i^* = \lambda D_{hk} n_h n_k n_i - \lambda D_{ij} n_j + W_{ij} n_j, \\
\partial_i n_h &= \frac{\partial n_h}{\partial n_i} - n_i n_j \frac{\partial n_h}{\partial n_j} = \delta_{ih} - n_i n_h, \partial_i n_i = 3 - 1 = 2, \\
n_i \partial_i \varrho^* &= n_i \frac{\partial\varrho^*}{\partial n_i} - n_i n_i n_j \frac{\partial\varrho^*}{\partial n_j} = n_i \frac{\partial\varrho^*}{\partial n_i} - n_j \frac{\partial\varrho^*}{\partial n_j} = 0, \\
u_i^* \partial_i \varrho^* &= \left[\lambda D_{hk} n_h n_k n_i - \lambda D_{ij} n_j + W_{ij} n_j\right] \partial_i \varrho^* = \left(W_{ij} - \lambda D_{ij}\right) n_j \partial_i \varrho^*,
\end{aligned}$$

$$
\begin{aligned}
\partial_i u_i &= \partial_i \left[\lambda D_{hk} n_h n_k n_i - \lambda D_{ij} n_j + W_{ij} n_j\right] \\
&= \lambda D_{hk} \left(\partial_i n_h n_k n_i\right) - \lambda D_{ij} \left(\partial_i n_j\right) + W_{ij} \left(\partial_i n_j\right) \\
&= \lambda D_{hk} \left(\partial_i n_h\right) n_k n_i + \lambda D_{hk} n_h \left(\partial_i n_k\right) n_i + \lambda D_{hk} n_h n_k \left(\partial_i n_i\right) - \lambda D_{hk} \left(\partial_h n_k\right) + \\
&\quad W_{ij} \left(\partial_i n_j\right) \\
&= \lambda D_{hk} \left(\delta_{ih} - n_i n_h\right) n_k n_i + \lambda D_{hk} n_h \left(\delta_{ik} - n_i n_k\right) n_i + \lambda D_{hk} n_h n_k 2 - \\
&\quad \lambda D_{hk} \left(\delta_{hk} - n_h n_k\right) \\
&= \lambda D_{hk} n_k n_h - \lambda D_{hk} n_h n_k + \lambda D_{hk} n_h n_k - \lambda D_{hk} n_h n_k + 2\lambda D_{hk} n_h n_k + \\
&\quad \lambda D_{ij} \left(n_i n_j\right) \\
&= 3\lambda D_{hk} n_k n_h.
\end{aligned}
$$

Thus, the evolution equation is

$$
\begin{aligned}
\frac{\partial \varrho^*}{\partial z} \upsilon_z + \partial_i \left(\varrho^* u_i^*\right) &= \frac{\partial \varrho^*}{\partial z} \upsilon_z + u_i^* \partial_i \varrho^* + \varrho^* \partial_i u_i^* \\
&= \frac{\partial \varrho^*}{\partial z} \upsilon_z + \left(W_{ij} - \lambda D_{ij}\right) n_j \partial_i \varrho^* + 3\lambda \varrho^* D_{hk} n_k n_h = 0.
\end{aligned}
\tag{A.1}
$$

In spherical coordinate system, Eq. (A.1) reads

$$
\begin{aligned}
&\frac{\partial \varrho^*}{\partial z} \upsilon_z + \\
&\frac{1}{4} \left\{
\begin{array}{c}
3\lambda \left[\begin{array}{c} -\varepsilon - 3\varepsilon \cos(2\theta) + 2\sin(2\theta)\left[\left(L_{xz} + L_{zx}\right)\cos(\varphi) + \left(L_{yz} + L_{zy}\right)\sin\varphi\right] + \\ 2\sin^2(\theta)\left[(-1+2a)\,\varepsilon\cos(2\varphi) + \left(L_{xy} + L_{yx}\right)\sin(2\varphi)\right] \end{array} \right] \varrho^* \\
-2 \left[\begin{array}{c} L_{xy} - L_{yx} + \left(L_{xy} + L_{yx}\right)\lambda\cos^2(\varphi) \\ + \left[-L_{yz} + L_{zy} + \left(L_{yz} + L_{zy}\right)\lambda\right] \frac{\cos\varphi}{\tan\theta} \\ -\sin(\varphi) \left[\begin{array}{c} 2(-1+2a)\,\varepsilon\lambda\cos(\varphi) \\ + \left(-L_{xz} + L_{zx} + \left(L_{xz} + L_{zx}\right)\lambda\right) \frac{1}{\tan\theta} \\ + \left(L_{xy} + L_{yx}\right)\lambda\sin(\varphi) \end{array} \right] \end{array} \right] \frac{\partial \varrho^*}{\partial \varphi} \\
+ \left[\begin{array}{c} -2\left[-L_{xz} + L_{zx} + \left(L_{xz} + L_{zx}\right)\lambda\cos(2\theta)\right]\cos(\varphi) \\ -2\left[-L_{yz} + L_{zy} + \left(L_{yz} + L_{zy}\right)\lambda\cos(2\theta)\right]\sin(\varphi) \\ +\lambda\sin(2\theta)\left[\varepsilon\left(-3 + (1-2a)\cos(2\varphi)\right) - \left(L_{xy} + L_{yx}\right)\sin(2\varphi)\right] \end{array} \right] \frac{\partial \varrho^*}{\partial \theta}
\end{array}
\right\} \\
&= 0,
\end{aligned}
$$

or

$$
\begin{aligned}
4\frac{\partial\varrho^*}{\partial z}\upsilon_z + 3\lambda\varrho^* &\left\{\begin{array}{c}
\varepsilon\left[2\left(2a-1\right)\sin^2\theta\cos 2\varphi - 1 - 3\cos 2\theta\right] \\
+2\left(L_{xy}+L_{yx}\right)\sin^2\theta\sin 2\varphi \\
+2\left(L_{yz}+L_{zy}\right)\sin 2\theta\sin\varphi \\
+2\left(L_{xz}+L_{zx}\right)\sin 2\theta\cos\varphi
\end{array}\right\} \\
+2\frac{\partial\varrho^*}{\partial\varphi} &\left\{\begin{array}{c}
\varepsilon\lambda\left(2a-1\right)\sin 2\varphi + L_{yx} - L_{xy} - \left(L_{yx}+L_{xy}\right)\lambda\cos 2\varphi \\
+\left[L_{yz}-L_{zy}-\left(L_{yz}+L_{zy}\right)\lambda\right]\frac{\cos\varphi}{\tan\theta} + \left[L_{zx}-L_{xz}+\left(L_{xz}+L_{zx}\right)\lambda\right]\frac{\sin\varphi}{\tan\theta}
\end{array}\right\} \\
+2\frac{\partial\varrho^*}{\partial\theta} &\left\{\begin{array}{c}
\frac{1}{2}\lambda\varepsilon\sin 2\theta\left[\left(1-2a\right)\cos 2\varphi - 3\right] - \frac{1}{2}\lambda\left(L_{xy}+L_{yx}\right)\sin 2\theta\sin 2\varphi \\
+\left[L_{yz}-L_{zy}-\left(L_{yz}+L_{zy}\right)\lambda\cos 2\theta\right]\sin\varphi \\
+\left[L_{xz}-L_{zx}-\left(L_{xz}+L_{zx}\right)\lambda\cos 2\theta\right]\cos\varphi
\end{array}\right\} \\
&= 0.
\end{aligned}
$$

Appendix B

Derivation of the scalar invariant D_t^2

We seek the general solution of D_t^2 for the calculation of the fabric deformability for the case of unrestricted fabric evolution which is defined by Eq. (3.2)

$$D_{\mathrm{t}}^2 = \mathsf{D}\mathbf{n} \cdot \mathsf{D}\mathbf{n} - (\mathsf{D}\mathbf{n} \cdot \mathbf{n})^2,$$

or in index notation

$$D_{\mathrm{t}}^2 = D_{ij} n_j D_{ik} n_k - (D_{ij} n_i n_j)^2.$$

With the definitions of D, L and $\mathbf{n}$ presented in Appendix A, we can write

$$\begin{aligned}
D_{ij} n_i = \\
&\left\{\frac{1}{2}(L_{xz} + L_{zx})\cos\theta + a\epsilon\cos\varphi\sin\theta + \frac{1}{2}(L_{xy} + L_{yx})\sin\theta\sin\varphi\right\}, \\
&\left\{\frac{1}{2}(L_{yz} + L_{zy})\cos\theta + \frac{1}{2}(L_{xy} + L_{yx})\cos\varphi\sin\theta + (1-a)\epsilon\sin\theta\sin\varphi\right\}, \\
&\left\{-\epsilon\cos\theta + \frac{1}{2}(L_{xz} + L_{zx})\cos\varphi\sin\theta + \frac{1}{2}(L_{yz} + L_{zy})\sin\theta\sin\varphi\right\}.
\end{aligned}$$

With this expression $D_{ij} n_i n_j$ reads,

$$\begin{aligned}
D_{ij} n_i n_j = \\
&\cos\varphi\sin\theta\left(\frac{1}{2}(L_{xz} + L_{zx})\cos\theta + a\epsilon\cos\varphi\sin\theta + \frac{1}{2}(L_{xy} + L_{yx})\sin\theta\sin\varphi\right) \\
&+\cos\theta\left(-\epsilon\cos\theta + \frac{1}{2}(L_{xz} + L_{zx})\cos\varphi\sin\theta + \frac{1}{2}(L_{yz} + L_{zy})\sin\theta\sin\varphi\right) \\
&+\sin\theta\sin\varphi\left(\frac{1}{2}(L_{yz} + L_{zy})\cos\theta + \frac{1}{2}(L_{xy} + L_{yx})\cos\varphi\sin\theta + (1-a)\epsilon\sin\theta\sin\varphi\right),
\end{aligned}$$

and

$$
\begin{aligned}
&D_{ij}n_jD_{ik}n_k = \\
&\quad \left(\frac{1}{2}(L_{xz}+L_{zx})\cos\theta + a\epsilon\cos\varphi\sin\theta + \frac{1}{2}(L_{xy}+L_{yx})\sin\theta\sin\varphi\right)^2 \\
&\quad \left(-\epsilon\cos\theta + \frac{1}{2}(L_{xz}+L_{zx})\cos\varphi\sin\theta + \frac{1}{2}(L_{yz}+L_{zy})\sin\theta\sin\varphi\right)^2 \\
&\quad + \left(\frac{1}{2}(L_{yz}+L_{zy})\cos\theta + \frac{1}{2}(L_{xy}+L_{yx})\cos\varphi\sin\theta + (1-a)\epsilon\sin\theta\sin\varphi\right)^2,
\end{aligned}
$$

so that D_t^2 is given by

$$
\begin{aligned}
&D_t^2 = \\
&\quad \left(\frac{1}{2}(L_{xz}+L_{zx})\cos\theta + a\epsilon\cos\varphi\sin\theta + \frac{1}{2}(L_{xy}+L_{yx})\sin\theta\sin\varphi\right)^2 \\
&\quad + \left(-\epsilon\cos\theta + \frac{1}{2}(L_{xz}+L_{zx})\cos\varphi\sin\theta + \frac{1}{2}(L_{yz}+L_{zy})\sin\theta\sin\varphi\right)^2 \\
&\quad + \left(\frac{1}{2}(L_{yz}+L_{zy})\cos\theta + \frac{1}{2}(L_{xy}+L_{yx})\cos\varphi\sin\theta + (1-a)\epsilon\sin\theta\sin\varphi\right)^2 \\
&\quad - \left[\cos\varphi\sin\theta\left(\frac{1}{2}(L_{xz}+L_{zx})\cos\theta + a\epsilon\cos\varphi\sin\theta + \frac{1}{2}(L_{xy}+L_{yx})\sin\theta\sin\varphi\right)\right]^2 \\
&\quad - \left[\cos\theta\left(-\epsilon\cos\theta + \frac{1}{2}(L_{xz}+L_{zx})\cos\varphi\sin\theta + \frac{1}{2}(L_{yz}+L_{zy})\sin\theta\sin\varphi\right)\right]^2 \\
&\quad - \left[\sin\theta\sin\varphi\left(\frac{1}{2}(L_{yz}+L_{zy})\cos\theta + \frac{1}{2}(L_{xy}+L_{yx})\cos\varphi\sin\theta + (1-a)\epsilon\sin\theta\sin\varphi\right)\right]^2
\end{aligned}
\tag{B.1}
$$

For the EDML application, Eq. (B.1) is not dependent on L_{zx}, L_{xy}, L_{yx},L_{yz} and L_{zy} due to the assumption in Eq. (4.11).

Appendix C

Numerical procedure for the one-dimensional EDML flow model

C.1 Unrestricted fabric evolution equation discretization

The numerical solution of Eq. (4.14) is obtained by using a finite volume discretization scheme. We can rewrite Eq. (4.14) in a simpler form to carry out the discretization that reads,

$$\frac{\partial \rho^*(z,\theta,\varphi)}{\partial z} v_z(z) + A(\theta,\varphi)\frac{\partial \rho^*(\theta,\varphi)}{\partial \varphi} + B(\theta,\varphi)\frac{\partial \rho^*(\theta,\varphi)}{\partial \theta} + C(\theta,\varphi) = 0, \tag{C.1}$$

where $A(\theta,\varphi) = D(\theta,\varphi) + \frac{1}{\sin\theta}E(\theta,\varphi)$ and the general discretization of the field variables are given by,

$\theta_i = (\frac{1}{2} + i)\Delta\theta; \quad \Delta\theta = \frac{\pi}{N\theta}; \quad i = 0, ..., N\theta - 1$

$\varphi_j = j\Delta\varphi; \quad \Delta\varphi = \frac{2\pi}{N\varphi}; \quad j = 0......, N\varphi$

$z_{h+1} = z_h + (v_z)_h\,\Delta t.$

For the inner part of the spherical domain, $i = 0, ..., N\theta - 2$, $j = 0......, N\varphi - 1$, $h = 0, ..., Nz$, the volume integration of Eq. (C.1) gives,

$$0 = \int_{\theta_i - \frac{\Delta\theta}{2}}^{\theta_i + \frac{\Delta\theta}{2}} \sin\theta \int_{\varphi_j - \frac{\Delta\varphi}{2}}^{\varphi_j + \frac{\Delta\varphi}{2}} \left[\frac{\partial \rho^*}{\partial z} v_z(z) + D \frac{\partial \rho^*}{\partial \varphi} + \frac{E}{\sin\theta} \frac{\partial \rho^*}{\partial \varphi} + B \frac{\partial \rho^*}{\partial \theta} + C \right] d\theta d\varphi.$$

Carrying out the integration gives,

$$\begin{gathered}
v_{z_h} \frac{\rho^*(z_{h+1}, \theta_i, \varphi_j) - \rho^*(z_h, \theta_i, \varphi_j)}{\Delta z} \left[\cos(\theta_i - \frac{\Delta\theta}{2}) - \cos(\theta_i + \frac{\Delta\theta}{2}) \right] \Delta\varphi \\
+ D(\theta_i, \varphi_j) \frac{\rho^*(z_h, \theta_i, \varphi_{j+1}) - \rho^*(z_h, \theta_i, \varphi_{j-1})}{2\Delta\varphi} \left[\cos(\theta_i - \frac{\Delta\theta}{2}) - \cos(\theta_i + \frac{\Delta\theta}{2}) \right] \Delta\varphi \\
+ E(\theta_i, \varphi_j) \frac{\rho^*(z_h, \theta_i, \varphi_{j+1}) - \rho^*(z_h, \theta_i, \varphi_{j-1})}{2\Delta\varphi} \Delta\theta\Delta\varphi \\
+ B(\theta_i, \varphi_j) \frac{\rho^*(z_h, \theta_{i+1}, \varphi_j) - \rho^*(z_h, \theta_{i-1}, \varphi_j)}{2\Delta\theta} \left[\cos(\theta_i - \frac{\Delta\theta}{2}) - \cos(\theta_i + \frac{\Delta\theta}{2}) \right] \Delta\varphi \\
+ C(\theta_i, \varphi_j) \left[\cos(\theta_i - \frac{\Delta\theta}{2}) - \cos(\theta_i + \frac{\Delta\theta}{2}) \right] \Delta\varphi = 0,
\end{gathered}$$

which simplifies to,

$$\begin{aligned}
&\rho^*(z_{h+1}, \theta_i, \varphi_j) = \\
&\quad \rho^*(z_h, \theta_i, \varphi_j) - \frac{D(\theta_i, \varphi_j)\Delta z}{v_{z_h} 2\Delta\varphi} [\rho^*(z_h, \theta_i, \varphi_{j+1}) - \rho^*(z_h, \theta_i, \varphi_{j-1})] \\
&\quad - \frac{E(\theta_i, \varphi_j)\Delta z}{v_{z_h} \Delta\varphi \left[\cos(\theta_i - \frac{\Delta\theta}{2}) - \cos(\theta_i + \frac{\Delta\theta}{2}) \right]} [\rho^*(z_h, \theta_i, \varphi_{j+1}) - \rho^*(z_h, \theta_i, \varphi_{j-1})] \Delta\theta \\
&\quad - \frac{B(\theta_i, \varphi_j)\Delta z}{v_{z_h} 2\Delta\theta} [\rho^*(z_h, \theta_{i+1}, \varphi_j) - \rho^*(z_h, \theta_{i-1}, \varphi_j)] \\
&\quad - \frac{C(\theta_i, \varphi_j)\Delta z}{v_{z_h}}.
\end{aligned} \tag{C.2}$$

On the north pole of the spherical domain, $i = 0$, $j = 0......, N\varphi - 1$, $h = 0, ..., Nz$, in analogy to the procedure presented for the inner domain, the integration reads,

$$0 = \int_0^{\Delta\theta} \sin\theta \int_{\varphi_j - \frac{\Delta\varphi}{2}}^{\varphi_j + \frac{\Delta\varphi}{2}} \left[\frac{\partial \rho^*}{\partial z} v_z(z) + D \frac{\partial \rho^*}{\partial \varphi} + \frac{E}{\sin\theta} \frac{\partial \rho^*}{\partial \varphi} + B \frac{\partial \rho^*}{\partial \theta} + C \right] d\theta d\varphi,$$

which simplifies to,

$$
\begin{gathered}
v_{z_h}\frac{\rho^*(z_{h+1},\frac{\Delta\theta}{2},\varphi_j)-\rho^*(z_h,\frac{\Delta\theta}{2},\varphi_j)}{\Delta z}[1-\cos\Delta\theta]\Delta\varphi \\
+D(\frac{\Delta\theta}{2},\varphi_j)\frac{\rho^*(z_h,\frac{\Delta\theta}{2},\varphi_{j+1})-\rho^*(z_h,\frac{\Delta\theta}{2},\varphi_{j-1})}{2\Delta\varphi}[1-\cos\Delta\theta]\Delta\varphi \\
+E(\frac{\Delta\theta}{2},\varphi_j)\frac{\rho^*(z_h,\frac{\Delta\theta}{2},\varphi_{j+1})-\rho^*(z_h,\frac{\Delta\theta}{2},\varphi_{j-1})}{2\Delta\varphi}\Delta\theta\Delta\varphi \\
+B(\frac{\Delta\theta}{2},\varphi_j)\frac{\frac{1}{2}\rho^*(z_h,\frac{3}{2}\Delta\theta,\varphi_j)+\frac{1}{2}\rho^*(z_h,\frac{\Delta\theta}{2},\varphi_j)-\frac{1}{Nl}\sum_{l=0}^{Nl-1}\rho^*(z_h,\frac{\Delta\theta}{2},\varphi_l)}{\Delta\theta}[1-\cos\Delta\theta]\Delta\varphi \\
+C(\frac{\Delta\theta}{2},\varphi_j)[1-\cos\Delta\theta]\Delta\varphi=0,
\end{gathered}
$$

and therefore,

$$
\begin{aligned}
\rho^*(z_{h+1},\frac{\Delta\theta}{2},\varphi_j) &= \rho^*(z_h,\frac{\Delta\theta}{2},\varphi_j) \\
&- \frac{D(\frac{\Delta\theta}{2},\varphi_j)\Delta z}{2\Delta\varphi\ v_{z_h}}\left[\rho^*(z_h,\frac{\Delta\theta}{2},\varphi_{j+1})-\rho^*(z_h,\frac{\Delta\theta}{2},\varphi_{j-1})\right] \\
&- \frac{E(\frac{\Delta\theta}{2},\varphi_j)\Delta z}{2\Delta\varphi\ v_{z_h}(1-\cos\Delta\theta)}\left[\rho^*(z_h,\frac{\Delta\theta}{2},\varphi_{j+1})-\rho^*(z_h,\frac{\Delta\theta}{2},\varphi_{j-1})\right]\Delta\theta \\
&- \frac{B(\frac{\Delta\theta}{2},\varphi_j)\Delta z}{\Delta\theta\ v_{z_h}} \\
&\quad \left[\frac{1}{2}\rho^*(z_h,\frac{3}{2}\Delta\theta,\varphi_j)+\frac{1}{2}\rho^*(z_h,\frac{\Delta\theta}{2},\varphi_j)-\frac{1}{Nl}\sum_{l=0}^{Nl-1}\rho^*(z_h,\frac{\Delta\theta}{2},\varphi_l)\right] \\
&- \frac{C(\frac{\Delta\theta}{2},\varphi_j)}{v_{z_h}}\Delta z. \qquad \text{(C.3)}
\end{aligned}
$$

On the south pole, $i=N\theta-1$, $j=0......,N\varphi-1$, $h=0,....,Nz$, we obtain similarly

$$
\begin{aligned}
&\rho^*(z_{h+1}, \pi - \frac{\Delta\theta}{2}, \varphi_j) = \\
&\quad \rho^*(z_h, \pi - \frac{\Delta\theta}{2}, \varphi_j) \\
&\quad -\frac{D(\pi - \frac{\Delta\theta}{2}, \varphi_j)\Delta z}{2\Delta\varphi \; v_{z_h}} \left[\rho^*(z_h, \pi - \frac{\Delta\theta}{2}, \varphi_{j+1}) - \rho^*(z_h, \pi - \frac{\Delta\theta}{2}, \varphi_{j-1})\right] \\
&\quad -\frac{E(\pi - \frac{\Delta\theta}{2}, \varphi_j)\Delta z}{2\Delta\varphi \; v_{z_h}(1 - \cos\Delta\theta)} \left[\rho^*(z_h, \pi - \frac{\Delta\theta}{2}, \varphi_{j+1}) - \rho^*(z_h, \pi - \frac{\Delta\theta}{2}, \varphi_{j-1})\right] \Delta\theta \\
&\quad -\frac{B(\frac{\pi - \Delta\theta}{2}, \varphi_j)\Delta z}{\Delta\theta \; v_{z_h}} \\
&\quad \left[\frac{1}{Nl}\sum_{l=0}^{Nl-1} \rho^*(z_h, \pi - \frac{\Delta\theta}{2}, \varphi_l) - \frac{1}{2}\rho^*(z_h, \pi - \frac{3}{2}\Delta\theta, \varphi_j) - \frac{1}{2}\rho^*(z_h, \pi - \frac{\Delta\theta}{2}, \varphi_j)\right] \\
&\quad \frac{C(\pi - \frac{\Delta\theta}{2}, \varphi_j)}{v_{z_h}}\Delta z.
\end{aligned} \tag{C.4}
$$

C.2 Transversely isotropic fabric evolution equation discretization

Solution of Equation 4.15 is obtained with a forward finite-difference scheme (Euler method), so that the discretization of Eq. (4.15) gives

$$
\frac{\rho^*(i+1,j) - \rho^*(i,j)}{\Delta z} v_{z_i} = \frac{\rho^*(i,j+1) - \rho^*(i,j)}{\Delta\theta} \frac{3}{4}\iota\epsilon \sin 2\theta + \frac{3}{4}\iota\rho^*(i,j)\epsilon(1 + 3\cos 2\theta),
$$

which yields

$$
\rho^*(i+1,j) = \rho^*(i,j) + \frac{\Delta z}{v_{z_i}} \left[\frac{\rho^*(i,j+1) - \rho^*(i,j)}{\Delta\theta} \frac{3}{4}\iota\epsilon \sin 2\theta + \frac{3}{4}\iota\rho^*(i,j)\epsilon(1 + 3\cos 2\theta)\right], \tag{C.5}
$$

with

$\Delta\theta = \frac{\pi}{N\theta}; \qquad i = 0, ..., N\theta$

$z_{i+1} = z_i + (v_z)_i \, \Delta t.$

Appendix D

Lagrangian model for the EDML fabric evolution equation

The Lagrangian approach treats the fabric as an assemblage of discrete grains having each a given orientation for their c-axis. The orientation of the c-axis is given by the vector $\mathbf{n}$, whose components are

$$n_1 = \sin\theta\cos\varphi \qquad n_2 = \sin\theta\sin\varphi \qquad n_3 = \cos\theta. \tag{D.1}$$

The evolution of the c-axis orientation is given by the equation

$$\mathbf{n}(c+dt) = \mathbf{n}(t) + \dot{\mathbf{n}}dt. \tag{D.2}$$

The term $\dot{\mathbf{n}}$ can be computed by using Eq. (3.18), so that with

$$u_i^* = \iota D_{hk}n_hn_kn_i - \iota D_{ij}n_j + W_{ij}n_j \tag{D.3}$$

the components $\dot{n_1}$, $\dot{n_2}$ and $\dot{n_3}$ are given by

$$\begin{aligned}\dot{n_1} = u_1^* = \iota(&D_{11}n_1n_1n_1 + D_{13}n_1n_3n_1 + D_{22}n_2n_2n_1\\ &+D_{13}n_3n_1n_1 + D_{33}n_3n_3n_1) - \iota(D_{11}n_1 + D_{13}n_3) + W_{13}n_3\end{aligned} \tag{D.4}$$

$$\begin{aligned}\dot{n_2} = u_2^* = \iota(&D_{11}n_1n_1n_2 + D_{13}n_1n_3n_2 + D_{22}n_2n_2n_2\\ &+D_{13}n_3n_1n_2 + D_{33}n_3n_3n_2) - \iota D_{22}n_2\end{aligned} \tag{D.5}$$

$$\dot{n_3} = u_3^* = \iota(D_{11}n_1n_1n_3 + D_{13}n_1n_3n_3 + D_{22}n_2n_2n_3 \\ +D_{13}n_3n_1n_3 + D_{33}n_3n_3n_3) - \iota(D_{13}n_1 + D_{33}n_3) + W_{31}n_1. \quad \text{(D.6)}$$

Appendix E

Procedure for the stability analysis of the anisotropic flow law

We define a potential (work rate) given by the deformation and the deviatoric stress tensors as

$$\phi = \mathsf{S} : \mathsf{D}, \tag{E.1}$$

such that, by using Eq. (3.7), the potential ϕ reads, with the notation,
$d_i = A(T')\, \sigma^{n-1}\, S_i\, \hat{E}(\mathcal{A})$,

$$\phi = d_i S_i = A(T')\, \sigma^{n-1}\, \hat{E}(\mathcal{A})\, S_i S_i. \tag{E.2}$$

In the following, we express the tensor S in vector notation in a space of 5-dimensions, hence, according to Lequeu and others (1987) and Castelnau (1996)

$$\left\{ \begin{array}{c} S_1 = \frac{1}{\sqrt{2}}(S_{22} - S_{11}) \\ S_2 = \sqrt{\frac{3}{2}} S_{33} \\ S_3 = \sqrt{2} S_{23} \\ S_4 = \sqrt{2} S_{13} \\ S_5 = \sqrt{2} S_{12} \end{array} \right\}. \tag{E.3}$$

For $n = 3$, $\sigma^2 = \frac{1}{2} S_{ij} S_{ij} = \frac{1}{2} S_i S_i$. We are interested in evaluating the equipotential defined in the $\mathbf{S}_1 - \mathbf{S}_2(S_{33},\, S_{13})$ plane so that,

$$\begin{aligned} S_2 &= R\cos\theta \\ S_4 &= R\sin\theta, \end{aligned} \tag{E.4}$$

where θ is the angle describing all possible configurations of stresses. With Eq. (E.4), we write $\sigma^2 = \frac{1}{2} S_i S_i = \frac{1}{2} R^2$ and Eq. (E.2) becomes

$$\phi = 2\, A(T')\, \sigma^{n+1}\, \hat{E}(\mathcal{A}), \tag{E.5}$$

and

$$\phi = 2\, A(T') \left(\frac{R^2}{2} \right)^{\frac{n+1}{2}} \hat{E}(\mathcal{A}) = \bar{\phi}, \tag{E.6}$$

where $\bar{\phi}$ is a positive real constant. Solving Eq. (E.6) for R gives

$$\begin{aligned} R^{n+1} &= \frac{2^{\frac{n+1}{2}}\, \bar{\phi}}{2\, A(T')\, \hat{E}(\mathcal{A})} \\ R &= \sqrt[n+1]{2} \frac{2^{\frac{n+1}{2}}\, \bar{\phi}}{2\, A(T')\, \hat{E}(\mathcal{A})} \\ R &= \frac{2^{\frac{1}{2}}\, \bar{\phi}^{\frac{1}{n+1}}}{2^{\frac{1}{n+1}} [A(T')\, \hat{E}(\mathcal{A})]^{\frac{1}{n+1}}}. \end{aligned} \tag{E.7}$$

R can be interpreted as the radius of the ellipse described by the equipotential (Fig. E.1). With Eq. (E.3), we write

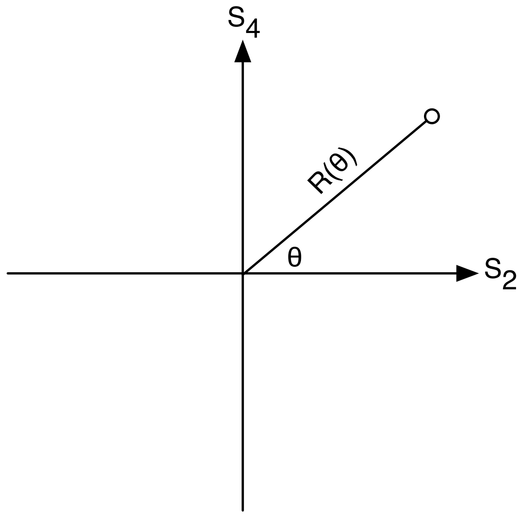

Figure E.1: Parameters for drawing the ellipse defined by the equipotential

$$\begin{aligned} S_{33} &= \frac{R \cos\theta}{\sqrt{\frac{3}{2}}} \\ S_{13} &= \frac{R \sin\theta}{\sqrt{2}}. \end{aligned} \tag{E.8}$$

The solution of Eq. (E.7) is obtained by solving $\mathcal{A}$ with Eq. (5.9), then using Eq. (E.8) and by expressing the second and fourth-order orientation tensor in the orthotropic reference frame, we have

$$S_{ij}a_{jh}S_{hi} = a_{11}^{(2)}S_{13}^2 + a_{11}^{(2)}(S_{13}^2 + S_{33}^2),$$

and

$$a_{ijkl}^{(4)}S_{kl}S_{ij} = a_{3333}^{(4)}S_{33}^2 + 4a_{1133}^{(4)}S_{13}^2$$

and by noting that $\mathrm{tr}(\mathsf{S}) = 2\sigma^2 = R^2$, Eq. (5.9) reads

$$\mathcal{A} = 5\left[\frac{1}{2}a_{11}^{(2)}\sin^2\theta + a_{33}^{(2)}\left(\frac{1}{2}\sin^2\theta + \frac{2}{3}\cos^2\theta\right) - \left(\frac{2}{3}a_{3333}^{(4)}\cos^2\theta + 4a_{1133}^{(4)}\frac{1}{2}\sin^2\theta\right)\right].$$

Appendix F

Decomposition of the orientation tensors based equation for the deformability $\mathcal{A}$

We need to solve the contracted and double contracted products in Eq. (5.8). The component involving the term $\mathsf{a}^{(2)}$ reads in index notation

$$a_{jh}^{<2>} D_{hi} D_{ij}.$$

Summation on all components gives

$$\begin{aligned}
= \quad & a_{11}^{<2>} D_{11} D_{11} + a_{11}^{<2>} D_{12} D_{21} + a_{11}^{<2>} D_{13} + D_{31} \\
& + a_{22}^{<2>} D_{21} D_{12} + a_{22}^{<2>} D_{22} D_{22} + a_{22}^{<2>} D_{23} D_{32} \\
& + a_{33}^{<2>} D_{31} D_{13} + a_{33}^{<2>} D_{32} D_{23} + a_{33}^{<2>} D_{33} D_{33} \\
& + a_{12}^{<2>} D_{21} D_{11} + a_{12}^{<2>} D_{22} D_{21} + a_{12}^{<2>} D_{23} D_{31} \\
& + a_{21}^{<2>} D_{11} D_{12} + a_{21}^{<2>} D_{12} D_{22} + a_{21}^{<2>} D_{13} D_{32} \\
& + a_{23}^{<2>} D_{31} D_{12} + a_{23}^{<2>} D_{32} D_{22} + a_{23}^{<2>} D_{33} D_{32} \\
& + a_{32}^{<2>} D_{21} D_{13} + a_{32}^{<2>} D_{22} D_{23} + a_{32}^{<2>} D_{23} D_{33} \\
& + a_{13}^{<2>} D_{31} D_{11} + a_{13}^{<2>} D_{32} D_{21} + a_{13}^{<2>} D_{33} D_{31} \\
& + a_{31}^{<2>} D_{11} D_{13} + a_{31}^{<2>} D_{12} D_{23} + a_{31}^{<2>} D_{13} D_{33}
\end{aligned}$$

$$
\begin{aligned}
= \quad & a_{11}^{<2>}(D_{11})^2 + a_{11}^{<2>}(D_{12})^2 + a_{11}^{<2>}(D_{13})^2 \\
& + a_{22}^{<2>}(D_{12})^2 + a_{22}^{<2>}(D_{22})^2 + a_{22}^{<2>}(D_{23})^2 \\
& + a_{33}^{<2>}(D_{13})^2 + a_{33}^{<2>}(D_{23})^2 + a_{33}^{<2>}(D_{33})^2 \\
& + a_{12}^{<2>}D_{11}D_{12} + a_{12}^{<2>}D_{22}D_{12} + a_{12}^{<2>}D_{23}D_{13} \\
& + a_{12}^{<2>}D_{11}D_{12} + a_{12}^{<2>}D_{22}D_{12} + a_{12}^{<2>}D_{23}D_{13} \\
& + a_{23}^{<2>}D_{13}D_{12} + a_{23}^{<2>}D_{22}D_{23} + a_{23}^{<2>}D_{33}D_{23} \\
& + a_{23}^{<2>}D_{13}D_{12} + a_{23}^{<2>}D_{22}D_{23} + a_{23}^{<2>}D_{33}D_{23} \\
& + a_{13}^{<2>}D_{11}D_{13} + a_{13}^{<2>}D_{23}D_{12} + a_{13}^{<2>}D_{33}D_{13} \\
& + a_{13}^{<2>}D_{11}D_{13} + a_{13}^{<2>}D_{23}D_{12} + a_{13}^{<2>}D_{33}D_{13}
\end{aligned}
$$

$$
\begin{aligned}
= \quad & a_{11}^{<2>}((D_{11})^2 + (D_{12})^2 + (D_{13})^2) + a_{22}^{<2>}((D_{12})^2 + (D_{22})^2 + (D_{23})^2) \\
& + a_{33}^{<2>}((D_{13})^2 + (D_{23})^2 + (D_{33})^2) \\
& + a_{12}^{<2>}(2D_{11}D_{12} + 2D_{22}D_{12} + 2D_{23}D_{13}) \\
& + a_{23}^{<2>}(2D_{13}D_{12} + 2D_{22}D_{23} + 2D_{33}D_{23}) \\
& + a_{13}^{<2>}(2D_{11}D_{13} + 2D_{23}D_{12} + 2D_{33}D_{13})
\end{aligned} \tag{F.1}
$$

Similarly, the component involving the term $a^{(4)}$ reads in index notation

$$a_{ijkl}^{<4>}D_{kl}D_{ij}$$

Summation on all components gives

$$a^{<4>}_{1111}(D_{11})^2 + a^{<4>}_{2222}(D_{22})^2 + a^{<4>}_{3333}(D_{33})^2$$

$$+a^{<4>}_{1122}D_{11}D_{22} + a^{<4>}_{1212}D_{12}D_{12} + a^{<4>}_{2211}D_{22}D_{11} + a^{<4>}_{2121}D_{21}D_{21} + a^{<4>}_{1221}D_{12}D_{21} + a^{<4>}_{2112}D_{21}D_{12}$$
$$+a^{<4>}_{1133}D_{11}D_{33} + a^{<4>}_{1313}D_{13}D_{13} + a^{<4>}_{3311}D_{33}D_{11} + a^{<4>}_{3131}D_{31}D_{31} + a^{<4>}_{1331}D_{13}D_{31} + a^{<4>}_{3113}D_{31}D_{13}$$
$$+a^{<4>}_{2233}D_{22}D_{33} + a^{<4>}_{2323}D_{23}D_{23} + a^{<4>}_{3322}D_{33}D_{22} + a^{<4>}_{3232}D_{32}D_{32} + a^{<4>}_{2332}D_{23}D_{32} + a^{<4>}_{3223}D_{32}D_{23}$$

$$+a^{<4>}_{1123}D_{11}D_{23} + a^{<4>}_{1132}D_{11}D_{32} + a^{<4>}_{2213}D_{22}D_{13} + a^{<4>}_{2231}D_{22}D_{31} + a^{<4>}_{3321}D_{33}D_{21} + a^{<4>}_{3312}D_{33}D_{12}$$
$$+a^{<4>}_{1213}D_{12}D_{13} + a^{<4>}_{1231}D_{12}D_{31} + a^{<4>}_{1223}D_{12}D_{23} + a^{<4>}_{1232}D_{12}D_{32} + a^{<4>}_{2113}D_{21}D_{13} + a^{<4>}_{2131}D_{21}D_{31}$$
$$+a^{<4>}_{2123}D_{21}D_{23} + a^{<4>}_{2132}D_{21}D_{32} + a^{<4>}_{1312}D_{13}D_{12} + a^{<4>}_{1321}D_{13}D_{21} + a^{<4>}_{1323}D_{13}D_{23} + a^{<4>}_{1332}D_{13}D_{32}$$
$$+a^{<4>}_{3112}D_{31}D_{12} + a^{<4>}_{3121}D_{31}D_{21} + a^{<4>}_{3123}D_{31}D_{23} + a^{<4>}_{3132}D_{31}D_{32} + a^{<4>}_{2311}D_{23}D_{11} + a^{<4>}_{3211}D_{32}D_{11}$$
$$+a^{<4>}_{1322}D_{13}D_{22} + a^{<4>}_{3122}D_{31}D_{22} + a^{<4>}_{2133}D_{21}D_{33} + a^{<4>}_{1233}D_{12}D_{33} + a^{<4>}_{2312}D_{23}D_{12} + a^{<4>}_{2321}D_{23}D_{21}$$
$$+a^{<4>}_{2313}D_{23}D_{13} + a^{<4>}_{2331}D_{23}D_{31} + a^{<4>}_{3212}D_{32}D_{12} + a^{<4>}_{3221}D_{32}D_{21} + a^{<4>}_{3213}D_{32}D_{13} + a^{<4>}_{3231}D_{32}D_{31}$$

$$+a^{<4>}_{1113}D_{11}D_{13} + a^{<4>}_{1112}D_{11}D_{12} + a^{<4>}_{2111}D_{21}D_{11} + a^{<4>}_{3111}D_{31}D_{11} + a^{<4>}_{1211}D_{12}D_{11} + a^{<4>}_{1311}D_{13}D_{11}$$
$$+a^{<4>}_{1121}D_{11}D_{21} + a^{<4>}_{1131}D_{11}D_{31} + a^{<4>}_{2221}D_{22}D_{21} + a^{<4>}_{2223}D_{22}D_{23} + a^{<4>}_{1222}D_{12}D_{22} + a^{<4>}_{3222}D_{32}D_{22}$$
$$+a^{<4>}_{2122}D_{21}D_{22} + a^{<4>}_{2322}D_{23}D_{22} + a^{<4>}_{2212}D_{22}D_{12} + a^{<4>}_{2232}D_{22}D_{32} + a^{<4>}_{3331}D_{33}D_{31} + a^{<4>}_{3332}D_{33}D_{32}$$
$$+a^{<4>}_{1333}D_{13}D_{33} + a^{<4>}_{2333}D_{23}D_{33} + a^{<4>}_{3133}D_{31}D_{33} + a^{<4>}_{3233}D_{32}D_{33} + a^{<4>}_{3313}D_{33}D_{13} + a^{<4>}_{3323}D_{33}D_{23}$$

With the symmetry conditions defined in Eq. (5.5), independent terms of $a^{(4)}$ are :
- group $a^{<4>}_{iijj}$, three independent

$$\left\{\begin{array}{c} a^{<4>}_{1122} \\ a^{<4>}_{1212} \\ a^{<4>}_{2211} \\ a^{<4>}_{2121} \\ a^{<4>}_{1221} \\ a^{<4>}_{2112} \end{array}\right\} = a^{<4>}_{1122}, \left\{\begin{array}{c} a^{<4>}_{1133} \\ a^{<4>}_{1313} \\ a^{<4>}_{3311} \\ a^{<4>}_{3131} \\ a^{<4>}_{1331} \\ a^{<4>}_{3113} \end{array}\right\} = a^{<4>}_{1133}, \left\{\begin{array}{c} a^{<4>}_{2233} \\ a^{<4>}_{2323} \\ a^{<4>}_{3322} \\ a^{<4>}_{3232} \\ a^{<4>}_{2332} \\ a^{<4>}_{3223} \end{array}\right\} = a^{<4>}_{2233}$$

- group $a^{<4>}_{iijk}$, three independent

$$\left\{\begin{array}{c} a^{<4>}_{1123} \\ a^{<4>}_{1132} \\ a^{<4>}_{2113} \\ a^{<4>}_{2131} \\ a^{<4>}_{1312} \\ a^{<4>}_{3112} \\ a^{<4>}_{3121} \\ a^{<4>}_{2311} \\ a^{<4>}_{3211} \\ a^{<4>}_{1213} \\ a^{<4>}_{1231} \\ a^{<4>}_{1321} \end{array}\right\} = a^{<4>}_{1123}, \left\{\begin{array}{c} a^{<4>}_{2213} \\ a^{<4>}_{2231} \\ a^{<4>}_{1223} \\ a^{<4>}_{1232} \\ a^{<4>}_{2123} \\ a^{<4>}_{1322} \\ a^{<4>}_{3122} \\ a^{<4>}_{2312} \\ a^{<4>}_{2321} \\ a^{<4>}_{3212} \\ a^{<4>}_{3221} \\ a^{<4>}_{2132} \end{array}\right\} = a^{<4>}_{2231}, \left\{\begin{array}{c} a^{<4>}_{3321} \\ a^{<4>}_{3312} \\ a^{<4>}_{1323} \\ a^{<4>}_{1332} \\ a^{<4>}_{3123} \\ a^{<4>}_{3132} \\ a^{<4>}_{2313} \\ a^{<4>}_{2331} \\ a^{<4>}_{3213} \\ a^{<4>}_{3231} \\ a^{<4>}_{2133} \\ a^{<4>}_{1233} \end{array}\right\} = a^{<4>}_{3312}$$

- group $a^{<4>}_{iiij}$, six independent

$$\left\{\begin{array}{c} a^{<4>}_{1112} \\ a^{<4>}_{2111} \\ a^{<4>}_{1211} \\ a^{<4>}_{1121} \end{array}\right\} = a^{<4>}_{1112}, \left\{\begin{array}{c} a^{<4>}_{1113} \\ a^{<4>}_{1311} \\ a^{<4>}_{1131} \\ a^{<4>}_{3111} \end{array}\right\} = a^{<4>}_{1131}, \left\{\begin{array}{c} a^{<4>}_{2221} \\ a^{<4>}_{1222} \\ a^{<4>}_{2122} \\ a^{<4>}_{2212} \end{array}\right\} = a^{<4>}_{2212},$$

$$\left\{\begin{array}{c} a_{2223}^{<4>} \\ \\ a_{3222}^{<4>} \\ \\ a_{2322}^{<4>} \\ \\ a_{2232}^{<4>} \end{array}\right\} = a_{2223}^{<4>}, \left\{\begin{array}{c} a_{3331}^{<4>} \\ \\ a_{1333}^{<4>} \\ \\ a_{3133}^{<4>} \\ \\ a_{3313}^{<4>} \end{array}\right\} = a_{3331}^{<4>}, \left\{\begin{array}{c} a_{3332}^{<4>} \\ \\ a_{2333}^{<4>} \\ \\ a_{3233}^{<4>} \\ \\ a_{3323}^{<4>} \end{array}\right\} = a_{3332}^{<4>}.$$

Then it follows,

$$\begin{aligned}
& a_{ijkl}^{<4>} D_{kl} D_{ij} = \\
& \quad a_{1111}^{<4>} (D_{11})^2 + a_{2222}^{<4>} (D_{22})^2 + a_{3333}^{<4>} (D_{33})^2 \\
& \\
& \quad + a_{1122}^{<4>} (D_{11}D_{22} + D_{11}D_{22} + D_{12}D_{12} + D_{12}D_{12} + D_{12}D_{12} + D_{12}D_{12}) \\
& \quad + a_{1133}^{<4>} (D_{11}D_{33} + D_{11}D_{33} + D_{13}D_{13} + D_{13}D_{13} + D_{13}D_{13} + D_{13}D_{13}) \\
& \quad + a_{2233}^{<4>} (D_{22}D_{33} + D_{22}D_{33} + D_{23}D_{23} + D_{23}D_{23} + D_{23}D_{23} + D_{23}D_{23}) \\
& \\
& \quad + a_{1123}^{<4>} D_{11}D_{23} + a_{1123}^{<4>} D_{11}D_{23} + a_{1123}^{<4>} D_{12}D_{13} + a_{1123}^{<4>} D_{12}D_{13} + a_{1123}^{<4>} D_{12}D_{13} + a_{1123}^{<4>} D_{12}D_{13} \\
& \quad + a_{1123}^{<4>} D_{12}D_{13} + a_{1123}^{<4>} D_{12}D_{13} + a_{1123}^{<4>} D_{12}D_{13} + a_{1123}^{<4>} D_{12}D_{13} + a_{1123}^{<4>} D_{11}D_{23} + a_{1123}^{<4>} D_{11}D_{23} \\
& \\
& \quad + a_{2231}^{<4>} D_{22}D_{13} + a_{2231}^{<4>} D_{22}D_{13} + a_{2231}^{<4>} D_{12}D_{23} + a_{2231}^{<4>} D_{12}D_{23} + a_{2231}^{<4>} D_{12}D_{23} + a_{2231}^{<4>} D_{12}D_{23} \\
& \quad + a_{2231}^{<4>} D_{22}D_{13} + a_{2231}^{<4>} D_{22}D_{13} + a_{2231}^{<4>} D_{12}D_{23} + a_{2231}^{<4>} D_{12}D_{23} + a_{2231}^{<4>} D_{12}D_{23} + a_{2231}^{<4>} D_{12}D_{23} \\
& \\
& \quad + a_{3312}^{<4>} D_{33}D_{12} + a_{3312}^{<4>} D_{33}D_{12} + a_{3312}^{<4>} D_{13}D_{23} + a_{3312}^{<4>} D_{13}D_{23} + a_{3312}^{<4>} D_{13}D_{23} + a_{3312}^{<4>} D_{13}D_{23} \\
& \quad + a_{3312}^{<4>} D_{33}D_{12} + + a_{3312}^{<4>} D_{33}D_{12} + a_{3312}^{<4>} D_{13}D_{23} + a_{3312}^{<4>} D_{13}D_{23} + a_{3312}^{<4>} D_{13}D_{23} + a_{3312}^{<4>} D_{13}D_{23} \\
& \\
& \quad + a_{1112}^{<4>} D_{11}D_{12} + a_{1112}^{<4>} D_{11}D_{12} + a_{1112}^{<4>} D_{11}D_{12} + a_{1112}^{<4>} D_{11}D_{12} \\
& \quad + a_{1131}^{<4>} D_{11}D_{13} + a_{1131}^{<4>} D_{11}D_{13} + a_{1131}^{<4>} D_{11}D_{13} + a_{1131}^{<4>} D_{11}D_{13} \\
& \quad + a_{2212}^{<4>} D_{22}D_{21} + a_{2212}^{<4>} D_{22}D_{21} + a_{2212}^{<4>} D_{22}D_{21} + a_{2212}^{<4>} D_{22}D_{21} \\
& \quad + a_{2223}^{<4>} D_{22}D_{23} + a_{2223}^{<4>} D_{22}D_{23} + a_{2223}^{<4>} D_{22}D_{23} + a_{2223}^{<4>} D_{22}D_{23} \\
& \quad + a_{3331}^{<4>} D_{33}D_{13} + a_{3331}^{<4>} D_{33}D_{13} + a_{3331}^{<4>} D_{33}D_{13} + a_{3331}^{<4>} D_{33}D_{13} \\
& \quad + a_{3332}^{<4>} D_{33}D_{23} + a_{3332}^{<4>} D_{33}D_{23} + a_{3332}^{<4>} D_{33}D_{23} + a_{3332}^{<4>} D_{33}D_{23},
\end{aligned}$$

which can be simplified to,

$$
\begin{aligned}
&a^{<4>}_{ijkl} D_{kl} D_{ij} = \\
&\quad a^{<4>}_{1111} (D_{11})^2 + a^{<4>}_{2222} (D_{22})^2 + a^{<4>}_{3333} (D_{33})^2 \\
&\quad + a^{<4>}_{1122} (2D_{11} D_{22} + 4(D_{12})^2) + a^{<4>}_{1133} (2D_{11} D_{33} + 4(D_{13})^2) + a^{<4>}_{2233} (2D_{22} D_{33} + 4(D_{23})^2) \\
&\quad + 4a^{<4>}_{1123} D_{11} D_{23} + 8a^{<4>}_{1123} D_{12} D_{13} + 4a^{<4>}_{2231} D_{22} D_{13} + 8a^{<4>}_{2231} D_{12} D_{23} + 4a^{<4>}_{3312} D_{33} D_{12} \\
&\quad + 8a^{<4>}_{3312} D_{13} D_{23} \\
&\quad + 4a^{<4>}_{1112} D_{11} D_{12} + 4a^{<4>}_{1131} D_{11} D_{13} + 4a^{<4>}_{2212} D_{22} D_{21} + 4a^{<4>}_{2223} D_{22} D_{23} + 4a^{<4>}_{3331} D_{33} D_{13} \\
&\quad + 4a^{<4>}_{3332} D_{33} D_{23}.
\end{aligned}
\tag{F.2}
$$

Appendix G

Derivation of the evolution equation for the second-order tensor $\mathsf{a}^{(2)}$

We need to compute Eq. (5.14) in order to obtain solutions for the components $a_{11}^{(2)}$, $a_{22}^{(2)}$, $a_{12}^{(2)}$, $a_{23}^{(2)}$ and $a_{13}^{(2)}$. The components of the fourth-order tensor are computed with the IBOF and only nine components are independent. The IBOF computes the following components: $a_{1111}^{<4>}$, $a_{2222}^{<4>}$, $a_{1122}^{<4>}$, $a_{1123}^{<4>}$, $a_{2231}^{<4>}$, $a_{1131}^{<4>}$, $a_{1112}^{<4>}$, $a_{2223}^{<4>}$ and $a_{2212}^{<4>}$. The other components can be deduced from the relation:

$$a_{ijkk} = a_{ij} - a_{ijll} - a_{ijmm} (i.j, k, l, m = 1, 2, 3; k \neq l \neq m). \tag{G.1}$$

so that

$$\begin{aligned} a_{1111}^{<4>} &= a_{11}^{<2>} - a_{1122}^{<4>} - a_{1133}^{<4>} \\ a_{1133}^{<4>} &= -a_{1111}^{<4>} + a_{11}^{<2>} - a_{1122}^{<4>} \end{aligned} \tag{G.2}$$

$$\begin{aligned} a_{2222}^{<4>} &= a_{22}^{<2>} - a_{2211}^{<4>} - a_{2233}^{<4>} \\ a_{2222}^{<4>} &= a_{22}^{<2>} - a_{1122}^{<4>} - a_{2233}^{<4>} \\ a_{2233}^{<4>} &= -a_{2222}^{<4>} + a_{22}^{<2>} - a_{1122}^{<4>} \end{aligned} \tag{G.3}$$

$$\begin{aligned} a_{3333}^{<4>} &= a_{33}^{<2>} - a_{3311}^{<4>} - a_{3322}^{<4>} \\ a_{3333}^{<4>} &= a_{33}^{<2>} - a_{1133}^{<4>} - a_{2233}^{<4>} \end{aligned} \tag{G.4}$$

$$
\begin{aligned}
a_{1333}^{<4>} &= a_{13}^{<2>} - a_{1311}^{<4>} - a_{1322}^{<4>} \\
a_{1333}^{<4>} &= a_{13}^{<2>} - a_{1131}^{<4>} - a_{2231}^{<4>}
\end{aligned} \tag{G.5}
$$

$$
\begin{aligned}
a_{2333}^{<4>} &= a_{23}^{<2>} - a_{2311}^{<4>} - a_{2322}^{<4>} \\
a_{2333}^{<4>} &= a_{23}^{<2>} - a_{1123}^{<4>} - a_{2223}^{<4>}
\end{aligned} \tag{G.6}
$$

$$
\begin{aligned}
a_{1233}^{<4>} &= a_{12}^{<2>} - a_{1211}^{<4>} - a_{1222}^{<4>} \\
a_{1233}^{<4>} &= a_{12}^{<2>} - a_{1112}^{<4>} - a_{2212}^{<4>}.
\end{aligned} \tag{G.7}
$$

After mathematical manipulations, we obtain the five differential equations that need to be solved in the finite-element simulation, they read

$$
\begin{aligned}
&\frac{\partial a_{11}^{(2)}}{\partial t} + \mathbf{v} \cdot \nabla a_{11}^{(2)} + 2\iota(D_{11} - D_{33})a_{11}^{(2)} = \\
&\quad 2(W_{12}a_{12}^{(2)} - W_{31}a_{31}^{(2)}) + 2\iota[D_{12}(2a_{1112}^{(4)} - a_{12}^{(2)}) + D_{31}(2a_{1131}^{(4)} - a_{31}^{(2)}) \\
&\quad + a_{1111}^{(4)}D_{11} + a_{1122}^{(4)}D_{22} - (a_{1111}^{(4)} + a_{1122}^{(4)})D_{33} + 2a_{1123}^{(4)}D_{23}].
\end{aligned} \tag{G.8}
$$

$$
\begin{aligned}
&\frac{\partial a_{22}^{(2)}}{\partial t} + \mathbf{v} \cdot \nabla a_{22}^{(2)} + 2\iota(D_{22} - D_{33})a_{22}^{(2)} = \\
&\quad 2(-W_{12}a_{12}^{(2)} + W_{23}a_{23}^{(2)}) + 2\iota[D_{12}(2a_{2212}^{(4)} - a_{12}^{(2)}) + D_{23}(2a_{2223}^{(4)} - a_{23}^{(2)}) \\
&\quad + a_{1122}^{(4)}D_{11} + a_{2222}^{(4)}D_{22} - (a_{2222}^{(4)} + a_{1122}^{(4)})D_{33} + 2a_{2231}^{(4)}D_{31}].
\end{aligned} \tag{G.9}
$$

$$
\begin{aligned}
&\frac{\partial a_{12}^{(2)}}{\partial t} + \mathbf{v} \cdot \nabla a_{12}^{(2)} - \iota 3D_{33}a_{12}^{(2)} = \\
&\quad W_{12}(a_{22}^{(2)} - a_{11}^{(2)}) - W_{31}a_{23}^{(2)} + W_{23}a_{31}^{(2)} \\
&\quad + D_{12}\iota[4a_{1122}^{(4)} - (a_{11}^{(2)} + a_{22}^{(2)})] + D_{13}\iota(4a_{1123}^{(4)} - a_{23}^{(2)}) \\
&\quad + D_{23}\iota(4a_{2231}^{(4)} - a_{13}^{(2)}) + 2\iota[a_{1211}^{(4)}D_{11} + a_{1222}^{(4)}D_{22} - (a_{1112}^{(4)} + a_{2212}^{(4)})D_{33}].
\end{aligned} \tag{G.10}
$$

$$\begin{aligned}
&\frac{\partial a^{(2)}_{23}}{\partial t} + \mathbf{v}\cdot\nabla a^{(2)}_{23} + \iota(D_{22} - D_{33)}a^{(2)}_{23} = \\
&\quad W_{23}(a^{(2)}_{33} - a^{(2)}_{22}) + W_{31}a^{(2)}_{12} - W_{12}a^{(2)}_{31} \\
&\quad + D_{12}\iota(4a^{(4)}_{2231} - a^{(2)}_{31}) + D_{23}\iota[3a^{(2)}_{22} - a^{(2)}_{33} - 4(a^{(4)}_{2222} + a^{(4)}_{1122})] \\
&\quad + D_{31}\iota[3a^{(2)}_{12} - 4(a^{(4)}_{1122} + a^{(4)}_{2212})] \\
&\quad + 2\iota[a^{(4)}_{1123}D_{11} + a^{(4)}_{2223}D_{22} - (a^{(4)}_{1123} + a^{(4)}_{2223})D_{33}].
\end{aligned} \tag{G.11}$$

$$\begin{aligned}
&\frac{\partial a^{(2)}_{13}}{\partial t} + \mathbf{v}\cdot\nabla a^{(2)}_{13} + \iota(D_{11} - D_{33})a^{(2)}_{13} = \\
&\quad W_{31}(a^{(2)}_{11} - a^{(2)}_{33}) + W_{12}a^{(2)}_{23} - W_{23}a^{(2)}_{12} \\
&\quad + D_{12}\iota(4a^{(4)}_{1123} - a^{(2)}_{23}) + D_{31}\iota[3a^{(2)}_{11} - a^{(2)}_{33} - 4(a^{(4)}_{1111} + a^{(4)}_{1122})] \\
&\quad + D_{23}\iota[3a^{(2)}_{12} - 4(a^{(4)}_{1112} + a^{(4)}_{2212})] \\
&\quad + 2\iota[a^{(4)}_{1311}D_{11} + a^{(4)}_{1322}D_{22} - (a^{(4)}_{1131} + a^{(4)}_{2231})D_{33}].
\end{aligned} \tag{G.12}$$

Appendix H

Integration by part in two and three dimensions: Green's theorem

We consider here the Green's theorem as exposed in Zienkiewicz and others (2005).

Consider the integration by parts of the following two-dimensional expression

$$\int\int_{\Omega} \phi \frac{\partial \psi}{\partial x}\, dx\, dy. \tag{H.1}$$

Integration first with respect to x and using the well-known relation for integration by parts in one dimension

$$\int_{x_L}^{x_R} u\, dv = -\int_{x_L}^{x_R} v\, du + (uv)_{x=x_r} - (uv)_{x=x_L}, \tag{H.2}$$

we have, using the symbols in Fig. H.1

$$\int\int_{\Omega} \phi \frac{\partial \psi}{\partial x}\, dx\, dy = -\int\int_{\Omega} \frac{\partial \phi}{\partial x} \psi\, dx\, dy + \int_{y_B}^{y_T} \left[(\phi\ \psi)_{x=x_R} - (\phi\ \psi)_{x=x_L} \right] dy. \tag{H.3}$$

By considering a direct segment of the boundary $d\Gamma$ on the right-hand boundary , we have,

$$dy = n_x\, d\Gamma, \tag{H.4}$$

where n_x is the direction cosine between the outward normal and the x direction. Similarly on the left-hand section we have

$$dy = -n_x\, d\Gamma. \tag{H.5}$$

The final term of Eq. (H.3) can thus be expresses as the integral taken around an anti-

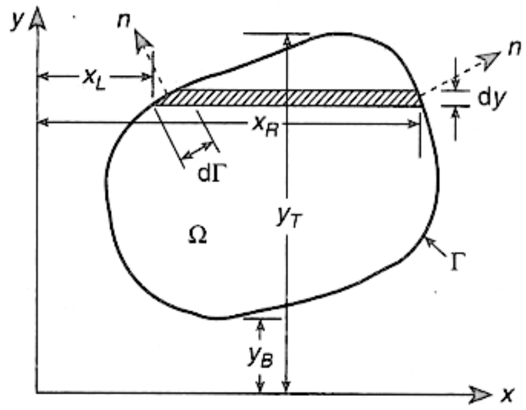

Figure H.1: Definitions for integrations in two dimensions (Zienkiewicz and others, 2005).

clockwise direction of the complete closed boundary:

$$\oint_\Gamma \phi\, \psi\, n_x\, d\Gamma. \tag{H.6}$$

If several closes contours are encountered, this direction has to be taken around each such contours. The general expression in all cases is

$$\int\int_\Omega \phi \frac{\partial \psi}{\partial x}\, dx\, dy = -\int\int_\Omega \frac{\partial \phi}{\partial x} \psi\, dx\, dy + \oint_\Gamma \phi\, \psi\, n_x\, d\Gamma. \tag{H.7}$$

Similarly, if differentiation in the y direction aries we can write

$$\int\int_\Omega \phi \frac{\partial \psi}{\partial y}\, dx\, dy = -\int\int_\Omega \frac{\partial \phi}{\partial y} \psi\, dx\, dy + \oint_\Gamma \phi\, \psi\, n_y\, d\Gamma, \tag{H.8}$$

where n_y is the direction cosine between the outward normal direction and the y axis.

In three dimension, by identical procedure we can write

$$\int\int\int_\Omega \phi \frac{\partial \psi}{\partial y}\, dx\, dy\, dz = -\int\int\int_\Omega \frac{\partial \phi}{\partial y} \psi\, dx\, dy\, dz + \oint_\Gamma \phi\, \psi\, n_y\, d\Gamma, \tag{H.9}$$

where $d\Gamma$ becomes the element of the surface area and the last integral is taken over the whole surface.

Appendix I

Formulation of the viscosity equation in Elmer

The formulation of the Glen's flow law varies with the definition of the second invariants of the deviatoric stress tensor S and the deformation rate tensor D (noted in the following I_{S_2} and I_{D_2} respectively). For the deviatoric stresses, the effective stress and the second invariant have the same definition

$$\sigma^2 = I_{S_2}^2 = \frac{1}{2} S_{ij} S_{ij}. \tag{I.1}$$

For the deformation rates, the second invariant is by definition

$$I_{D_2}^2 = \frac{1}{2} D_{ij} D_{ij}, \tag{I.2}$$

while the effective strain is in general defined as

$$\dot{\gamma}^2 = 2 D_{ij} D_{ij} = 4 I_{D_2}^2. \tag{I.3}$$

In Elmer, the power law reads

$$S_{ij} = 2\eta_0 \, \dot{\gamma}^{m-1} D_{ij}, \tag{I.4}$$

where $m = \frac{1}{n}$. By recalling the power law in Eq. (3.11), we have by identification

$$[\hat{E}(\mathcal{A})]^{-1/n} \, [A(T')]^{-1/n} \, d^{-(1-1/n)} = 2\eta_0 \, \dot{\gamma}^{-(1-1/n)}. \tag{I.5}$$

With Eq. (I.3), we have $\dot{\gamma} = \sqrt{4 I_{D_2}^2} = 2\,d$, so that Eq. (I.5) becomes

$$[\hat{E}(\mathcal{A})]^{-1/n}\,[A(T')]^{-1/n}\,d^{-(1-1/n)} = 2\eta_0\,(2\,d)^{-(1-1/n)},$$

and

$$\eta_0 = \frac{1}{[2\hat{E}(\mathcal{A})A(T')]^{\frac{1}{n}}}. \tag{I.6}$$

The viscosity in Elmer is then computed by

$$\eta = \frac{1}{[2\hat{E}(\mathcal{A})A(T')]^{\frac{1}{n}}}\dot{\gamma}^{-(1-1/n)}. \tag{I.7}$$

Eq. (I.7) is equivalent to Eq. (3.15). This can be shown by using I.1 and I.4, so that we have

$$\begin{aligned}
\sigma^2 = \\
&\frac{1}{2}\left(\frac{2}{[2\hat{E}(\mathcal{A})A(T')]^{\frac{1}{n}}}(2\,d)^{-(1-1/n)}D_{11}\right)^2 \\
&+\frac{1}{2}\left(\frac{2}{[2\hat{E}(\mathcal{A})A(T')]^{\frac{1}{n}}}(2\,d)^{-(1-1/n)}D_{22}\right)^2+\frac{1}{2}\left(\frac{2}{[2\hat{E}(\mathcal{A})A(T')]^{\frac{1}{n}}}(2\,d)^{-(1-1/n)}D_{33}\right)^2 \\
&+\left(\frac{2}{[2\hat{E}(\mathcal{A})A(T')]^{\frac{1}{n}}}(2\,d)^{-(1-1/n)}D_{12}\right)^2+\left(\frac{2}{[2\hat{E}(\mathcal{A})A(T')]^{\frac{1}{n}}}(2\,d)^{-(1-1/n)}D_{13}\right)^2 \\
&+\left(\frac{2}{[2\hat{E}(\mathcal{A})A(T')]^{\frac{1}{n}}}(2\,d)^{-(1-1/n)}D_{23}\right)^2,
\end{aligned}$$

$$\sigma = \frac{2}{[2\hat{E}(\mathcal{A})A(T')]^{\frac{1}{n}}}2^{-(1-1/n)}\,d^{-(1-1/n)}\,d,$$

which gives

$$d = \sigma^n\hat{E}(\mathcal{A})A(T').$$

Similarly, with Eq. (I.1) and Eq. (3.11), we have

$$\begin{aligned}\sigma^2 = \\ &\frac{1}{2}\left([\hat{E}(\mathcal{A})]^{-\frac{1}{n}}\,[A(T')]^{-\frac{1}{n}}\,d^{-(1-1/n)}D_{11}\right)^2 \\ &+\frac{1}{2}\left([\hat{E}(\mathcal{A})]^{-\frac{1}{n}}\,[A(T')]^{-\frac{1}{n}}\,d^{-(1-1/n)}D_{22}\right)^2+\frac{1}{2}\left([\hat{E}(\mathcal{A})]^{-\frac{1}{n}}\,[A(T')]^{-\frac{1}{n}}\,d^{-(1-1/n)}D_{33}\right)^2 \\ &+\left([\hat{E}(\mathcal{A})]^{-\frac{1}{n}}\,[A(T')]^{-\frac{1}{n}}\,d^{-(1-1/n)}D_{12}\right)^2+\left([\hat{E}(\mathcal{A})]^{-\frac{1}{n}}\,[A(T')]^{-\frac{1}{n}}\,d^{-(1-1/n)}D_{13}\right)^2 \\ &+\left([\hat{E}(\mathcal{A})]^{-\frac{1}{n}}\,[A(T')]^{-\frac{1}{n}}\,d^{-(1-1/n)}D_{23}\right)^2,\end{aligned}$$

$$\sigma = [\hat{E}(\mathcal{A})]^{-\frac{1}{n}}\,[A(T')]^{-\frac{1}{n}}\,d^{-(1-1/n)}\,d,$$

which also gives

$$d = \sigma^n \hat{E}(\mathcal{A})A(T^{'}).$$

This result proves the equivalence of Eq. (I.7) and Eq. (3.15).

Appendix J

Simulation results for the non-diagonal elements of the second-order tensor $\mathsf{a}^{(2)}$

The evolution of the $a_{12}^{(2)}$, $a_{23}^{(2)}$ and $a_{13}^{(2)}$ terms of the second-order tensor obtained with the steady-state simulation in the vicinity of the dome are shown in Figs. J.1, J.2 and J.3.

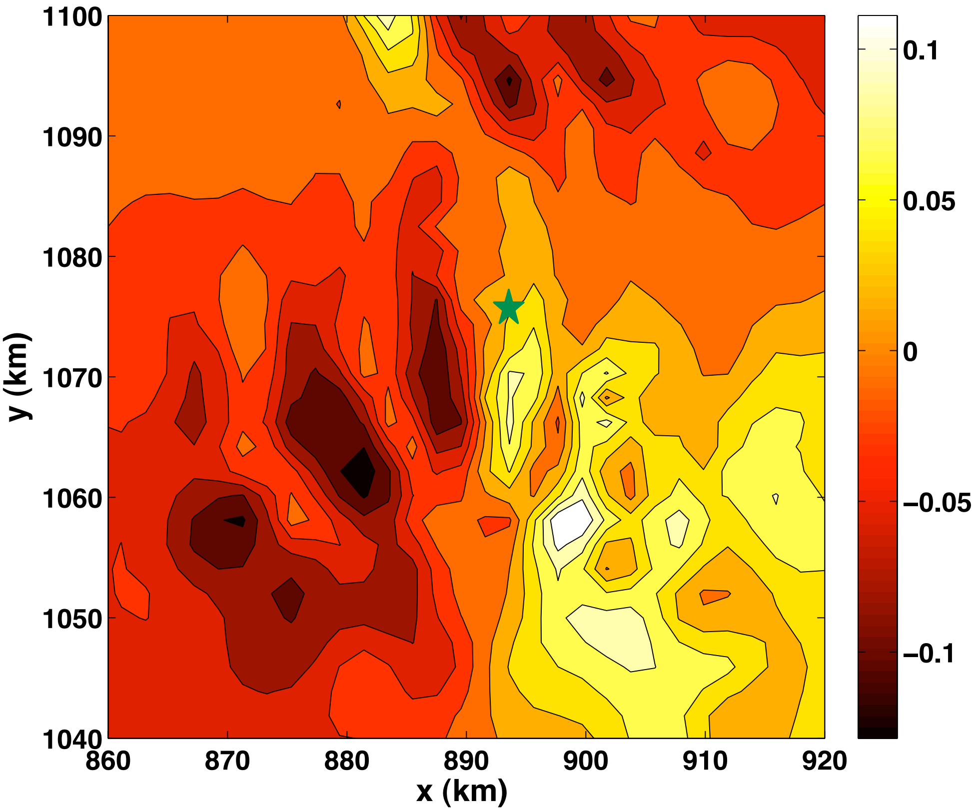

Figure J.1: Basal distribution of $a_{12}^{(2)}$ at the vicinity of the dome. The star indicates the location of the Dome Fuji ice core drilling site.

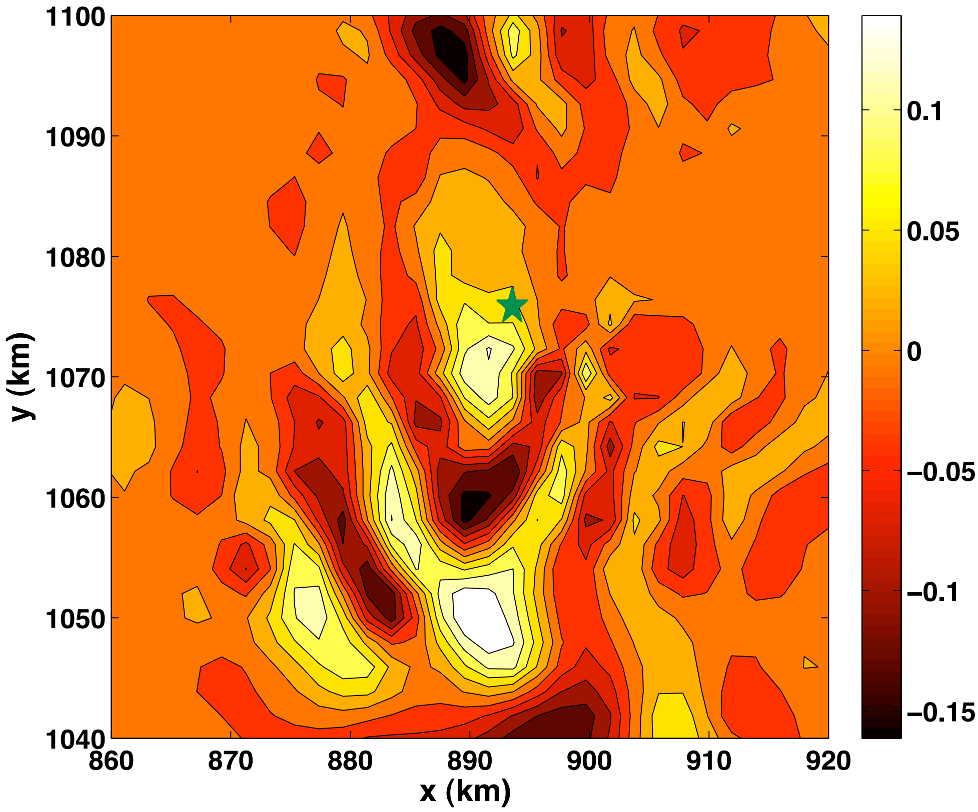

Figure J.2: Basal distribution of $a_{23}^{(2)}$ at the vicinity of the dome. The star indicates the location of the Dome Fuji ice core drilling site.

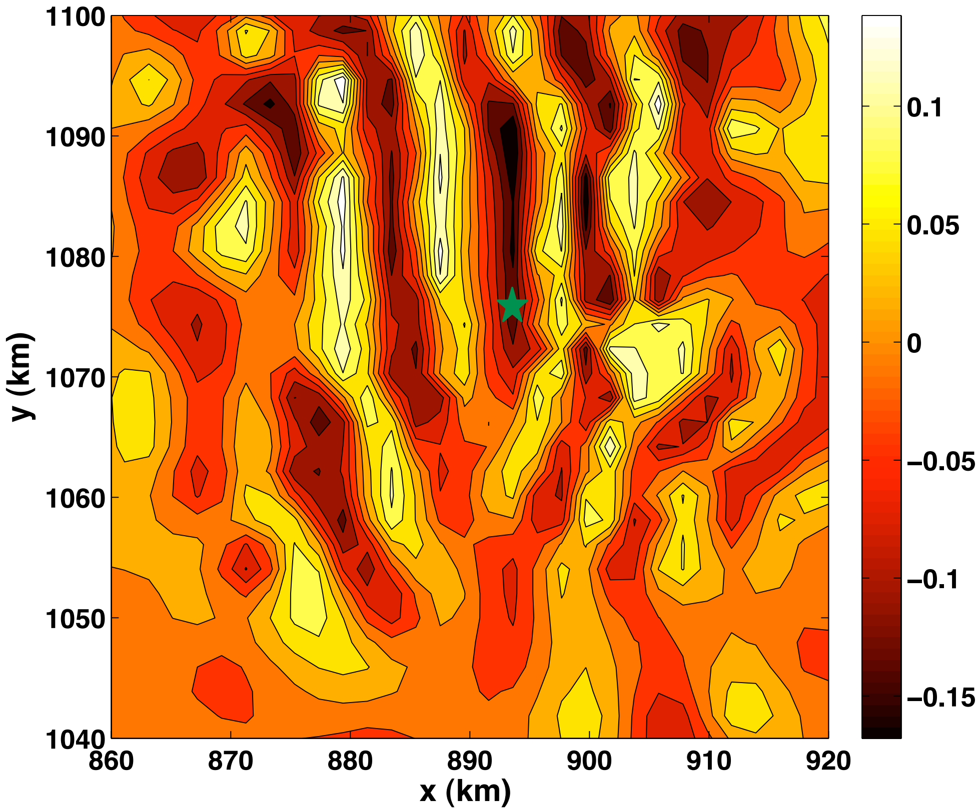

Figure J.3: Basal distribution of $a_{13}^{(2)}$ at the vicinity of the dome. The star indicates the location of the Dome Fuji ice core drilling site.

Bibliography

Advani, N. and C.L. Tucker III, 1987. The use of tensors to describe and predict fiber orientations in short fiber composites, *J. Rheol.*, **31**(8), 751–784.

Azuma, N., 1995. A flow law for anisotropic polycrystalline ice under uniaxial compressive deformation, *Cold Reg. Sci. Technol.*, **23**(2), 137–147.

Azuma, N. and K. Goto-Azuma, 1996. An anisotropic flow law for ice-sheet and its implications, *Ann. Glaciol.*, **23**, 601–614.

Azuma, N., Y. Wang, K. Mori, H. Narita, T. Hondoh, H. Shoji and O. Watanabe, 1999. Textures and fabrics in the Dome F (Antarctica) ice core, *Ann. Glaciol.*, **29**, 163–168.

Baiocchi, C., F. Brezzi and L. Franca, 1993. Virtual bubbles and the Galerkin least squares method, *Comp. Meths. Appl. Mech. Engrg.*, **105**, 125–141.

Boehler, J.P., 1978. Lois de comportement anisotrope des milieux continus, *J. de Mécanique*, **17**(2), 153–190.

Brezzi, F., L. Marini and E. Süli, 2004. Discontinuous Galerkin methods for first-order hyperbolic problems, *Math. Models Meths. Appl. Sci.*, **14**(12), 1893–1903.

Budd, W.F. and T.H. Jacka, 1989. A review of ice rheology for ice sheet modeling, *Cold Reg. Sci. Technol.*, **16**, 107–144.

Castelnau, O., 1996. Modélisation du comportement mécanique de la glace polycristalline par une approche auto-cohérente; application au développement de textures dans les glaces des calottes polaires, Doctoral thesis, Joseph-Fourier University, Grenoble I, France.

Castelnau, O. and P. Duval, 1994. Simulations of anisotropy and fabric development in polar ices, *Ann. Glaciol.*, **20**, 277–282.

Castelnau, O., P. Duval, R.A. Lebensohn and G. Canova, 1996b. Viscoplastic modeling of texture development in polycrystalline ice with a self-consistent approach: Comparison with bound estimates, *J. Geophys. Res.*, **16**(6), 851/13–868.

Chung, D.H. and T.H. Kwon, 2002. Invariant-based optimal fitting closure approximation for the numerical prediction of flow-induced fiber orientation, *J. Rheol.*, **46**, 169–194.

Cintra, J.S. and C.L. Tucker, 1995. Orthotropic closure approximation for flow-induced fiber orientation, *J. Rheol.*, **39**, 1095–1122.

Dafalias, Y. F., 2001. Orientation distribution function in non-affine rotations, *J. Mech. Phys. Solids*, **49**(11), 2493–2516.

Dahl-Jensen, D., S. J. Johnsen, C.U. Hammer, H. B. Clausen and J. Jouzel, 1993. Past accumulation rates derived from observed annual layers in the GRIP ice core from summit. central Greenland, *NATO ASI Ser., Ser, I*, **12**, 517–531.

Dansgaard, W. and S. J. Johnsen, 1969. A flow model and a time scale for the ice core from Camp Century, Greenland, *J. Glaciol.*, **8**(53), 215–223.

Deponti, A., V. Pennati and L. De Biase, 2006. A fully 3D finite volume method for incompressible Navier-Stokes equations, *Int. J. Numer. Meth. Fluid.*, **52**, 617–638.

Doake, C.S. and E.W. Wolff, 1985. Flow law on polar ice sheets, *Nature*, **314**, 255–257.

Doi, M., 1981. Molecular dynamics and rheological properties of concentrated solutions of rodlike polymers in isotropic and liquid crystalline phases, *J. Polym. Sci., Polym. Phys. Ed.*, **19**, 229–243.

Dupret, F., V. Verleye and B. Languillier, 1997. Numerical prediction of the molding of composite parts, *Rheology and Fluid Mechanics of Nonlinear Materials, ASME*, **78**, 79–90.

Durand, G., A. Persson, D. Samyn and A. Svensson, 2008. Relation between neighbouring grains in the upper part of the NorthGRIP ice core – Implications for rotation recrystallization, *Earth Planet. Sci. Lett.*, **265**(3), 666–671.

Durand, G., J. Weiss, V. Lipenkov, J.M. Barnola, G. Krinner, F. Parrenin, B. Delmonte, C. Ritz, P. Duval, R. Roethsliberger and M. Bigler, 2006a. Effect of impurities on grain growth in cold ice sheets, *J. Geophys. Res.*, **111**(F01015).

Duval, P., M.F. Ashby and I. Anderman, 1983. Rate-controlling processes in the creep of polycrystalline ice, *J. of Phys. Chem.*, **87**(21), 4066–4074.

Duval, P. and H. Le Gac, 1982. Mechanical behaviour of Antarctic ice, *Ann. Glaciol.*, **3**, 92–95.

Faria, S. H., 2003. Mechanics and thermodynamics of mixtures with continuous diversity, Doctoral thesis, Department of Mechanics, Darmstadt University of Technology, Germany, available online at http://elib.tu-darmstadt.de/diss/000307/.

Faria, S. H., 2006a. Creep and recrystallization of large polycrystalline masses. I. General continuum theory, *Proc. R. Soc. Lond.*, **A**(462), 1493–1514.

Faria, S. H., 2006b. Creep and recrystallization of large polycrystalline masses. III. Continuum theory of ice sheets, *Proc. R. Soc. Lond.*, **A**(462), 2797–2816.

Faria, S. H., G. M. Kremmer and K. Hutter, 2006. Creep and recrystallization of large polycrystalline masses. II. Constitutive theory for crystalline media with transversely isotropic grains, *Proc. R. Soc. Lond.*, **A**(462), 1699–1720.

Franca, L. P. and S. L. Frey, 1992. Stabilized finite elements methods: II. the incompressible Navier-Stokes equations., *Comp. Meths. Appl. Mech. Engrg.*, **99**, 209–233.

Franca, L. P., S. L. Frey and T.J.R. Hughes, 1992. Stabilized finite elements methods: I. application to the advective-diffusive model., *Comp. Meths. Appl. Mech. Engrg.*, **95**, 253–276.

Gagliardini, O., 1999. Simulation numérique d'un écoulement bidimensionnel de la glace polaire présentant une anisotropie induite évolutive, Doctoral thesis, Joseph-Fourier University, Grenoble I, France.

Gagliardini, O. and J. Meyssonnier, 2000. Simulation of anisotropic ice flow and fabric evolution along the GRIP-GISP2 flow line (Central Greenland), *Ann. Glaciol.*, **30**, 217–223.

Gillet-Chaulet, F., O. Gagliardini, J. Meyssonnier, M. Montagnat and O. Castelnau, 2005. A user-friendly anisotropic flow law for ice-sheet modelling, *J. Glaciol.*, **51**(172), 3–14.

Gillet-Chaulet, F., O. Gagliardini, J. Meyssonnier, T. Zwinger and J. Ruokolainen, 2006. Flow induced anisotropy in polar ice and related ice-sheet flow modeling, *J. Non-Newtonian Fluid Mech.*, **134**, 33–43.

Gödert, G., 2003. A mesoscopic approach for modelling texture evolution of polar ice including recrystallization phenomena, *Ann. Glaciol.*, **37**, 23–28.

Gödert, G. and K. Hutter, 1998. Induced anisotropy in large ice shields: Theory and its homogenization, *Cont. Mech. Thermodyn.*, **10**, 293–318.

Greve, R., 1997. A continuum-mechanical formulation for shallow polythermal ice sheets, *Phil. Trans. R. Soc. Lond.*, **A355**(1726), 921–974.

Greve, R., 2005. Dynamics of Ice Sheets and Glaciers, Lecture notes, Hokkaido University OpenCourseWare, available online at http://ocw.hokudai.ac.jp/Course/GraduateSchool/EnvironmentalScience/DynamicsOfIce/.

Greve, R. and H. Blatter, 2008. Dynamics of Ice Sheets and Glaciers, Springer, Berlin, etc., in press.

Greve, R., Y. Wang and B. Mügge, 2002. Comparison of numerical schemes for the solution of the advective age equation in ice sheets, *Ann. Glaciol.*, **35**, 487–494.

Hamann, I., S. Kipfstuhl and A. Lambrecht, 2008. Ice-Fabrics study in EDML deep ice core (Antarctica), Paper in preparation.

Han, K.H. and Y.T. Im, 2002. Numerical simulation of three-dimensional fiber orientation in short-fiber-reinforced injection-molded parts, *J. Mater. Process. Technol.*, **124**, 366–371.

Hand, G.L., 1962. A theory of anisotropic fluids, *J. Fluid. Mech.*, **13**, 33–46.

Hooke, R. LeB., 2005. Principles of Glacier Mechanics, Cambridge University Press, Cambridge etc., 2nd ed.

Hutter, K., 1983. Theoretical Glaciology; Material Science of Ice and the Mechanics of Glaciers and Ice Sheets, D. Reidel Publishing Company, Dordrecht, The Netherlands.

Huybrechts, P., O. Rybak, F. Pattyn, U. Ruth and D. Steinhage, 2007. Ice thinning, upstream advection, and non-climatic biases for the upper 89% of the EDML ice core from a nested model of the Antarctic ice sheet, *Clim. Past Discuss.*, **3**(3), 693–727.

Hvidberg, C.S., 1996. Steady-state thermo-mechanical modeling of ice flow near the center of large ice sheets with the finite-element technique, *Ann. Glaciol.*, **23**, 116–123.

Hvidberg, C.S., D. Dahl-Jensen and E. D. Waddington, 1996. Ice flow between the GRIP and GISP2 boreholes in Central Greenland, *J. Geophys. Res.*, **102**(C12), 851–26–859.

Jacka, T. H. and W. F. Budd, 1989. Isotropic and anisotropic flow relations for ice dynamics, *Ann. Glaciol.*, **12**, 81–84.

Kamb, W.B., 1961. The glide direction in ice, *J. Glaciol.*, **3**(30), 1097–1106.

Kameda, T., H. Motoyama, S. Fujita and S. Takahashi, 2008. Temporal and spatial variability of surface mass balance at Dome Fuji, East Antarctica, by the stake method from 1995 to 2006, *J. Glaciol.*, **54**(184), 107–116.

Kawamura, K., T. Nakazawa, S. Aoki, S. Sugawara, Y. Fujii and O. Watanabe, 2003. Atmospheric CO2 variations over the last three glacial-interglacial climatic cycles deduced from the Dome Fuji deep ice core, Antarctica using a wet extraction technique, *Tellus*, **55**(B), 126–137.

Kawamura, K., F. Parrenin, L. Lisiecki, R. Uemura, F. Vimeux, J.P. Severinghaus, M.A. Hutterli, T. Nakazawa, S. Aoki, J. Jouzel, M.E. Raymo, K. Matsumoto, H. Nakata, H. Motoyama, S. Fujita, K. Goto-Azuma, Y. Fujii and O. Watanabe, 2007. Northern Hemisphere forcing of climatic cycles in Antarctica over the past 360,000 years, *Nature*, **448**, 912–916.

Le Gac, H., 1980. Contribution à la détermination des lois de comportement de la glace polycristalline (anélasticité et plasticité), Doctoral thesis, Grenoble University, France.

Lebensohn, R.A. and C.N. Tomé, 1993. A self-consistent anisotropic approach for the simulation of plastic deformation and texture development of polycrystals: application to zirconium alloys, *Acta metall, mater.*, **41**(9), 2611–2624.

Lequeu, P.H., P. Gilormini, F. Montheillet, B. Bacroix and J.J. Jonas, 1987. Yield surfaces for textured polycrystals -I. Crystallographic approach, *Acta metall, mater.*, **35**(2), 439–451.

Lipenkov, V.Y., A.N. Salamatin and P. Duval, 1997. Bubbly-ice densification in ice sheets: II. Applications, *J. Glaciol.*, **43**(115), 397–407.

Lipscomb, G.G., M.M. Denn, D.U. Hur and D.V. Boger, 1988. The flow of fiber suspensions in complex geometries, *J. Non-Newtonian Fluid Mech.*, **26**, 297–325.

Liu, H., K. Jezek, B. Li and Z. Zhao, 2001. Radarsat Antarctic Mapping Project digital elevation model version 2, Digital Media. National Snow and Ice Data Center, Boulder, CO, USA.

Lliboutry, L., 1993. Anisotropic, transversely isotropic non linear viscosity of rock ice and rheological parameters inferred by homogenization, *Int. J. Plast.*, **9**, 619–632.

Lliboutry, L. and P. Duval, 1985. Various isotropic and anisotropic ices found in glacier and polar ice caps and their corresponding rheologies, *Annales Geophysicae*, **3**(2), 207–224.

Lythe, M.B., D.G. Vaughan and the BEDMAP Consortium, 2000. BEDMAP-bed topography of the Antarctic. 1:10,000,000 scale map, BAS(Misc) 9. Cambridge, British Antarctic Survey.

Mangeney, A., 1996. Modélisation de l'écoulement de la glace dans les calottes polaires: prises en compte d'une loi de comportement anisotropique, Doctoral thesis, Pierre et Marie Curie University, Paris VI, France.

Mangeney, A., F. Califano and O. Castelnau, 1996. Isothermal flow of an anisotropic ice sheet in the vicinity of an ice divide, *J. Geophys. Res.*, **101**(12), 189–28–204.

Mansuy, P., 2001. Contribution à l'étude du comportement viscoplastique d'un multicristal de glace: hétérogéinité de la déformation et localisation, expériences et modèles, Doctoral thesis, Joseph-Fourier University, Grenoble I, France.

Martin, C., R. Hindmarch and F. Navarro, 2006. Dating ice flow change near the flow divide at Roosevelt Island, Antarctica, by using a thermo-mechanical model to predict radar stratigraphy, *J. Geophys. Res.*, **111**.

Meyssonier, J., P. Duval, O. Gagliardini and A. Philip, 2001. Constitutive modeling and flow simulation of anisotropic polar ice, Continuum mechanics and applications in geophysics and the environment. Berlin, etc. Springer-Verlag.

Meyssonier, J. and A. Philip, 1996. A model for the tangent viscous behaviour of anisotropic polar ice, *Ann. Glaciol.*, **23**, 253–261.

Miyamoto, A., 1999. Mechanical properties and crystal textures of Greenland deep ice cores, Doctoral thesis, Hokkaido University, Sapporo, Japan.

Montagnat Rentier, M., 2001. Contribution à l'étude du comportement viscoplastique des glaces des calottes polaires: modes de déformation et simulation du développement des textures, Doctoral thesis, Joseph-Fourier University, Grenoble I, France.

Morland, L. W., 1984. Thermo-mechanical balances of ice sheet flows, *Geophys. Astrophys. Fluid Dyn.*, **29**, 237–266.

Morland, L. W. and R. Staroszczyk, 1998. Viscous response of Polar ice with evolving fabric, *Cont. Mech. Thermodyn.*, **10**, 115–120.

Motoyama, H., 2007. The second deep ice coring project at Dome Fuji, Antarctica, *Scientific Drilling*, **5**, 41–43.

Parrenin, F., J.M. Barnola, J. Beer, T. Blunier, E. Castellano, J. Chappellaz, G. Dreyfus, H. Fischer, S. Fujita, J. Jouzel, K. Kawamura, B. Lemieux-Dudon, L. Loulergue, V. Masson-Delmotte, B. Narcisi, J.R. Petit, G. Raisbeck, D. Raynaud, U. Ruth, J. Schwander, M. Severi, R. Spahni, J.P. Steffensen, A. Svensson, R. Udisti, C. Waelbroeck and E. Wolff, 2007. The EDC3 chronology for the EPICA Dome C ice core, *Clim. Past*, **3**, 485–497.

Paterson, W. S. B., 1991. Why ice-age ice is sometimes “soft”, *Cold Reg. Sci. Technol.*, **20**(1), 75–98.

Paterson, W. S. B., 1994. The Physics of Glaciers, Pergamon Press, Oxford etc., 3rd ed.

Pattyn, F., 2003. A new three-dimensional higher-order thermo-mechanical ice sheet model: Basis sensitivity, ice stream development, and ice flow across subglacial lakes, *J. Geophys. Res.*, **108**(B8).

Pettit, E. C., 2003. Unique dynamic behaviour of ice divides: Simple Dome and the rheological properties of ice, Doctoral thesis, University of Washington.

Pettit, E. C. and E. D. Waddigton, 2003. Ice flow at low deviatoric stress, *J. Glaciol.*, **49**(166).

Pimienta, P., 1987. Etude du comportement mecanique des glaces polycristallines aux faibles contraintes; applications aux glaces des calottes polaires, Doctoral thesis, University of Grenoble, France.

Pimienta, P., P. Duval and V. Y. Lipenkov, 1987. Mechanical behaviour of anisotropic polar ice, Waddington, E. D. and J. S. Walder, eds., The Physical Basis of Ice Sheet Modelling, IAHS Press, Wallingford, UK, IAHS Publication No. 170, 57–66.

Placidi, L., 2004. Thermodynamically consistent formulation of induced anisotropy in polar ice accounting for grain-rotation, grain-size evolution and recrystallization, Doctoral thesis, Department of Mechanics, Darmstadt University of Technology, Germany, available online at http://elib.tu-darmstadt.de/diss/000614/.

Placidi, L., 2005. Microstructured continua treated by the theory of mixtures, Doctoral thesis, University of Rome “La Sapienza”, Italy.

Placidi, L., R. Greve, H. Seddik and S. H. Faria, 2008. A continuum-mechanical, anisotropic flow model for polar ice, based on an anisotropic flow enhancement factor (CAFFE), Paper in preparation.

Placidi, L. and K. Hutter, 2006a. An anisotropic flow law for incompressible polycrystalline materials, *Z. angew. Math. Phys.*, **57**, 160–181.

Placidi, L. and K. Hutter, 2006b. Thermodynamics of polycrystalline materials treated by the theory of mixtures with continuous diversity, *Cont. Mech. Thermodyn.*, **17**(6), 409–451.

Placidi, L., K. Hutter and S. H. Faria, 2006. A critical review of the mechanics of polycrystalline polar ice, *GAMM-Mitt.*, **29**(1), 80–117.

Raymond, C. F., 1983. Deformation in the vicinity of ice divides, *J. Glaciol.*, **29**, 357–373.

Schulson, E. M., 1999. The structure and mechanical behaviour of ice, *JOM*, **51**(2), 21–27.

Staroszczyk, R. and L. W. Morland, 2000. Plane ice sheet flow with evolving orthotropic fabric, *Ann. Glaciol.*, **30**, 93–101.

Svendsen, B. and K. Hutter, 1996. A continuum approach for modeling induced anisotropy in glaciers and ice sheets, *Ann. Glaciol.*, **23**, 262–269.

Thorsteinsson, T., 1996. Textures and fabrics in the GRIP ice core, in relation to climate history and ice deformation, Ber. Polarforsch. 205.

Thorsteinsson, T., 2001. An analytical approach to deformation of anisotropic ice-crystal aggregates, *J. Glaciol.*, **47**(158), 507–516.

Thorsteinsson, T., 2002. Fabric development with nearest-neighbor interaction and dynamic recrystallization, *J. Geophys. Res.*, **107**(B1), 1–13.

Thorsteinsson, T., J. Kipfstuhl and H. Miller, 1997. Textures and fabrics in the GRIP ice core, *J. Geophys. Res.*, **102**(C12), 583–600.

Tommasi, A., D. Mainprice, G. Canova and Y. Chastel, 2000. Viscoplastic self-consistent and equilibrium-based modeling of olivine lattice preferred orientations: Implications for the upper mantle seismic anisotropy, *J. Geophys. Res.*, **105**(B4), 7893–7908.

Van der Veen, C. J., 1999. Fundamentals of Glacier Dynamics, A. A. Balkema, Rotterdam.

Van der Veen, C. J. and I.M. Whillans, 1994. Development of fabric in ice, *Cold Reg. Sci. Technol.*, **22**(22), 171–195.

Wang, Y., J. Kipfstuhl, N. Azuma, W. Thorsteinsson and H. Miller, 2003. Ice-fabrics study in the upper 1500 m of the Dome C (East Antarctica) deep ice core, *Ann. Glaciol.*, **37**, 97–104.

Watanabe, O., K. Kamiyama, H. Motoyama, Y. Fujii, M. Igarashi, T. Furukawa, K. Goto-Azuma, T. Saito, S. Kanamori, N. Kanamori, N. Yoshida and R. Uemura, 2003. General tendencies of stable isotopes and major chemical constituents of the Dome Fuji deep ice core, *Mem. Natl. Inst. Polar Res., Spec. Issue*, **57**, 1–24.

Wesche, C., O. Eisen, H. Oerter, D. Schulte and D. Steinhage, 2007. Surface topography and ice flow in the vicinity of the EDML deep-drilling site, *J. Glaciol.*, **53**(182), 442–448.

Wilson, J. L., D. S. Russell-Head and H. M. Sim, 2003. The application of an automated fabric analyzer system to the textural evolution of folded ice layers in shear zones, *Ann. Glaciol.*, **37**, 7–17.

Zienkiewicz, O.C., R.L. Taylor and J.Z. Zhu, 2005. The finite element method: its basis and fundamentals, Butterworth-Heinemann, UK.